Analog Quantum Simulation via Parametric Interactions in Superconducting Circuits

by

Jamal Husain Busnaina

A thesis
presented to the University of Waterloo
in fulfillment of the
thesis requirement for the degree of
Doctor of Philosophy
in
Electrical and Computer Engineering (Quantum Information)

Waterloo, Ontario, Canada, 2023

Examining Committee Membership

The following served on the Examining Committee for this thesis. The decision of the Examining Committee is by majority vote.

External Examiner:	Dr. Max Hofheinz Professor, Dept. of Electrical and Computer Engineering, University of Sherbrooke
Supervisor:	Dr. Christopher Wilson Professor, Dept. of Electrical and Computer Engineering, University of Waterloo
Internal Member:	Dr. Hamed Majedi Professor, Dept. of Electrical and Computer Engineering, University of Waterloo
Internal Member:	Dr. Michal Bajcsy Professor, Dept. of Electrical and Computer Engineering, University of Waterloo
Internal-External Member:	Dr. Christine Muschik Professor, Dept. of Physics and Astronomy, University of Waterloo

Author's Declaration

I hereby declare that I am the sole author of this thesis. This is a true copy of the thesis, including any required final revisions, as accepted by my examiners.

I understand that my thesis may be made electronically available to the public.

Abstract

While universal quantum computers are still years away from being used for simulating complicated quantum systems, analog quantum simulators have become an increasingly attractive approach to studying classically intractable quantum systems in condensed matter physics, chemistry, and high-energy physics. In this dissertation, we utilize superconducting cavities and qubits to establish analog quantum simulation (AQS) platforms to study systems of interest.

An approach of AQS that has gained interest lately is the use of photonic lattices to simulate popular lattice models. These systems consist of an array of cavities or resonators arranged on a lattice with some couplings graph between modes. We propose an *in situ* programmable platform based on a superconducting multimode cavity. The unique design of the cavity allows us to program arbitrarily connected lattices where the coupling strength and phase of each individual coupling are highly programmable via parametrically activated interactions. Virtually, any quadratic bosonic Hamiltonian can be realized in our platform with a straightforward pumping scheme.

The effectiveness of the cavity-based AQS platform was demonstrated by the experimental simulation of two interesting models. First, we simulated the effect of a fictitious magnetic field on a 4-site plaquette of a bosonic Creutz ladder, a paradigmatic topological model from high-energy physics. Under the right magnetic field conditions, we observed topological features such as emergent edge states and localized soliton states. The platform's ability is further explored by introducing pairing (downconversion) terms to simulate the Bosonic Kitaev chain (BKC), the bosonic version of the famous Fermionic Kitaev chain that hosts Majorana fermions. We observe interesting properties of BKC, such as chiral transport and sensitivity to boundary conditions.

In the final part of the dissertation, we propose and implement a parametrically activated three-qubit interaction in a circuit QED architecture as the simplest building block to simulate lattice gauge theories (LGT). LGT is a framework for studying gauge theories in discretized space-time, often used when perturbative methods fail. The gauge symmetries lead to conservation laws, such as Gauss's law in electrodynamics, which impose constraints tying the configuration of the gauge field to the configuration of "matter" sites. Therefore, any quantum simulation approach for LGTs must maintain these conservation laws, with one strategy in AQS being to build them in at the hardware level. Here, the gauge constraints are explicitly included using a higher-order parametric process between three qubits. The simplest 2-site U(1) LGT building block is realized with two qubits as matter sites and a third qubit as the gauge field mediating the matter-matter interaction, which is crucial to maintain the symmetry of U(1) LGTs.

Acknowledgements

My Ph.D. journey has been a profound and transformative experience, encompassing both the achievement of my doctoral degree and significant personal growth. I would like to express my heartfelt gratitude to the many individuals who have played pivotal roles in this journey, which, like that of many others, endured the challenges of the COVID-19 pandemic.

I am deeply grateful to my supervisor, Christopher Wilson, for the opportunity to join Engineered Quantum Systems Laboratory (EQSL), and his exceptional guidance and mentorship on this journey. His skillful balance between providing direction and fostering independence has enabled my personal and intellectual growth. Christopher's unwavering support during both personal challenges and unforeseen experimental setbacks reflects his generous spirit. I truly appreciate his consistent presence and invaluable guidance throughout this endeavor.

I had the privilege of collaborating with senior colleagues, particularly the postdoctorate fellows. I extend my heartfelt appreciation to Ibrahim for his invaluable assistance, especially during many restless days and nights spent in the Quantum-Nano Fabrication and Characterization Facility (QNFCF). His dedication and craftsmanship have been genuinely inspiring. Dima's consistent assistance with experiment setups and the cryostat was indispensable to my research. Furthermore, I enjoyed working with Zheng, our esteemed theorist, engaging in enlightening discussions spanning physics and beyond. Zheng's insights offered me valuable glimpses into the mindset of theoretical physicists.

EQSL introduced me to a remarkable community of colleagues, some of whom became cherished friends. Sandbo, my office mate for an extended period, not only engaged me in enlightening discussions but also contributed significantly to my work through this device. Jimmy and I were partners in multiple projects, I enjoyed working together for a long time. I'm also grateful to Cindy for being a friend and valuable colleague helping me with fabrication and experiments. My heartfelt thanks extend to EQSL members Bharat, Guang, Ben, Huichen, Mohammad, Amir, Nizar, Luyao, and Vadiraj. Their invaluable support has left a substantial mark on my academic journey.

Dedication

To my beloved family,
To my dear father and mother, your love, guidance, and unconditional support have shaped me into the person I am today. I am eternally grateful. To my sisters, Huda, Toha, and Hunaida, your unwavering love and encouragement have been a constant source of inspiration.

To my cherished wife, Nawal,
Your love, patience, and belief in me have been my greatest blessings. This dedication is a small token of my appreciation for your extraordinary presence in my life.

To my beloved children, Leen and Husain,
Your laughter and innocence have filled my life with immeasurable joy and purpose. You are my greatest treasures.

In memory of those who lost their lives in the devastating flooding in Derna, may their souls find eternal peace.

With profound gratitude, I thank Allah for the countless blessings that He has bestowed upon me, and I seek His guidance and mercy in all endeavors.

Table of Contents

List of Figures

List of Tables

Chapter 1

Introduction

Quantum simulation is a rapidly developing field that has the potential to revolutionize our understanding of quantum systems. In particular, there is an increasing need to develop methods for simulating complex quantum systems that are classically intractable.

Classical computers have provided valuable insights into the behavior of many quantum systems through numerical methods such as quantum Monte Carlo simulations. However, the exponential scaling of quantum systems and the infamous "sign problem" can make simulating certain systems intractable [1, 2]. The sign problem, which arises from the intrinsic physical properties of the system [3, 4, 1, 5], remains incurable in many cases, particularly for a large set of quantum field theories [6, 7], as well as topologically ordered systems [8], such as quantum spin liquids [9]. In addition, sign problems also affect simulating lattice gauge theories (LGT), particularly, real-time evolution [10] and models with finite fermion density [11].

Analog quantum simulation (AQS) offers a near-term solution to unlocking the power of quantum computing. In AQS, a well-controlled artificial system is constructed to have the same Hamiltonian as the system of interest, and the dynamics of the artificial system can be studied to gain insights into the behavior of the original system. A particularly advantageous case for AQS compared to digital quantum simulation with qubits are simulations involving bosonic fields, which can be challenging to encode on small-scale qubit-based computers.

In this dissertation, we aim to investigate the use of AQS as a tool for studying classically intractable systems, particularly those with topological properties and lattice gauge theories models. One of our key contributions is the advancement of an *in situ* programmable platform for AQS, which is based on a multimode superconducting parametric cavity. We utilized this platform to demonstrate the feasibility of simulating topological models such

as the bosonic Creutz ladder and the bosonic Kitaev chain. Additionally, we propose and implement a three-qubit circuit as a building block for investigating many-body interactions in lattice gauge theories (LGT). We will delve into the design, implementation, and characterization of AQS circuits, highlighting the potential of AQS as a powerful simulation tool for quantum systems and its potential applications in quantum computing. To proceed, the thesis is presented as follows.

In chapter 2, we will delve into the design and implementation of the building blocks used in the research, including superconducting cavities, superconducting quantum interference devices (SQUIDs), transmon qubits, and other relevant components. We will also discuss the role these building blocks play in the overall research and how they were used to achieve specific goals.

In chapter 3, we will focus on developing and demonstrating the *in situ* programmable platform for AQS. We will provide a detailed discussion of the theory and implementation of the AQS platform and the experimental setup.

In chapter 4: we will discuss the theory of the bosonic Creutz ladder and the implementation of the model on our AQS platform. We demonstrate the use of the hopping terms in our AQS platform to simulate a plaquette of Creutz ladder model under the effect of the external magnetic field. We then provide an analysis of the experimental results to show the emergent topological properties predicted in theory.

In chapter 5, we will extend the application of the AQS platform by adding a pairing (downconversion) interaction to our set of programmable terms. The simulation of the bosonic Kitaev chain model is demonstrated, which includes both the hopping and pairing terms. We will provide the theory of the model, predicted properties, and implementation on the AQS platform. The results of the simulated chain will be discussed to show that the predicted chiral properties are achieved.

In chapter 6, we will focus on designing and implementing a three-qubit circuit as a building block for simulating many-body interactions in LGTs.We will provide an overview of the theory of LGTs with a focus on U(1) LGTs in particular. We will provide an in-depth discussion of the implementation of the building block in the three-qubit circuit. Then, we will discuss the experiment including device characterization and measurements of the three-qubit circuit, and how the results mimic the dynamics of 2-site U(1) LGTs.

Chapter 2

Building Blocks Development

This chapter will delve into the design and implementation of the building blocks used in this thesis research, including superconducting cavities, superconducting quantum interference devices (SQUIDs), transmon qubits, and any other relevant components.

2.1 Josephson junction

A Josephson junction is a nonlinear device made of two superconducting electrodes separated by a thin insulating layer. It is the key element in superconducting devices, including tunable cavities and qubits.

In superconducting metals, at very low temperatures, the electrons form Cooper pairs as phonon scattering is suppressed, allowing current flow with zero resistance. Electron pairing occurs due to attractive interaction mediated by the exchange of virtual phonons, giving rise to a macroscopic quantum coherence across the material [12]. In contrast to normal metals, where electrons and their dynamics are described statistically, Cooper pairs are represented by one macroscopic wavefunction that describes the quantum state extending over the entire material.

In a Josephson junction, the macroscopic wavefunction extends across the insulating layer from one electrode to the other with a nonzero amplitude. Thus, Cooper pairs can tunnel through the insulating layer, resulting in a supercurrent flowing through the junction, a phenomenon known as quantum tunneling, depicted in Fig. 2.1. The supercurrent is a direct result of the phase coherence of the macroscopic wavefunctions on the two sides of

the junction. The phase difference between the wave functions creates the dynamics of Cooper pairs, which are described by the Josephson equations:

$$V = (\frac{\hbar}{2e})\frac{d\varphi}{dt} \qquad \text{voltage} - \text{phase relation} \tag{2.1}$$

$$I = I_c \sin\varphi \qquad \text{current} - \text{phase relation} \tag{2.2}$$

Here, I_c is the critical current, φ is the phase difference, $\hbar$ is the reduced Planck constant, and e is the electron charge. The critical current is the maximum allowable supercurrent through a junction before it becomes dissipative. It can be related to the normal-state resistance, R_N, with the Ambegaokar-Baratoff relation at approximately $T \approx 0$ [13].

$$I_c = \frac{\pi\Delta_{sc}(T)}{2eR_N}, \tag{2.3}$$

where $2\Delta_{sc}$ is the superconducting energy gap of the electrodes on either side of the junction. The Josephson junction energy can be written as:

$$U_J = \int_0^t dt I(t)V(t), \tag{2.4}$$

where $V(t)$ is the voltage across the junction, and $I(t)$ is the current flowing through the junction, both as functions of time. By substituting the Josephson equations for the voltage and the current into Eq. 2.4, we get:

$$U_J = (\frac{\hbar}{2e})\int_0^t I(\frac{d\varphi}{dt})dt = (\frac{\hbar}{2e})I_c\int_0^\varphi \sin\varphi d\varphi = E_j(1-\cos\varphi), \tag{2.5}$$

where $E_j = (\frac{\hbar}{2e})I_c$ is the so-called Josephson energy of the junction, we can think of Eq 2.5 as the effective potential energy of the Josephson junction as a function of the junction phase.

(a)

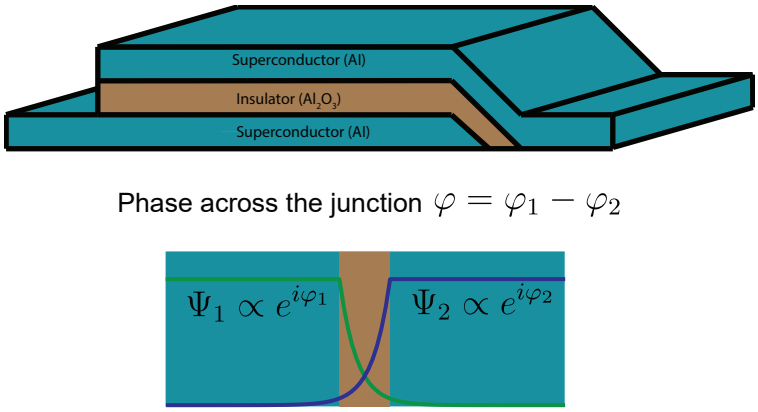

(b)

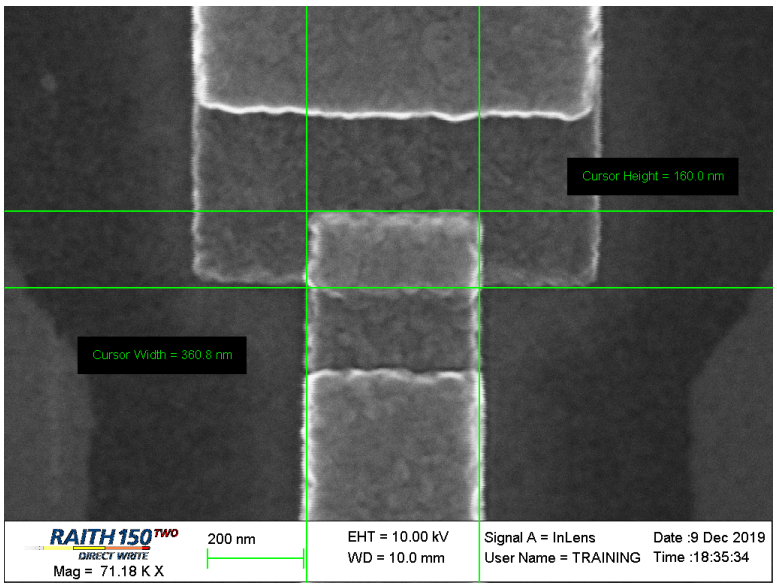

Figure 2.1: The Josephson Junction. (Top) Schematic representation of a Josephson junction, composed of a sandwich of superconductor-insulator-superconductor (S-I-S) layers. The wavefunction of the supercurrent extends through the barrier with nonzero probability, allowing for the quantum tunneling of Cooper pairs through the barrier. (Bottom) Scanning electron microscopy (SEM) image of Josephson junction fabricated using the Dolan technique, which employs double-angle evaporation. The Josephson energy, E_J is proportional to its area, indicated by the green rulers, which define the overlap region of the S-I-S layers.

2.2 SQUID

The superconducting quantum interference device (SQUID) is a loop created by connecting a pair of junctions in parallel. The SQUID is sensitive to external magnetic field threading the loop, making it useful for many applications, including magnetic field sensors and tunable c-QED elements such as qubits and cavities. The macroscopic wavefunction in superconductors constrains the phases of the parallel junctions, φ_α and φ_β. To show that, we start with the supercurrent equation that describes the phase across a superconductor [12]

$$-\frac{2\pi\lambda_L^2\mu_0}{\Phi_0}\mathbf{J} - \frac{2\pi}{\Phi_0}\mathbf{A} = \nabla\varphi, \tag{2.6}$$

where λ_L is the material's penetration depth at which the current density vanishes, $\mathbf{J}$ is the current density, $\mathbf{A}$ is the electromagnetic vector potential, and φ is the wavefunction's phase.

To relate the junction phases, we can take a line integral along the SQUID loop. We can choose the counter to be inside the cross-section of the superconductor where $\mathbf{J} = 0$. This simplifies the supercurrent equation by eliminating the second term, resulting in $\nabla\varphi = -\frac{2\pi}{\Phi_0}\mathbf{A}$. To this end, we proceed by taking the line integral around the closed path of the SQUID loop,

$$\oint \nabla\varphi \cdot dl = \int \nabla\varphi_\beta + \int \nabla\varphi_\alpha - \frac{2\pi}{\Phi_0}\int_{leads} \mathbf{A}\cdot dl = \varphi_\beta - \varphi_\alpha - \frac{2\pi}{\Phi_0}\oint \mathbf{A}.\cdot dl. \tag{2.7}$$

The line integral of the gradient $\nabla\varphi$ at the junctions equals the phase difference across the junctions. On the other hand, the simplified supercurrent equation is applied for the remaining part as it consists of superconductor paths, where the gradient $\nabla\varphi$ substituted by the vector potential, $\mathbf{A}$.

Now, we consider the SQUID loop in the presence of an external magnetic field. The total flux threading the loop, Φ_{ext}, can be expressed as the line integral of the vector potential along the SQUID loop $\Phi_{ext} = \oint \mathbf{A}\cdot dl$. Substiting this in Eq. 2.7 gives:

$$\oint \nabla\varphi \cdot dl = \varphi_\beta - \varphi_\alpha - 2\pi\frac{\Phi_{ext}}{\Phi_0} \tag{2.8}$$

To ensure that the wavefunction phase is single-valued and continuous around the SQUID loop, the total phase change must be a multiple of 2π, as the wavefunction must have same value when takes a round-trip and return to the same location. This results in the final

relation between the external field and SQUID phases which allows us to control the phase difference $\varphi_\beta - \varphi_\alpha$ by applying an external magnetic field:

$$2\pi n = \varphi_\beta - \varphi_\alpha - 2\pi \frac{\Phi_{ext}}{\Phi_0} \tag{2.9}$$

We move on to construct the SQUID energy and use the relation in Eq. 2.9 to write it in terms of the external flux. In the SQUID circuit shown in Figure 2.2, the total current flowing in one direction can be expressed in terms of a sum of junction currents as

$$I_{sq} = I_{c,\alpha} \sin \varphi_\alpha + I_{c,\beta} \sin \varphi_\beta. \tag{2.10}$$

Following the previous section, the SQUID energy reads,

$$U_{SQ} = -E_{j,\alpha} \cos \varphi_\alpha - E_{j,\beta} \cos \varphi_\beta. \tag{2.11}$$

By using an external magnetic flux to control the phase difference in Eq. 2.9 at $n = 0$, there is only one true degree of freedom, namely the phase sum, which we call φ_{sq}. We define the junction phases in terms of Φ_{ext} and φ_{sq}, [14].

$$\varphi_{sq} = \frac{\varphi_\beta + \varphi_\alpha}{2} \tag{2.12}$$

$$\varphi_\alpha = \varphi_{sq} - \pi \frac{\Phi_{ext}}{\Phi_0} \tag{2.13}$$

$$\varphi_\beta = \varphi_{sq} + \pi \frac{\Phi_{ext}}{\Phi_0} \tag{2.14}$$

The SQUID energy, then, can be re-written as:

$$U_{SQ} = -(E_{j,\alpha} + E_{j,\beta}) \cos\left(\pi \frac{\Phi_{ext}}{\Phi_0}\right) \cos(\varphi_{sq}) - (E_{j,\alpha} + E_{j,\beta}) \sin\left(\pi \frac{\Phi_{ext}}{\Phi_0}\right) \sin(\varphi_{sq}) \tag{2.15}$$

Redefining the constant prefactors as $E_\Sigma = E_{j,\alpha} + E_{j,\beta}$ and $E_\Delta = E_{j,\alpha} - E_{j,\beta}$, we reach the final expression:

$$U_{SQ} = -E_\Sigma \cos\left(\pi \frac{\Phi_{ext}}{\Phi_0}\right) \cos(\varphi_{sq}) + E_\Delta \sin\left(\pi \frac{\Phi_{ext}}{\Phi_0}\right) \sin(\varphi_{sq}) \tag{2.16}$$

It is worth noting that the first term is an even function in the external flux while the second term is an odd function. Both terms can be tuned or modulated via the external flux. This will play a vital role in creating the different parametric interactions needed to build our analog quantum simulation platforms.

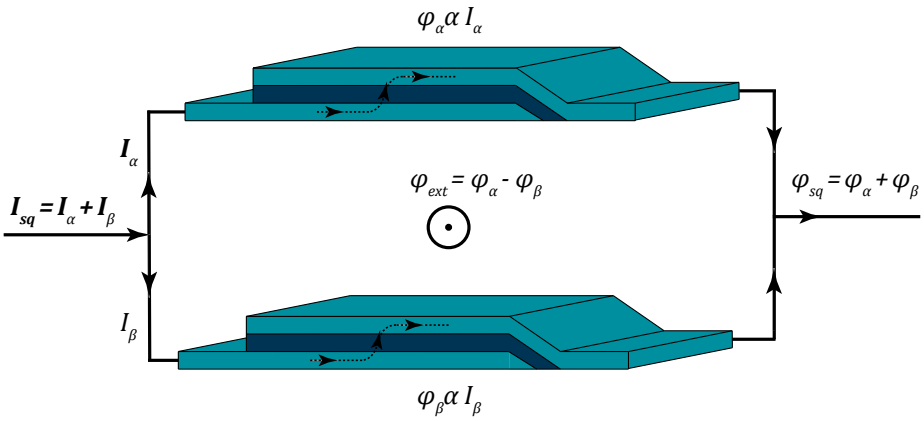

Figure 2.2: Illustration of a Superconducting Quantum Interference Device (SQUID). This device is created by connecting two junctions in parallel, forming a loop. By applying an external magnetic field to the loop, the phase difference between the two junctions can be controlled, enabling control over the effective critical current.

2.3 transmon qubit

During the last two decades, the design of superconducting qubits has improved significantly. The first generation of these qubits was the charge qubit, also known as a Cooper Pair Box (CPB). The CPB essentially consists of a superconducting island connected to a Cooper-pairs reservoir (usually ground) by a Josephson junction. The superconducting island is also coupled to an external voltage source via a gate capacitor. The number of Cooper pairs in the island can be varied by adjusting the island potential, which allows for performing quantum operations on the qubit. However, CPB qubits were found to be highly sensitive to charge noise. To mitigate this problem, the transmon design was developed by shunting the junction with a large capacitor, which increases the ratio of Josephson energy to charging energy to over 100, and hence reduces charge sensitivity.

The simplest circuit for a single qubit often involves a transmon qubit coupled to a readout resonator. We will proceed with deriving the Hamiltonian of a similar circuit, and extract the useful quantities including qubit frequency, anharmonicity, and qubit-resonator dispersive shift.

In a typical derivation of the transmon Hamiltonian, the flux variable ϕ is introduced to describe the magnetic flux of the node [15]. The flux variable equals the time integral of the voltage across the junction and can be directly related to the junction phase via the

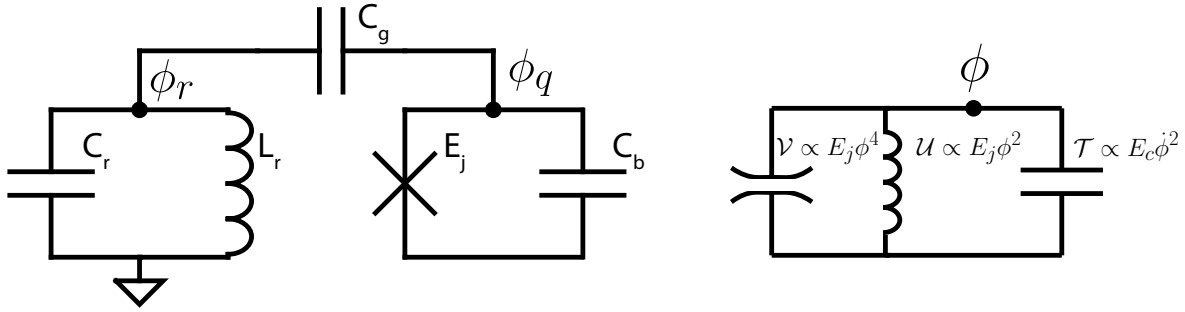

Figure 2.3: An illustration of a transmon coupled to a resonator. (left) The transmon is depicted as a Josephson junction shunted by a large capacitor. The resonator is shown as a parallel LC oscillator, which is capacitively coupled to the qubit and is typically used for readout measurements. (right) A simplified representation of the transmon circuit is shown, where the junction of the qubit is split into two parts, with energies that depend on the qubit flux. These parts are a linear inductor and a nonlinear inductor, representing the fourth-order term of the junction energy expansion. This depiction describes the transmon as an oscillator with a small nonlinear element that can be treated perturbatively.

Josephson equations:

$$\phi = \int_{-\infty}^{t} V dt = \frac{\Phi_0}{2\pi}\varphi \tag{2.17}$$

Writing the junction energy in terms of flux variable, by replacing $\varphi = 2\pi\frac{\phi}{\Phi_0}$, is particularly useful because it allows us to analyze the transmon in terms of a simple harmonic oscillator, which provides a familiar picture. In this sense, the potential energy describes the "fictitious" magnetic energy stored in the Josephson junction associated with flux; in reality, the junction phase. On the other hand, the kinetic energy describes the electrical energy stored in the capacitor associated with the charge, which is related to the flux derivative based on Eq. 2.17, $V = \dot{\phi}$. We proceed with deriving the Lagrangian and Hamiltonian, with the flux being the generalized coordinates that describe the system's degrees of freedom.

The kinetic energy stored in a capacitor is $E = \frac{1}{2}CV_c^2 = \frac{1}{2}C\dot{\phi}^2$. The capacitor flux can be a node flux to the ground or, in the case of coupling capacitors, the flux difference between two nodes at the capacitor ends. In a large network, it is more convenient to write the system's Hamiltonian in matrix form, which we will start practicing now. We aggregate all circuit flux variables in the flux vector, $\Phi = (\phi_q, \phi_r)$. The capacitance matrix in Fig. 2.3

can be easily written as:

$$C = \begin{bmatrix} C_b + C_g & -C_g \\ -C_g & C_r + C_g \end{bmatrix} \tag{2.18}$$

The total kinetic energy reads:

$$\mathcal{T} = \frac{1}{2}\dot{\Phi}^\intercal C \dot{\Phi} \tag{2.19}$$

The potential energy stored as magnetic energy can be stored either in an inductor as $E = \frac{\phi^2}{2L}$ or in the junction associated with the fictitious flux as $E = -E_j \cos\left(2\pi \frac{\phi}{\Phi_0}\right)$. Thus, the total energy stored in our circuit read:

$$\mathcal{U} = -E_j \cos\left(2\pi \frac{\phi_q}{\Phi_0}\right) + \frac{\phi_r^2}{2L_r} \tag{2.20}$$

With both energies, it is straightforward to write the Lagrangian as follows:

$$\mathcal{L} = \mathcal{T} - \mathcal{U} = \frac{1}{2}\dot{\Phi}^\intercal C \dot{\Phi} + E_j \cos\left(2\pi \frac{\phi_q}{\Phi_0}\right) - \frac{\phi_r^2}{2L_r} \tag{2.21}$$

To derive the Hamiltonian, we define the vector conjugate momentum of the coordinate Φ as:

$$\mathcal{Q} = \frac{\partial \mathcal{L}}{\partial \dot{\Phi}} = C\dot{\Phi} \tag{2.22}$$

Redefining $\dot{\Phi}$ in terms of the conjugate momentum:

$$\dot{\Phi} = C^{-1}\mathcal{Q} \tag{2.23}$$

The inverse of the capacitance matrix is simplified by assuming that C_b^2, $C_r^2 \gg C_g^2$ and $C_r + C_g \approx C_r$, and defining the total qubit capacitance as $C_\Sigma = C_b + C_g$. This results in the simplified inverse matrix:

$$C^{-1} = \begin{bmatrix} \frac{1}{C_\Sigma} & \frac{Cg}{C_\Sigma C_r} \\ \\ \frac{Cg}{C_\Sigma C_r} & \frac{1}{C_r} \end{bmatrix} \tag{2.24}$$

The Hamiltonian can then be formulated as follows:

$$\mathcal{H} = \mathcal{Q}\dot{\Phi} - \mathcal{L} = \frac{1}{2}\mathcal{Q}^\intercal C^{-1} \mathcal{Q} - E_j \cos\left(2\pi \frac{\phi_q}{\Phi_0}\right) + \frac{\phi_r^2}{2L_r} \tag{2.25}$$

We can then promote the q and ϕ to operators and impose the canonical commutation relations. Then, we split the Hamiltonian into two decoupled subsystems, and a coupling

Hamiltonian to be treated consecutively. We can carry out the multiplication in the first term of the Hamiltonian given by Eq. 2.25. The first part is the resonator Hamiltonian, the second part is the qubit Hamiltonian, and the third part is the coupling Hamiltonian:

$$\hat{\mathcal{H}} = \hat{\mathcal{H}}_r + \hat{\mathcal{H}}_q + \hat{\mathcal{H}}_c \tag{2.26}$$

$$\hat{\mathcal{H}}_r = \frac{\hat{q}_r^2}{2C_r} + \frac{\hat{\phi}_r^2}{2L_r} \qquad \text{Resonator Hamiltonian} \tag{2.27}$$

$$\hat{\mathcal{H}}_q = \frac{\hat{q}_q^2}{2C_\Sigma} - E_j \cos\left(2\pi \frac{\hat{\phi}_q}{\Phi_0}\right) \qquad \text{Qubit Hamiltonian} \tag{2.28}$$

$$\hat{\mathcal{H}}_c = \frac{C_g}{C_\Sigma C_r} \hat{q}_q \hat{q}_r \qquad \text{Coupling Hamiltonian} \tag{2.29}$$

2.3.1 Resonator Hamiltonian

The Hamiltonian of the LC resonator can be written in a familiar way using the ladder operators as

$$\hat{\mathcal{H}}_r = \hbar\omega_r \, (\hat{a}^\dagger \hat{a} + \frac{1}{2}), \tag{2.30}$$

where the resonator frequency is $\omega_r = \frac{1}{\sqrt{L_r C_r}}$, and the associated lowering and raising operators are defined as

$$\hat{a}_r = +i \frac{1}{\sqrt{2C_r \hbar\omega_r}} \hat{q}_r + \frac{1}{\sqrt{2L_r \hbar\omega_r}} \hat{\phi}_r, \tag{2.31}$$

$$\hat{a}_r^\dagger = -i \frac{1}{\sqrt{2C_r \hbar\omega_r}} \hat{q}_r + \frac{1}{\sqrt{2L_r \hbar\omega_r}} \hat{\phi}_r. \tag{2.32}$$

Conversely, the charge and flux operators then expressed as

$$\hat{q}_r = -i \sqrt{\frac{C_r \hbar\omega_r}{2}} (\hat{a}_r - \hat{a}_r^\dagger) \tag{2.33}$$

$$\hat{\phi}_r = \sqrt{\frac{L_r \hbar\omega_r}{2}} (\hat{a}_r + \hat{a}_r^\dagger). \tag{2.34}$$

The eigenenergies of this Hamiltonian are evenly spaced, $E_n = \hbar\omega_r(n + \frac{1}{2})$, where n is a non-negative integer. The raising and lowering operators, $\hat{a}^\dagger$ and $\hat{a}$, allow for transitioning between the energy levels. While the $\hat{a}^\dagger$ operator increases the energy by $\hbar\,\omega_r$, the $\hat{a}$ operator decreases it by the same amount.

2.3.2 Qubit Hamiltonian

The qubit Hamiltonian in equation 2.28 is written in terms of the charge and flux operators. Nonetheless, it is insightful to change the operators to write Hamiltonian in a form similar to the transmon paper [16]. We define the Cooper-pair number operator $\hat{n}_q = \frac{\hat{q}_q}{2e}$. Here, e is the electron charge, and the factor 2 comes from the fact that a Cooper pair consists of two electrons. In this context, we also define the charging energy $E_c = \frac{e^2}{2C_\Sigma}$, which represents the energy required to add or remove a Cooper pair from the superconductor island.

The qubit Hamiltonian can then be rewritten as

$$\hat{\mathcal{H}}_q = 4E_c\,\hat{n}_q^2 - E_j \cos\hat{\varphi}_q. \tag{2.35}$$

Perturbative approach to transmon qubit

Written in the phase basis, $\hat{\mathcal{H}}_q$ has the form of Mathieu's differential equation, which can be solved exactly in terms of special functions known as Mathieu functions. This approach becomes essentially intractable when multiple coupled qubits are involved. Therefore, it is convenient to develop a perturbative approach to solve $\hat{\mathcal{H}}_q$. We start by expanding the cosine term of $\hat{\mathcal{H}}_q$ to fourth order around the minimum $\varphi = 0$, giving

$$\hat{\mathcal{H}}_q = 4E_c\,\hat{n}_q^2 + E_j\frac{\hat{\varphi}_q^2}{2} + \hat{\mathcal{H}}_p, \tag{2.36}$$

where $\hat{\mathcal{H}}_p$ is the fourth-order term which we will treat later on.

The leading-order Hamiltonian then is identical to the simple harmonic oscillator, and thus we can write it in terms of the raising and lowering operators

$$\hat{\mathcal{H}}_q = \hbar\omega_q(\hat{a}_q^\dagger\hat{a}_q + \frac{1}{2}), \tag{2.37}$$

with the Cooper-pair number and phase operators expressed as

$$\hat{\varphi}_q = \frac{1}{\sqrt{2}}(\frac{8E_c}{E_j})^{1/4}(\hat{a}_q + \hat{a}_q^\dagger), \tag{2.38}$$

$$\hat{n}_q = \frac{-i}{\sqrt{2}}(\frac{E_c}{8E_j})^{1/4}(\hat{a}_q - \hat{a}_q^\dagger). \tag{2.39}$$

Keeping in mind that the number operator is linked to the charge operator by changing the prefactor, let us also define it here as

$$\hat{q}_q = -i\sqrt{\frac{C_\Sigma \hbar\omega_q}{2}}(\hat{a}_q - \hat{a}_q^\dagger). \tag{2.40}$$

Now we starting treating $\hat{\mathcal{H}}_p$ by rewriting it in terms of the lowering and raising operators as

$$\hat{\mathcal{H}}_p = -E_j\frac{\hat{\varphi}_q^4}{24} = -\frac{E_j}{24}(\frac{2E_c}{E_j})(\hat{a}_q + \hat{a}_q^\dagger)^4 = -\frac{E_c}{12}(\hat{a}_q + \hat{a}_q^\dagger)^4. \tag{2.41}$$

Treatment of $\hat{\mathcal{H}}_p$ in 1st order perturbation theory, results in a term that introduces corrections to the diagonal elements of the qubit Hamiltonian as

$$\hat{\mathcal{H}}_p \approx -\frac{E_c}{2}(\hat{a}_q^\dagger\hat{a}_q + \hat{a}_q^\dagger\hat{a}_q\hat{a}_q^\dagger\hat{a}_q). \tag{2.42}$$

While the linear term corrects the harmonic qubit frequency by $E_c/2$, the quadratic term adds the nonlinearity needed for qubit anharmonicity. The full Hamiltonian with correction then reads,

$$\hat{\mathcal{H}} = \hbar\omega_q(\hat{a}_q^\dagger\hat{a}_q + \frac{1}{2}) - \frac{E_c}{2}(\hat{a}_q^\dagger\hat{a}_q\hat{a}_q^\dagger\hat{a}_q + \hat{a}_q^\dagger\hat{a}_q). \tag{2.43}$$

Now we extract the quantities of interest, keeping in mind that the transition frequency of the qubit from $|n\rangle$ to $|n+1\rangle$ can be calculated as $\omega_{n,n+1} = (H|_{m=n+1} - H|_{m=n})/\hbar$. First, the qubit frequency is found to be $\omega_{01} = \sqrt{8E_jE_c}/\hbar - E_c/\hbar$. Second, the anharmonicity of the qubit is found by the energy difference between transitions ω_{12} and ω_{01} , $\alpha = \omega_{12} - \omega_{01} = -E_c$. A typical transmon is designed to suppress the sensitivity t charge noise with $E_j/E_c \geq 20$, while maintaining an anharmonicity of $\alpha/h \geq 200$ MHz. The qubit capacitance is primarily determined by this anharmonicity which allows selective excitation of the first energy state, effectively treating the transmon as a two-level system.

2.3.3 The Dispersve Coupling

In the previous section, we focused on the qubit and ignored its coupling to the resonator. However, to gain a full understanding of the qubit-resonator system, we must consider the coupling term and introduce the concept of qubit-resonator dispersive coupling. The resonator-qubit system is typically used as a subsystem for each qubit added to a multi-qubit system, where coupling to the resonator enables measuring the respective qubit state. In the

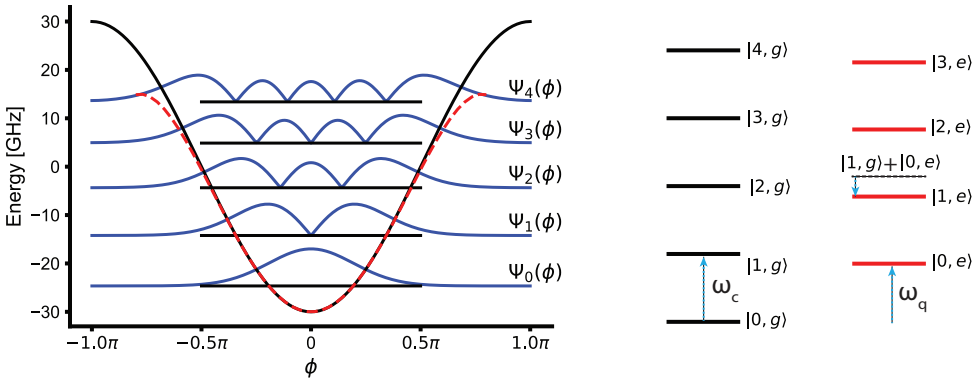

Figure 2.4: Specturm of the transmon qubit and its interaction with the resonator. (Left) Depiction of the absolute value of low-energy eigenfunctions of the qubit in the phase representation. In the transmon regime, the phase variable tends to remain near the minimum of the cosine potential. This allows for approximating the cosine potential to a fourth-order expansion, as indicated by the red dashed line. The uneven spacing between energy levels, due to the cosine potential, enables addressing only the lowest first and second transitions. (Right) Illustration of the energy levels of the qubit-resonator Hamiltonian in the dispersive regime. The energy levels largely do not hybridize, instead, the resonator energy levels are shifted by a small amount, and their spacing is slightly decreased when the qubit is excited, enabling the detection of the qubit state by probing the resonator response.

limit for dispersive , the coupling strength g is much smaller than the frequency detuning Δ, i.e. $\frac{g^2}{\Delta^2} \ll 1$. This condition is essential and we will elaborate on it later.

We can represent the coupling Hamiltonian in Eq. 2.29 in the ladder operator notation using the charge operators' definition for both the transmon qubit in Eq. 2.40 and the resonator in Eq. 2.33 , which we derived earlier.

$$\hat{\mathcal{H}}_c = -\frac{\hbar C_g}{2\sqrt{C_\Sigma C_r}}\sqrt{\omega_q \omega_r}(\hat{a}_q - \hat{a}_q^\dagger)(\hat{a}_r - \hat{a}_r^\dagger) \tag{2.44}$$

Now we recombine the complete system Hamiltonian including the bare resonator and transmon Hamiltonians as

$$\hat{\mathcal{H}} = \hbar\omega_q\, \hat{a}_q^\dagger \hat{a}_q + \hbar\omega_r\, \hat{a}_r^\dagger \hat{a}_r + \hbar g(\hat{a}_q - \hat{a}_q^\dagger)(\hat{a}_r - \hat{a}_r^\dagger), \tag{2.45}$$

where $g = \frac{C_g}{2\sqrt{C_\Sigma C_r}}\sqrt{\omega_q \omega_r}$. The resulting Hamiltonian after the rotating wave approximation (RWA) would be

$$\hat{\mathcal{H}} = \hbar\omega_r\, \hat{a}_r^\dagger \hat{a}_r + \hbar\omega_q\, \hat{a}_q^\dagger \hat{a}_q - \hbar g(\hat{a}_q \hat{a}_r^\dagger + \hat{a}_q^\dagger \hat{a}_r). \tag{2.46}$$

We define the vector representing the system ladder operators, $\hat{A} = (\hat{a}_r, \hat{a}_q)$, and view the Hamiltonian in matrix form as $\hat{\mathcal{H}} = \hat{A}^\dagger M \hat{A}$, where M is:

$$M = \begin{bmatrix} \omega_r & -g \\ -g & \omega_q \end{bmatrix}. \tag{2.47}$$

We apply the Bogoliubov transformation to $\hat{\mathcal{H}}$ in the limit of $\frac{g^2}{\Delta^2} \ll 1$. The system's eigenenergies then reads,

$$\tilde{\omega}_r = \omega_r + \frac{g^2}{\Delta}, \tag{2.48}$$

$$\tilde{\omega}_q = \omega_q - \frac{g^2}{\Delta}, \tag{2.49}$$

and the eigenbasis operators :

$$\begin{bmatrix} \hat{\tilde{a}}_r \\ \hat{\tilde{a}}_q \end{bmatrix} = \frac{1}{\sqrt{g^2 + \Delta^2}} \begin{bmatrix} \Delta & g \\ -g & \Delta \end{bmatrix} \begin{bmatrix} \hat{a}_r \\ \hat{a}_q \end{bmatrix}. \tag{2.50}$$

It is worth noting that the coupling strength g and the calculation of the eigenbasis are also valid for the qubit-qubit couplings when they are first treated as linear oscillators before treating the perturbative parts similar to the following step. The perturbative part

of the transmon qubit Hamiltonian, as given in Eq. 2.42, expressed in terms of the system's eigenbasis operators, gives:

$$\begin{aligned}\hat{\mathcal{H}}_p = & -\frac{E_c}{12}(\hat{a}_q + \hat{a}_q^\dagger)^4 \\ \approx & -\frac{E_c}{12}\Bigg\{6\frac{\Delta^4}{(\Delta^2+g^2)^2}\left(\hat{\tilde{a}}_q^\dagger\hat{\tilde{a}}_q\hat{\tilde{a}}_q^\dagger\hat{\tilde{a}}_q + \hat{\tilde{a}}_q^\dagger\hat{\tilde{a}}_q\right) \\ & + 12\frac{\Delta^2 g^2}{(\Delta^2+g^2)^2}\left(2\hat{\tilde{a}}_q^\dagger\hat{\tilde{a}}_q\hat{\tilde{a}}_r^\dagger\hat{\tilde{a}}_r + \hat{\tilde{a}}_r^\dagger\hat{\tilde{a}}_r + \hat{\tilde{a}}_q^\dagger\hat{\tilde{a}}_q\right) \\ & + 6\frac{g^4}{(\Delta^2+g^2)^2}\left(\hat{\tilde{a}}_r^\dagger\hat{\tilde{a}}_r\hat{\tilde{a}}_r^\dagger\hat{\tilde{a}}_r + \hat{\tilde{a}}_r^\dagger\hat{\tilde{a}}_r\right)\Bigg\}\end{aligned} \tag{2.51}$$

Leaving out $\hat{\tilde{a}}^\dagger\hat{\tilde{a}}$ terms that only introduce constant frequency offset, the expression is simplified in the limit of $\frac{g^2}{\Delta^2} \ll 1$, giving

$$\hat{\mathcal{H}}_p = -\frac{E_c}{2}\hat{\tilde{a}}_q^\dagger\hat{\tilde{a}}_q\hat{\tilde{a}}_q^\dagger\hat{\tilde{a}}_q - 2E_c\frac{g^2}{\Delta^2}\hat{\tilde{a}}_q^\dagger\hat{\tilde{a}}_q\hat{\tilde{a}}_r^\dagger\hat{\tilde{a}}_r - \frac{E_c}{2}(\frac{g}{\Delta})^4\,\hat{\tilde{a}}_r^\dagger\hat{\tilde{a}}_r\hat{\tilde{a}}_r^\dagger\hat{\tilde{a}}_r. \tag{2.52}$$

This expression consists of three terms, with the first being the qubit anharmonicity, which is nearly identical to the one derived for the bare qubit. The second term is the qubit-resonator coupling, also known as the cross-Kerr coupling, which is essential in dispersive readout schemes. The third term represents a weak anharmonicity acquired by the resonator due to its coupling to a highly nonlinear system (qubit), neglected, henceforth, at this level of approximation.

Finally, the Hamiltonian of a qubit dispersively coupled to a resonator reads,

$$\hat{\mathcal{H}} = \hbar\omega_r\hat{\tilde{a}}_r^\dagger\hat{\tilde{a}}_r + \hbar\omega_q\hat{\tilde{a}}_q^\dagger\hat{\tilde{a}}_q - \frac{E_c}{2}\hat{\tilde{a}}_q^\dagger\hat{\tilde{a}}_q\hat{\tilde{a}}_q^\dagger\hat{\tilde{a}}_q - 2\hbar\chi\hat{\tilde{a}}_q^\dagger\hat{\tilde{a}}_q\hat{\tilde{a}}_r^\dagger\hat{\tilde{a}}_r. \tag{2.53}$$

where $\chi = E_c\frac{g^2}{\hbar\Delta^2}$. In the context of quantum computing, it is more convenient to express the transmon qubit in the two-level representation, given its high nonlinearity, giving

$$\hat{\mathcal{H}} = \hbar\frac{\omega_q}{2}\sigma_q^z + \hbar(\omega_r - \chi\sigma_q^z)\hat{\tilde{a}}_r^\dagger\hat{\tilde{a}}_r. \tag{2.54}$$

The dispersive regime is achieved here when the coupling between the qubit and the resonator, g, is much weaker than the frequency detuning, Δ such that the energy exchange between the two systems is negligible. Instead, the resonator frequency becomes dependent on the qubit state, as seen in the second term of the resonator term. This shift can be

detected as a change in the resonator response, which is measured through a scattering matrix or pulsed measurement. When the qubit is excited, the resonator frequency is shifted by 2χ, where the change in the magnitude or phase of the readout pulse can be observed. Dispersive readout has become a widely used technique, as it allows for efficient and non-destructive readout of the qubit state.

2.4 Coplanar Waveguide $\lambda/4$ cavity

In this work, we use a one-dimensional microwave cavity that is constructed from a coplanar waveguide (CPW). The cavity is terminated at one end with a low-impedance component that connects the central conductor to the ground. At the other end, the waveguide is connected to an output transmission line through a capacitor that serves as a semireflective mirror. This design is commonly referred to as a $\lambda/4$ transmission line resonator, where the length of the transmission line is equivalent to a quarter of the wavelength of the fundamental mode.

2.4.1 Transmission Line Theory

Transmission line theory describes the behavior of electromagnetic waves as they travel along a physical medium, such as a cable or a waveguide. The incident wave, $V_+(z,t)$, is the wave that travels in the initial propagation direction through the medium, while the reflected wave, $V_-(z,t)$, is the wave that is created as a result of changes in the impedance of the waveguide. The properties of the transmission line include the characteristic impedance, Z_0, and the complex propagation constant, $\gamma = \alpha + j\beta$, where α is the per-unit-length attenuation constant, and β is the phase change per unit length. We follow the standard approach in this section. The electromagnetic waves can be fully described by the equation:

$$V_\pm(z,t) = V_\pm e^{\mp\gamma z + j\omega t} \tag{2.55}$$

Where V_+ is the complex amplitude of the incident wave, ω is the angular frequency, t is time, and z is the distance along the transmission line.

These are time-varying monochromatic plane waves. Thus, we can separate the time and space variables and study only the spatial component of those waves to solve problems of interest. The total wave describing voltage or current at any point in the transmission line is simply the sum of both incident and reflected waves:

$$V_t(z) = V_+ e^{-\gamma z} + V_- e^{\gamma z} \tag{2.56}$$

$$I_t(z) = I_+ e^{-\gamma z} + I_- e^{\gamma z}. \tag{2.57}$$

The incident and reflected currents in the line can be expressed in terms of the voltage and the characteristic impedance, Z_0, of the line as follows:

$$\frac{V_+}{I_+} = Z_0 = \frac{-V_-}{I_-} \tag{2.58}$$

The load termination of the transmission line imposes a boundary condition that relates the incident and reflected waves through Ohm's law:

$$Z_L = \frac{V_t(0)}{I_t(0)} = Z_0 \frac{V_+ + V_-}{V_+ - V_-} \tag{2.59}$$

The reflected wave amplitude can be defined as a complex ratio of the incident wave, $V_- = \Gamma V_+$, where Γ is the reflection coefficient. This relation is substituted in Eq. 2.59 and then solved for Γ to give

$$\Gamma = \frac{Z_L - Z_0}{Z_L + Z_0}. \tag{2.60}$$

The input impedance of a transmission line is the equivalent impedance seen looking into the input port and is determined by the characteristic impedance of the line and any reflections that occur along it. It can be calculated using Ohm's law:

$$Z_{in}(z) = \frac{V_t(z)}{I_t(z)} = Z_0 \frac{e^{-\gamma z} + \Gamma e^{\gamma z}}{e^{-\gamma z} - \Gamma e^{\gamma z}}, \tag{2.61}$$

where V_- is replaced by the reflection ratio. The expression can be further simplified to reach [17],

$$Z_{in}(z) = Z_0 \frac{Z_L + \ Z_0 \tanh \gamma d}{Z_0 + \ Z_L \tanh \gamma d}. \tag{2.62}$$

2.4.2 Resonance modes of the transmission line $\lambda/4$ cavity

The resonant frequencies of a capacitively coupled $\lambda/4$ transmission line cavity can be determined by considering the properties of the transmission line, including its length. In a lossless transmission line $\alpha = 0$, and $\beta = 2\pi/\lambda = \omega\sqrt{\epsilon_{eff}}/c$, where c is the speed of light and ϵ_{eff} is the effective dielectric constant, which is estimated as the average of air and substrate dielectric constants. The input impedance of the cavity, Z_{cav}, is calculated by first transforming the short circuit boundary condition $Z_L = 0$, across the transmission line of length d as

$$Z_{in}(d)|_{Z_L=0} = j \ Z_0 \tan \beta d. \tag{2.63}$$

After adding the coupling capacitor impedance to $Z_{in}(d)$, the cavity impedance at the input port reads,

$$Z_{cav} = \frac{1}{j\omega C} + j\ Z_0 \tan \beta d. \tag{2.64}$$

The resonance of a cavity occurs when the impedance is purely real, $\mathrm{Im}(Z_{cav}) = 0$ [17]. In the limit of $\omega C \to 0$, which imposes an imperfect open circuit boundary condition, the resonance condition reads,

$$Z_0 \tan \beta d = \infty. \tag{2.65}$$

The solution of this equation is $\beta_m = \frac{2\pi}{d}(1 + 2m)$. This implies an infinite number of resonance modes corresponding to the permissible propagation constant values, with the fundamental mode at $f_0 = \frac{c}{4d\sqrt{\epsilon_e ff}}$. That is, the length of the waveguide equals a quarter of the wavelength of the fundamental frequency $d = \lambda/4$, hence the name. The higher resonance frequencies are multiples of f_0 as follows:

$$f_m = f_0(1 + 2m), \tag{2.66}$$

i.e., the resonator supports an infinite number of resonances that are spaced by $2f_0$.

External Quality factor

In practice, our devices cannot be lossless, as we assumed earlier. There are often internal losses, e.g., due to conductive losses and impurities in the substrate and surface oxides. The energy in the cavity modes gradually dissipates to those internal loss channels. Therefore, we need to retrieve the photons/information from the modes before it dissipates if we want to do any meaningful computation using the modes.

The quality factor (Q) of a resonator can be used to quantify the loss of a resonator. It is defined as the ratio of the energy stored in the resonator to the energy lost per cycle of oscillations [17]. The quality factor can be classified into two types: internal and external. The internal Q factor, Q_i, is determined by the intrinsic loss mechanisms of the cavity. On the other hand, the external Q factor, Q_e, takes into account energy leakage to output transmission lines. The total resonator Q-factor, Q_{tot}, is then defined as

$$\frac{1}{Q_{tot}} = \frac{1}{Q_e} + \frac{1}{Q_i}. \tag{2.67}$$

In the context of our work, cavities are designed to have a lower Q_e compared to Q_i. This means that the external coupling is the primary channel of energy leakage, causing most of the photons in the cavity to leak through to the output transmission line. This is called the over-coupled regime. On the other hand, $Q_e > Q_i$ is known as the under-coupled regime.

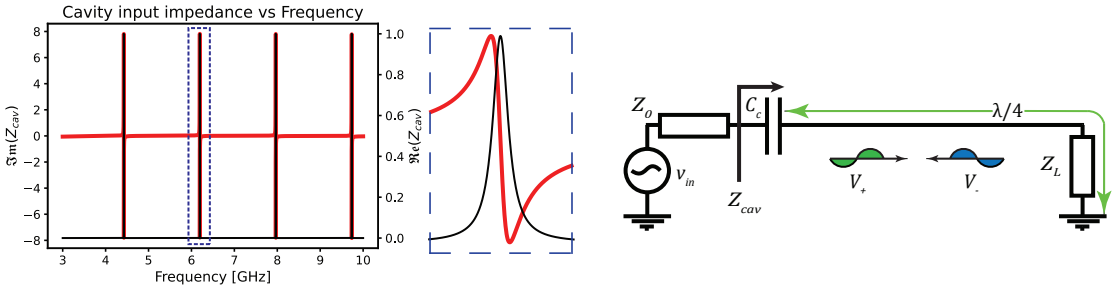

Figure 2.5: Simulation of Lossy Cavity Impedance and Schematic of Transmission Quarter Wavelength Cavity. (Left) The plot shows the numerical simulation of the cavity impedance as a function of frequency. The simulated cavity has a length of 32030 um and is modeled as a lossy system. The imaginary part of the impedance is observed to grow infinitely high (in the case of a lossless cavity), while the total impedance becomes purely real. The real part of impedance represents the internal losses of the cavity. The fundamental mode of the cavity is around 1.5 GHz, and the plot shows the measurement bandwidth, in which about four equally spaced cavity modes can be observed. (Right) The figure depicts a cartoon illustration of a $\lambda/4$ cavity. The cavity is capacitively coupled to the input port, with a characteristic impedance of 50Ω. The cavity can be terminated at the short-circuit end with a load impedance, which can vary depending on the desired results.

Scattering matrix

A standard approach to characterizing microwave systems is known as the scattering matrix. The scattering matrix, S, can be viewed as a linear transfer function of a system in the steady-state regime where a microwave signal is injected into one port while all ports are probed. The matrix element S_{nm} is defined as the ratio of the output signal at port n to the input signal at port m. This can be understood as a linear function in this sense: $V_n = S_{nm}V_m$, where the output voltage is linearly related to the input voltage with a complex factor.

One system of interest is a cavity coupled to a single input/output port with characteristic impedance Z_0. System information, such as resonance frequencies, linewidth, and quality factors, is extracted by measuring the reflection coefficient, $\Gamma(\omega)$. In addition, the coupling regime can also be determined by the phase of the scattering measurement. The reflection measurement, S_{11}, can be analytically expressed as

$$S_{11}(\omega) = \frac{V_-}{V_+} = \Gamma(\omega) = \frac{Z_{cav}(\omega) - Z_0}{Z_{cav}(\omega) + Z_0}. \tag{2.68}$$

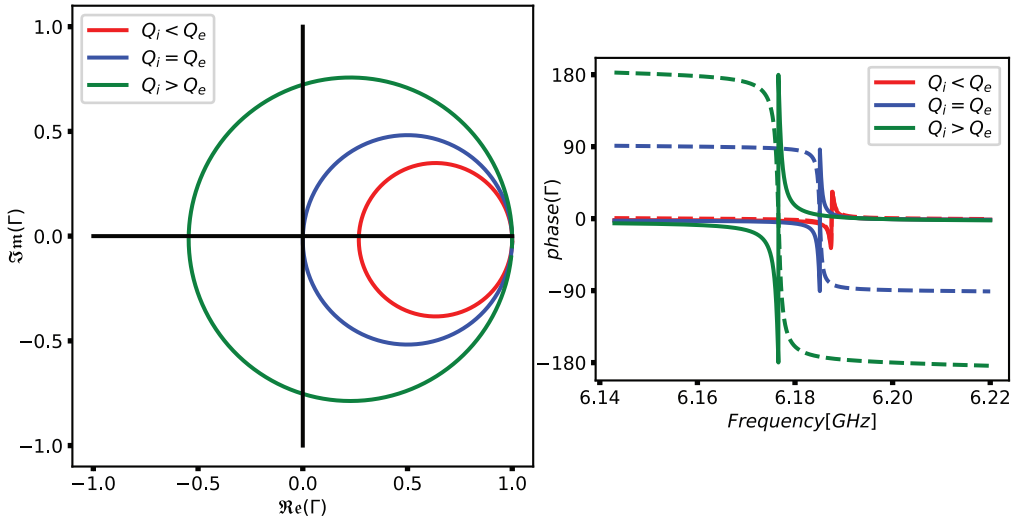

Figure 2.6: Reflection Characterization in the Complex Plane: A Study of the Reflection Coefficient and Phase Trajectory. (Left) The plot shows the reflection coefficient in the complex plane as a function of frequency. The frequency sweep causes the reflection coefficient trajectory to form a circle, $|\Gamma| < 1$. The green circle represents overcoupling, where the trajectory encircles the origin. In the case of critical coupling, shown in blue, the trajectory passes through the origin. In red, undercoupling is depicted, where the circle does not include the origin. (Right) The phase of the reflection coefficient trajectory is plotted as a function of frequency (unwrapped phase shown in dashed lines). The phase wrap is a clear indicator of the type of coupling. In overcoupling, the phase changes by a total of 360^o, while in critical coupling, it changes by only 180^o. In undercoupling, the total phase change does not reach 180^o.

Chapter 3

Superconducting Parametric Cavity as AQS

In this chapter, we introduce our analog quantum simulation platform, which is based on a multimode superconducting parametric cavity. Our platform offers unique design considerations and advantages, which we will discuss in detail. We will highlight the key features that make this platform a suitable choice for quantum simulation, such as uneven mode spacing, parametric interactions enabled by the SQUID, and the ability to program complex coupling terms. Additionally, we will examine the pump schemes used to create the parametric interactions and how to build lattice models. The characterization of the device and the experimental setup will also be discussed.

3.1 Device description

Our platform is a multimode superconducting parametric cavity composed of several resonant modes that share a common boundary condition imposed by a SQUID. We explore the details in the following sections.

3.1.1 Uneven frequency spacing of cavity modes

The eigenmodes of a typical cavity are equally spaced, making it challenging to selectively turn on or off the interaction between these modes using a parametric process. In a parametric process, the interactions are activated by parametric signals that are resonant

with the sum or difference of the modes' frequencies. This means that, with equally spaced modes, all interactions are turned on or off together. However, by making the mode spacing nondegenerate, the resonance frequencies of the different interactions become unique. This allows us to turn on or off any desired number of interactions without affecting stray couplings.

One way of achieving nondegenerate spacing is by modulating the cavity's characteristic impedance along its length, [18]. The dispersion relation becomes highly nonlinear by dividing the cavity length into n sections with varying impedance. We can reasonably estimate the cavity modes and spacing by applying the concept of impedance transformation, as discussed in chapter 2. Here, we transform the load impedance sequentially along different cavity sections until we reach the input port. We label the sections incrementally, with the first section at the load. This can be done by cascading the input impedance Eq. (2.62), giving

$$\begin{aligned} Z_{in,1} =& Z_{0,1}\frac{Z_L + j\ Z_{0,1}\tan\beta a_1}{Z_{0,1} + j\ Z_L \tan\beta a_1} \\ Z_{in,2} =& Z_{0,2}\frac{Z_{in,1} + j\ Z_{0,2}\tan\beta a_2}{Z_{0,2} + j\ Z_{in,1}\tan\beta a_2} \\ & \vdots \\ Z_{in,n} =& Z_{0,n}\frac{Z_{in,n-1} + j\ Z_{0,n}\tan\beta a_n}{Z_{0,n} + j\ Z_{in,n-1}\tan\beta a_n}, \end{aligned}$$

where $Z_{in,m}$ is the input impedance at end of section m , and $Z_{0,m}$ and a_m are the characteristic impedance and the length of section m, respectively. The total cavity impedance follows, similar to that in the previous chapter, by adding the coupling capacitor impedance.

$$Z_{cav} = \frac{1}{j\omega C} + Z_{in,n} \tag{3.1}$$

We design a $\lambda/4$ coplanar waveguide cavity divided into six sections with varied characteristic impedance. The total length of the cavity is $3203\,\mu$m. We compare the cavity response by plotting the phase of the reflection coefficient of our design in contrast to the response of a typical cavity with the same length, as shown in Fig 3.1. Unlike the typical equally spaced modes, the spacing between our cavity modes differs. The unique differences in the mode spacing allow us to assign a distinct modulation frequency for each interaction we target without activating other undesired interactions.

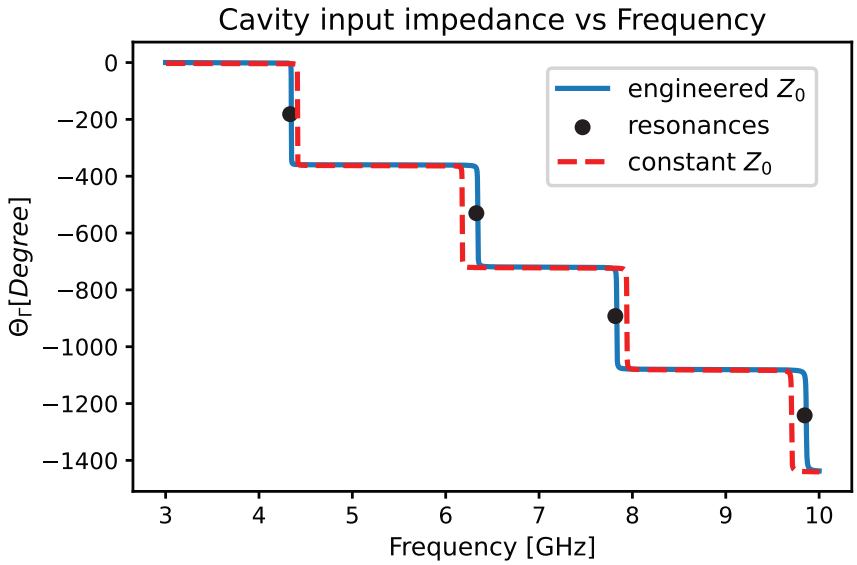

Figure 3.1: The reflection coefficient phase Θ_Γ is shown as a function of frequency. The fundamental mode of the cavity can be found around 1 GHz for both cases, which aligns with the $\lambda/4$ mode of the cavity length. The blue line represents the response of our designed cavity, with the resonance appearing at the center where the phase changes by 360 degrees, marked by black dots. The red dashed line displays the resonances of a typical cavity of the same length. Our designed cavity has shifted modes to nondegenerate resonances, unlike the conventional cavity, where all modes are evenly spaced.

There is no direct method to determine the number of sections and their characteristic impedance. The calculation is done numerically with trial and error where one has to optimize the uneven spacing such that the difference frequencies are unique for every pair of modes. The task becomes increasingly difficult for a large number of modes, as one has to keep track of the difference frequency between all possible pairs. For coherent interactions, the coupling strength between the modes should be in the strong coupling regime. i.e., stronger than the decay rate. Hence, the uniqueness of each pair frequency should be a minimum twice the coupling strength, practically around 20 MHz. In this case, a simple optimization algorithm can be developed to maximize the uniqueness of all pairs of modes as a function of the number of sections and characteristic impedance.

3.1.2 SQUID as a shared boundary condition

In a simple cavity, the mode frequencies are typically determined by the geometry and dielectric constant of the substrate material. This means that those frequencies are set during the design stage and cannot be changed once the cavity has been fabricated. However, it is possible to change the electrical length of the cavity by incorporating a SQUID in place of the short-circuit boundary condition [19]. The SQUID can be controlled by an external flux generated by a coil attached to the sample holder, which allows us to adjust the load impedance of the cavity, and hence its mode frequencies. In the quantum treatment of the transmission line cavity, the cavity modes are quantized, and a flux variable for each mode is defined to be proportional to the bosonic annihilation and creation operators of the mode, $\hat{\phi}_n \propto \hat{a}_n + \hat{a}_n^\dagger$. With the SQUID termination, the Hamiltonian of the system can be approximated as follows:

$$\hat{\mathcal{H}} = \sum_n \omega_n \hat{a}_n^\dagger \hat{a}_n + E_{sq} \cos\left(\pi \frac{\hat{\Phi}_{ext}}{\Phi_0}\right) \cos\left(2\pi \frac{\hat{\phi}_{sq}}{\Phi_0}\right), \tag{3.2}$$

where $\hat{\phi}_{sq}$ is the SQUID flux, and E_{sq} is the Josephson energy of the SQUID.

The mode flux is not point-like; instead, it is distributed along the cavity length and can be expressed arbitrarily as the mode function, $f_n(z)$. Thus, the mode flux can be written with an explicit spatial component as $\hat{\phi}_n(z,t) = f_n(z)\hat{\phi}_n$, describing the flux of mode n at any time t and position z. To this end, the total cavity flux can be written as the sum of all mode fluxes as

$$\hat{\phi}(z,t) = \sum_n f_n(z)\hat{\phi}_n. \tag{3.3}$$

For the impedance-modulated cavity, the mode functions are no longer a simple sinusoid. Instead, they are piecewise functions made from a number of sinusoids that satisfy the appropriate matching boundary conditions at each impedance discontinuity. Still, the conceptual description is the same as that of a simple cavity. In particular, it suffices to treat the SQUID flux, $\hat{\phi}_{sq}$, as the cavity flux at the termination point $z = 0$. Thus, the flux across the SQUID is proportional to the linear combination of all the cavity modes' flux variables, $\hat{\phi}_{sq} = \sum_n \alpha_n \hat{\phi}_n$, where $\alpha_n = f_n(0)$, giving

$$\hat{\mathcal{H}} = \sum_n \omega_n \hat{a}_n^\dagger \hat{a}_n + E_{sq} \cos\left(\pi \frac{\hat{\Phi}_{ext}}{\Phi_0}\right) \cos\left(2\pi \frac{\sum_n \alpha_n \hat{\phi}_n}{\Phi_0}\right). \tag{3.4}$$

Under the assumption of weak nonlinearity, i.e., the cavity linear inductance is much larger than the SQUID effective inductance, the cosine term in the SQUID can be approximated

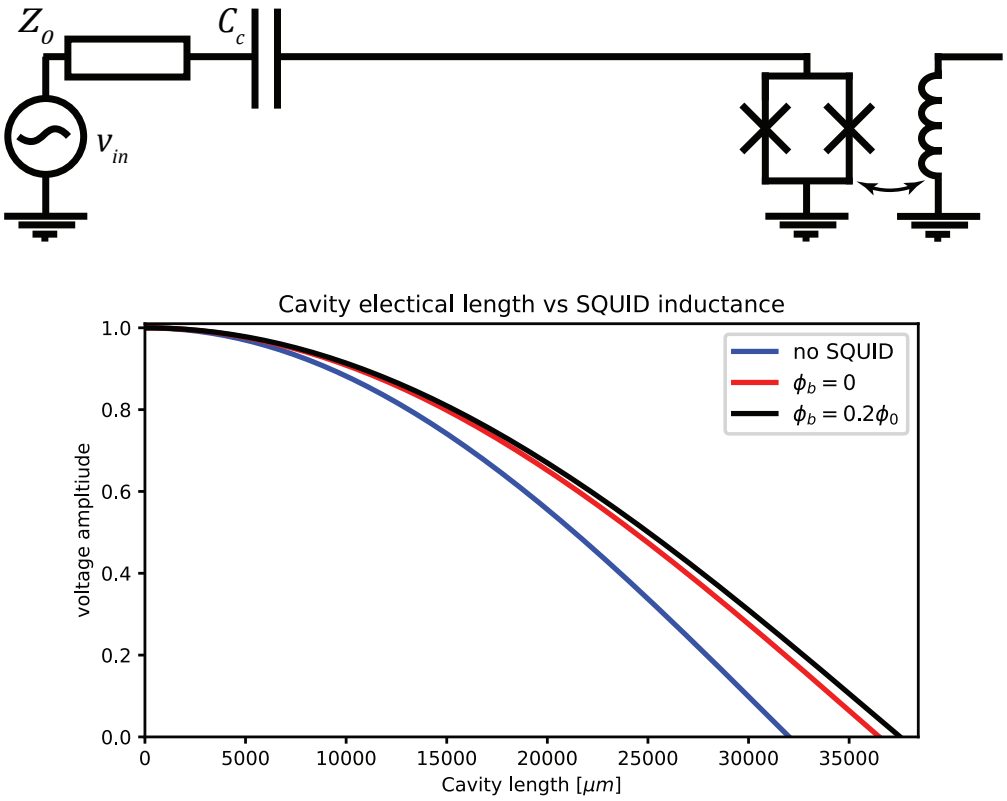

Figure 3.2: Tunable Cavity Design with a SQUID. (top) Schematics of the Cavity Design. The short-circuit boundary condition is replaced with a SQUID. The SQUID loop is inductively coupled to an external magnetic field to enable tuning and modulation of the boundary condition. (bottom) The spatial distribution of the voltage standing wave of the fundamental mode along the cavity. The blue line represents the bare cavity voltage at the short-circuit end, where it reaches zero. On the other hand, when the SQUID is tuned at a specific bias flux value, the voltage at the SQUID appears to extend beyond the cavity length because it corresponds to the fundamental wavelength of a longer cavity. This highlights that the addition of the SQUID acts as a tunable "electrical length.

to second order:

$$\hat{\mathcal{H}} = \sum_n \omega_n \hat{a}_n^\dagger \hat{a}_n - \frac{E_{sq}}{2} \cos\left(\pi \frac{\hat{\Phi}_{ext}}{\Phi_0}\right) (2\pi \frac{\sum_n \alpha_n \hat{\phi}_n}{\Phi_0})^2. \tag{3.5}$$

The external flux on the SQUID loop includes both a DC flux bias, ϕ_b, and an AC flux signal, $\hat{\phi}_p$, also known as a pump, $\hat{\Phi}_{ext} = \phi_b + \hat{\phi}_p$. Assuming $\pi \frac{\hat{\phi}_p}{\Phi_0} \ll 1$, the cosine term of the external flux can be approximated as

$$\cos\left(\pi \frac{\hat{\Phi}_{ext}}{\Phi_0}\right) = \cos\left(\pi \frac{\phi_b + \hat{\phi}_p}{\Phi_0}\right) = \cos\left(\pi \frac{\phi_b}{\Phi_0}\right) \underbrace{\cos\left(\pi \frac{\hat{\phi}_p}{\Phi_0}\right)}_{\approx 1} - \sin\left(\pi \frac{\phi_b}{\Phi_0}\right) \underbrace{\sin\left(\pi \frac{\hat{\phi}_p}{\Phi_0}\right)}_{\pi \frac{\hat{\phi}_p}{\Phi_0}}. \tag{3.6}$$

We can then separate the Hamiltonian into time-independent and time-dependent terms $\hat{\mathcal{H}} = \hat{\mathcal{H}}_0 + \hat{\mathcal{H}}_t$. The time-independent component, $\hat{\mathcal{H}}_0$, captures the static properties of the system, and it is given by

$$\begin{aligned} \hat{\mathcal{H}}_0 &= \sum_n \omega_n \hat{a}_n^\dagger \hat{a}_n - \frac{E_{sq}}{2} \cos\left(\pi \frac{\phi_b}{\Phi_0}\right) (\pi \frac{\sum_n \alpha_n \hat{\phi}_n}{\Phi_0})^2 \\ &= \sum_n \omega_n \hat{a}_n^\dagger \hat{a}_n - \frac{E_{sq}\pi}{2\Phi_0} \cos\left(\pi \frac{\phi_b}{\Phi_0}\right) \sum_{n,m} \alpha_n \alpha_m \hat{\phi}_m \hat{\phi}_n. \end{aligned} \tag{3.7}$$

The second term contributes to the modes' inductive coupling for $n \neq m$. Since the cavity modes are far-detuned, the linear coupling will only result in a slight shift to the original mode frequencies. More interestingly, in the case of $n = m$, the term becomes identical to an effective inductive energy $\propto \hat{\phi}_n^2$, with a tunable inductance $\propto \frac{1}{\frac{E_{sq}\pi}{\Phi_0} \cos\left(\pi \frac{\phi_b}{\Phi_0}\right) \alpha_n^2}$. Thus, this term allows for the tuning of the cavity modes through the DC flux bias ϕ_b. In this view, $\hat{\mathcal{H}}$ can be expressed in terms of tunable mode frequencies, $\omega_n(\phi_b)$, as

$$\hat{\mathcal{H}}_0 = \sum n\omega_n(\phi_b)\, \hat{\tilde{a}}_n^\dagger \hat{\tilde{a}}_n. \tag{3.8}$$

On the other hand, the time-dependent component, $\hat{\mathcal{H}}_t$, is given by:

$$\hat{\mathcal{H}}_t = \frac{\pi E_{sq}}{2\Phi_0} \sin\left(\pi \frac{\phi_b}{\Phi_0}\right) \hat{\phi}_p (2\pi \frac{\sum_n \alpha_n \hat{\phi}_n}{\Phi_0})^2 \tag{3.9}$$

Here, the term represents the interaction between the pump, $\hat{\phi}_p$, and the sum of the mode fluxes, which will enable the parametric interactions between the modes, as discussed in detail in the next section.

3.1.3 Parametric interactions

To use the time-dependent Hamiltonian introduced earlier to create parametric interactions by applying a proper pump signal. First, we must treat $\hat{\mathcal{H}}_t$ perturbatively. Recalling that the mode flux, $\hat{\phi}_n$, can be expressed in terms of the bosonic annihilation and creation operators, that is, $\hat{\phi}_n \propto \hat{a}_n + \hat{a}_n^\dagger$, we can rewrite $\hat{\mathcal{H}}_t$ in terms of the bosonic operators. By expanding the quadratic part, the Hamiltonian can be written as:

$$\hat{\mathcal{H}}_t = g_0(\phi_b)(\hat{a}_p^\dagger + \hat{a}_p)(\sum_{n,m} \hat{a}_n \hat{a}_m^\dagger + \hat{a}_n \hat{a}_m + h.c.) \tag{3.10}$$

Note that we have simplified the term for clarity. The pump is represented in terms of its bosonic operators, $\hat{\phi}_p \propto \hat{a}_p^\dagger + \hat{a}_p$. The coupling strength, $g_0(\phi_b)$, encompasses the sine term of the DC flux bias and all constants resulting from the quadratic expansion, while assuming that α_n is equal for all modes. It is also clear that the interaction strength is a function of the DC flux bias.

In the limit of a strong coherent signal, the pump can be represented by a complex number, α_p, which characterizes the amplitude and phase of the coherent state. It is done by transforming the pump bosonic operators through a displacement transformation [20]:

$$\hat{\tilde{a}}_p = \hat{a}_p + \alpha_p \tag{3.11}$$

where $\tilde{a}_p$ is the transformed annihilation operator. The $\hat{\mathcal{H}}_t$ can then be rewritten as

$$\hat{\mathcal{H}}_t = g_0(\phi_b)\,[\cancelto{0}{(\hat{\tilde{a}}_p^\dagger + \hat{\tilde{a}}_p)} - (\alpha_p + \alpha_p^*)]\,(\sum_{n,m} \hat{a}_n \hat{a}_m^\dagger + \hat{a}_n \hat{a}_m + h.c.) \tag{3.12}$$

In this rewritten form, the first term inside the square brackets, $(\hat{\tilde{a}}_p + \hat{\tilde{a}}_p^\dagger)$, contains the quantum fluctuations associated with the mode signal, which we ignore. The second term, $(\alpha_p + \alpha_p^*)$, is a classical signal that is proportional to the amplitude and phase of the coherent state. In other words, it is the expectation value of the mode operators in a large-amplitude coherent state.

Including the mode energies, $\hat{\mathcal{H}}_0$, the full Hamiltonian is:

$$\hat{\mathcal{H}} = \hat{\mathcal{H}}_0 + g_0(\phi_b)\,(\alpha_p + \alpha_p^*)\,(\sum_{n,m} \hat{a}_n \hat{a}_m^\dagger + \hat{a}_n \hat{a}_m + h.c.) \tag{3.13}$$

To clearly capture the interesting dynamics, we move to the interaction picture via the unitary transformation $U = e^{\frac{i}{\hbar}\mathcal{H}_0 t}$. Also, we write explicitly the temporal components of

the pump signal,

$$\begin{aligned}\hat{\mathcal{H}}_{int} &= i\hbar\dot{U}U^{\dagger} + U\hat{\mathcal{H}}U^{\dagger} \\ &= g_0(\phi_b)\,(\alpha_p e^{-i\omega_p t} + \alpha_p^* e^{i\omega_p t})\,(\sum_{n,m} \hat{a}_n\hat{a}_m^{\dagger} e^{-i\,(\omega_n-\omega_m)\,t} + \hat{a}_n\hat{a}_m e^{-i\,(\omega_n+\omega_m)\,t} + h.c.) \\ &= \; g_0(\phi_b)\,\alpha_p^* \sum_{n,m} (\hat{a}_n\hat{a}_m^{\dagger} e^{-i\,[(\omega_n-\omega_m)-\omega_p]\,t} + \hat{a}_n\hat{a}_m e^{-i\,[(\omega_n+\omega_m)-\omega_p]\,t}) + h.c.\end{aligned} \tag{3.14}$$

Since cavity modes have different frequencies, most terms in the Hamiltonian are fast oscillating and have weak effects. However, by setting the pump signal frequency to cancel out some terms, time-independent interaction can be achieved. On the AQS platform, two types of interaction are of interest: hopping and pairing interactions.

The hopping interaction can be activated by choosing a pump frequency that resonates with the first term in $\hat{\mathcal{H}}_{int}$, $\omega_p = \omega_n - \omega_m$, [18]. The rotating-wave approximation is used to ignore the effect of the fast oscillating terms, leading to the hopping interaction Hamiltonian,

$$\hat{\mathcal{H}}_{hopping} = g_0(\phi_b)\,|\alpha_p|\,(e^{-i\theta_p}\hat{a}_n\hat{a}_m^{\dagger} + h.c.). \tag{3.15}$$

Similarly, the pairing interaction can be activated by choosing a pump frequency that resonates with the second term in $\hat{\mathcal{H}}_{int}$, $\omega_p = \omega_n + \omega_m$,[21, 22]. The rotating-wave approximation is used to reach the pairing interaction Hamiltonian

$$\hat{\mathcal{H}}_{pairing} = g_0(\phi_b)\,|\alpha_p|\,(e^{-i\theta_p}\hat{a}_n\hat{a}_m + h.c.). \tag{3.16}$$

Notice here that the pump amplitude and phase give us control over the interaction strength as well as the well-defined phase of the interaction. This gives us the ability to create those interactions as desired between any two modes with varying strengths and phases. The prefactor, $g_0(\phi_b)$, can suppress or enhance these interactions, and thus the SQUID needs to be biased to achieve a nonzero value to enable these parametric interactions.

3.1.4 Lattice programming

The quantum systems in which we are interested are typically represented as lattices connected by interactions in spatial dimensions. In this platform, we instead represent these lattices by constructing them in the frequency dimension, where the cavity modes serve as the lattice sites, and the interactions are realized through parametric interaction. By using a set of pump signals, we can create hopping or pairing interactions between pairs of

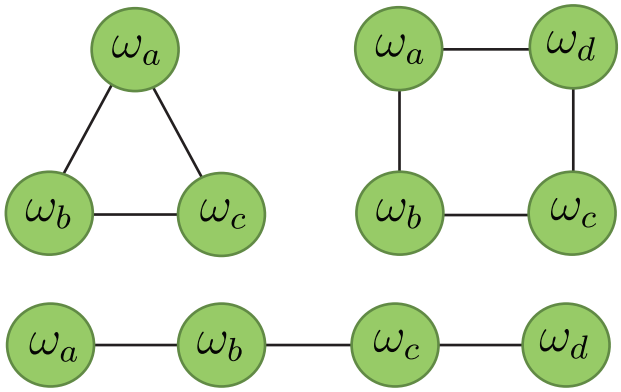

Figure 3.3: Graphical representation of three different shapes of lattices in a many-body quantum system that can be implemented using the multimode superconducting parametric cavity platform. The sites, represented as cavity modes in green circles, are aligned in a straight line, square, and triangle pattern, with lines between the sites representing a type of interaction. This illustration highlights the versatility of modeling quantum systems on an arbitrary lattice structure.

cavity modes, thereby programming a graph of connections representing the desired lattice model, illustrated in Fig. 3.3. In the literature, this has been referred to as using "synthetic dimensions".

With the choice of pump frequency, we selectively activate interaction between specific pairs of modes. This is made possible by the uneven spacing of the cavity modes, which allows for unique modulation frequencies for each interaction between any two sites, as shown in Fig. 3.4. The parametric interactions are controlled by the pump strength and phase. This allows us to control the phase of the coupling strength and implement models with complex hopping and pairing terms, providing a deeper understanding of the underlying physics of the quantum systems being studied.

3.2 Device Operation

3.2.1 Overview of the parametric cavity

The superconducting parametric cavity developed in this research consists of a long transmission line quarter-wavelength cavity with five accessible modes within the measurement bandwidth of 4-12 GHz and a SQUID serving as a tunable inductor shared by all cavity

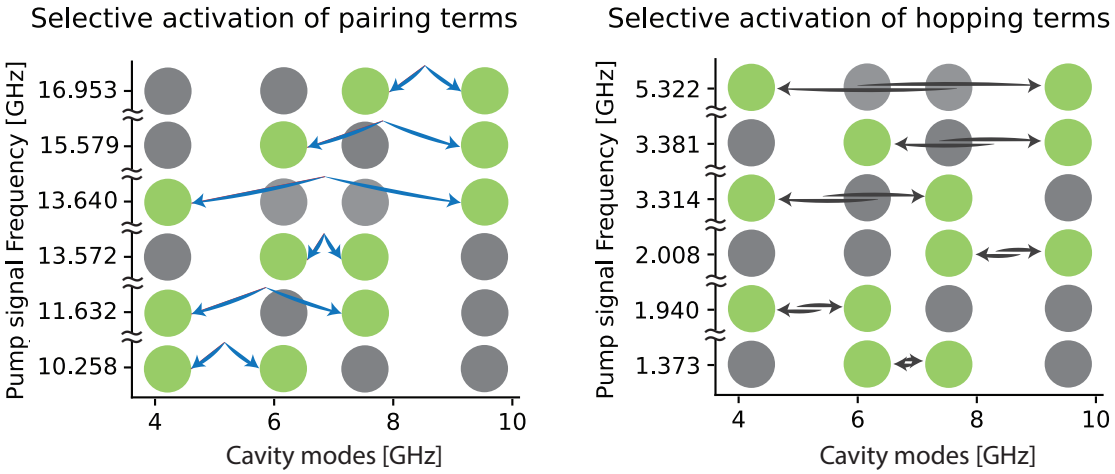

Figure 3.4: Illustration of the selective activation feature in our multimode superconducting parametric cavity platform. The x-axis represents the frequency of the cavity modes, while the y-axis represents the frequency of the parametric signal. As the parametric frequency is varied, a specific interaction between a pair of modes is activated. Each row shows four cavity modes in gray. When the parametric signal is at resonance, only two modes turn green when the interaction between them is activated. The arrow represents the link interaction, highlighting the ability to selectively activate interactions between specific pairs of modes. This feature enables the implementation of specific lattice structures and provides a powerful tool for simulating quantum systems.

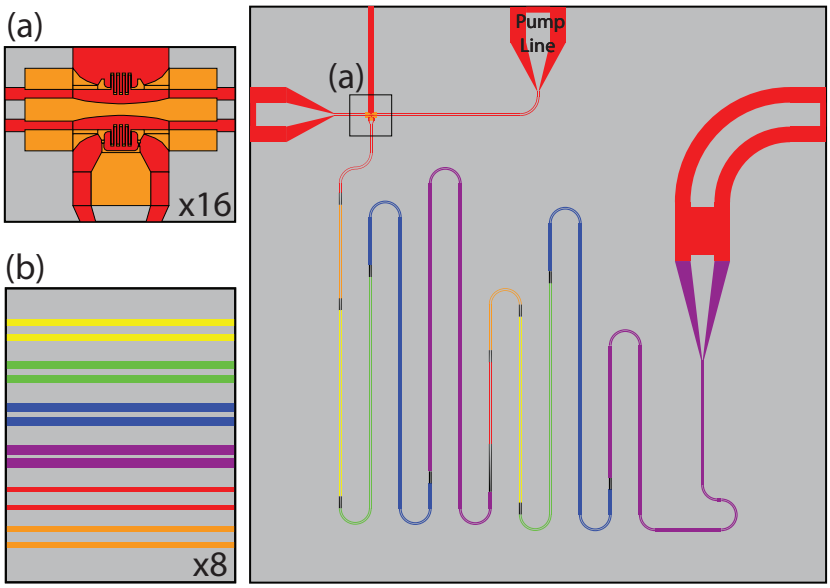

Figure 3.5: CAD design of superconducting parametric cavity. (a) The SQUID acts as a boundary condition and is inductively coupled to a pump line (scaled by a factor of 16). (b) The colored sections of the cavity possess varying characterizing impedance (scaled by a factor of 8).

modes, modulated parametrically. The cavity impedance is modulated to create nondegenerate spacing between the cavity modes, enabling the addressing of individual mode couplings. The cavity is capacitance coupled to a transmission line for probing and performing experiments.

3.2.2 The experimental and measurement setup

The experimental setup for our superconducting parametric cavity involves cooling the device down using a cryogenic-free dilution refrigerator that can reach a temperature of 7 mK. The fridge is composed of five cooling stages, as shown in Fig. 3.6. Microwave signals are transmitted to the device through 50 ohm SMA cables after significant attenuation through the input line and pump line. The output of the cavity is connected to an amplifier chain, starting with a HEMT amplifier at 4 K, to enhance the signal before it reaches room temperature for further amplification. A coil is mounted in very close proximity to the device to adjust the DC flux while the parametric modulation of the SQUID is achieved

through an on-chip fast-flux line terminated by a 50 Ω terminator.

Circulators are used to help isolate input and output signals in a single input/output device, allowing for the measurement of the device's reflection without affecting the incident signal. A set of pump signals is combined at room temperature and fed through the pump line. The input signal to the device can either be from VNA when we perform spectrum measurements or from arbitrary wave generators where the output is measured via a set of digitizers for time-domain measurement.

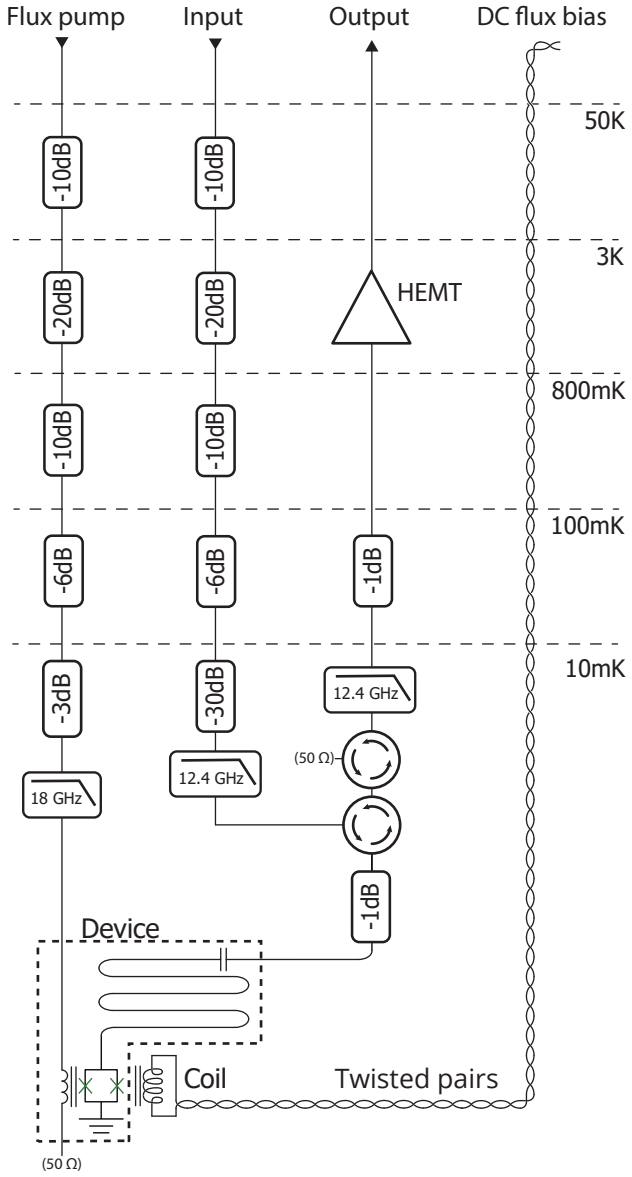

Figure 3.6: The cryogenic microwave network of the experimental setup

Chapter 4

Creutz Ladder Experiment

4.1 Introduction

This chapter shows our platform's potential for analog quantum simulation (AQS) to study classically intractable systems. AQS offers a near-term solution to unlocking the power of quantum computing by constructing a well-controlled artificial system with the same Hamiltonian as the system of interest. We present an *in situ* programmable platform for AQS based on a multimode superconducting parametric cavity for Hamiltonians of hopping terms with arbitrary complex amplitudes.

Our key contribution is the demonstration of the feasibility of simulating topological models such as the bosonic Creutz ladder (BCL) using our platform [23, 24, 25]. The BCL is a simple quasi-1D lattice model, but nonetheless exhibits a wide range of interesting behavior including topological and chiral states. It is historically important as one of the first models of chiral lattice fermions [23, 26]. Our implementation of the BCL simulation highlights the potential of AQS as a powerful simulation tool for quantum systems.

We will discuss the characterization of the device and the realization of a 4-site BCL model. we will also present the measurements and discuss the observation of emerging topological features of the BCL model. We will conclude by emphasizing the advantages of our AQS device compared to competing platforms. This chapter is is largely adapted from our publication [27], first co-authored with Jimmy Hung . The contributions of the authors are as follows.

- The theory team, comprised of E. Solano, H. Alaeian, and E. Rico, formulated the theoretical framework for using the device in simulating the BCL model.

- Jimmy Hung and I shared equal responsibility for conducting the experiments and collecting data.
- I took the lead in fitting the data to the scattering model discussed later and reconstructing the model's Hamiltonian.
- With the exception of the design and fabrication team, all authors contributed to the interpretation of the results and provided valuable insights.
- Sandbo Chang designed the device and, with assistance from Vadiraj A. M. and Ibrahim Nsanzineza, fabricated it.
- Jimmy Hung and I were jointly responsible for writing the majority of the manuscript, while the theory team authored the theory section. All authors, except the design and fabrication team, participated in reviewing and editing the manuscript.

4.2 Bosonic Creutz Ladder Theory

The Hamiltonian of the infinite Creutz ladder, illustrated in Fig. 4.1, is ($\hbar = 1$)

$$\begin{aligned}\hat{\mathcal{H}}_C = -\sum_n \Big[t_d \left(\hat{b}_n^\dagger \hat{a}_{n+1} + \hat{a}_n^\dagger \hat{b}_{n+1} \right) + \frac{t_v}{2} \left(\hat{b}_n^\dagger \hat{a}_n + \hat{a}_{n+1}^\dagger \hat{b}_{n+1} \right) \\ + t_h e^{i\frac{\phi}{2}} \left(\hat{a}_{n+1}^\dagger \hat{a}_n + \hat{b}_n^\dagger \hat{b}_{n+1} \right) \Big] + \text{H.C.},\end{aligned} \tag{4.1}$$

where t_d, t_v, t_h are the diagonal, vertical, and horizontal coupling rates and $\phi/2$ is the phase of the horizontal coupling. This Hamiltonian describes the dynamics of a crossed-link fermionic ladder in a magnetic field [23]. There are a number of interesting topological features of the model. As elaborated in previous work [24], at $\phi = \pi$, the Hamiltonian is time-reversal, particle-hole, and chiral symmetric. Moreover, in the so-called strong coupling limit of $t_v = 0$ and $t_d = t_h = 1$ and with open boundary conditions (finite chain), there are two chiral zero-energy modes localized at the two ends of the ladder. Here, we study the simplest building block one can use to investigate the chiral properties of the Creutz ladder.

We can program the bosonic version of $\hat{\mathcal{H}}_C$ into our parametric cavity with the appropriate choice of pump frequencies. For ease of notation, we will now drop the $\{\hat{a}_n, \hat{b}_n\}$ notation of Eqn. 4.1 and simplify to $\{\hat{a}_n\}$ with the connectivity of the lattice now encoded in a coupling tensor g_{nm}.

To probe the system, we must couple it to our measurement line, which we model with the coupling Hamiltonian

$$\hat{\mathcal{H}}_P = i \sum_n \sqrt{\kappa_n^{\text{ext}}} \left(\hat{a}_{i,n} - \hat{a}_{i,n}^\dagger \right) \left(\hat{a}_n + \hat{a}_n^\dagger \right), \tag{4.2}$$

with $\hat{a}_{i,n}$ describing the annihilation operator of the n^{th} input mode with the external coupling rate κ_n^{ext}.

To treat the dynamics of our driven, dissipative system, we use the following Lindblad master equation [28, 29]

$$\dot{\hat{\rho}} = -i \left[\hat{\mathcal{H}}_C + \hat{\mathcal{H}}_P, \hat{\rho} \right] + \sum_n \kappa_n \left(\hat{a}_n \hat{\rho} \hat{a}_n^\dagger - \frac{1}{2} \{ \hat{a}_n^\dagger \hat{a}_n, \hat{\rho} \} \right),$$

where $\hat{\rho}$ is the reduced density matrix of the plaquette and $\kappa_n = \kappa_n^{\text{ext}} + \kappa_n^{\text{int}}$ is the total photon decay rate including the internal loss rate κ_n^{int}. Here we are mainly interested in the dynamics of cavity modes so the transmission-line bath can be integrated out in the typical Lindblad form. The material loss inside the cavity leads to additional decay which could either be included as a non-Hermitian term κ_n^{int} or directly incorporated in the Lindblad form. If the latter, their noise input contribution and corresponding input/output formalism must be treated differently. While the coupling to the transmission line leads to input noise terms, the internal loss noise contribution should be governed by the fluctuation-dissipation theorem at the equilibrium temperature.

The Heisenberg-Langevin equations of motion for the mode operators follow directly as

$$\dot{\hat{a}}_n = i \left(\Delta_n + i \frac{\kappa_n}{2} \right) \hat{a}_n + i \sum_{m \neq n} \frac{g_{nm}}{2} \hat{a}_m + \sqrt{\kappa_n^{\text{ext}}} \hat{a}_{i,n}, \tag{4.3}$$

where $\Delta_n = \omega_n^s - \omega_n$ with ω_n^s being the probe frequency of the n^{th} mode. Using the input-output formalism, the output modes which we detect are then defined as $\hat{a}_{o,n} = \sqrt{\kappa_n^{\text{ext}}} \hat{a}_n - \hat{a}_{i,n}$. Finally, to find the scattering matrix, we solve for the steady-state solutions of Eqn. 4.3, *i.e.*, assuming $\dot{\hat{a}}_n = 0$, and define $S_{nm} = \langle \hat{a}_{o,n} | \hat{a}_{o,n} \rangle \,/\, \langle \hat{a}_{i,m} | \hat{a}_{i,m} \rangle$.

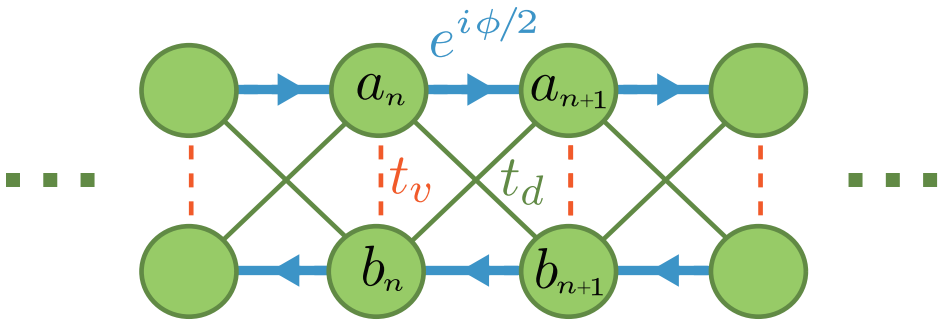

Figure 4.1: Schematic representation of the Creutz ladder. The arrows indicate the sign of the hopping phase.Reproduced from [27], with permission.

4.2.1 Scattering Matrix for an effective non-Hermitian Hamiltonian

Following Ref. [30], the same scattering equations can also be derived as the Heisenberg equations of motion of an effective non-Hermitian model Hamiltonian describing four parametrically coupled resonator modes with frequencies ω_a, ω_b, ω_c and ω_d, loss rates κ_a to κ_d , and a time-dependent coupling rate per link $g_{nm}(t) = |g_{nm}| \cos(\omega_{nm}^{p} t + \phi_{nm})$. The Hamiltonian is

$$\hat{\mathcal{H}} = \sum_{n=1}^{4} \left(\omega_n - i\frac{\kappa_n}{2}\right) \hat{a}_n^\dagger \hat{a}_n + i\sqrt{\kappa_n^{\text{ext}}}(\hat{a}_{\text{i},n} - \hat{a}_{\text{i},n}^\dagger)(\hat{a}_n^\dagger + \hat{a}_n) - \sum_{m\neq n} g_{nm}(t)(\hat{a}_n^\dagger + \hat{a}_n)(\hat{a}_m^\dagger + \hat{a}_m), \quad (4.4)$$

assuming that the cavities are probed at ω_n^{s} and ω_m^{s} where $\omega_m^{\text{s}} > \omega_n^{\text{s}}$. The pump tone frequency is set at $\omega_{\text{p}}^{\text{s}} = \omega_m^{\text{s}} - \omega_n^{\text{s}}$. Moving to the interaction picture and taking the appropriate rotating-wave approximation, we find

$$\begin{aligned} \hat{\mathcal{H}}_{int} = & \sum_{n=1}^{4} \left(\omega_n - \omega_n^s - i\frac{\kappa_n}{2}\right) \hat{a}_n^\dagger \hat{a}_n \\ & + i\sqrt{\kappa_n^{\text{ext}}}(\hat{a}_{\text{i},n}\hat{a}_n^\dagger - \hat{a}_{\text{i},n}^\dagger \hat{a}_n) \\ & - \sum_{m\neq n} \frac{|g_{nm}|}{2}(e^{i\phi_{nm}} \hat{a}_n^\dagger \hat{a}_m + e^{-i\phi_{nm}} \hat{a}_n \hat{a}_m^\dagger). \end{aligned} \quad (4.5)$$

The steady-state equations of motion of the steady-state solutions then follows as

$$i\sqrt{\kappa_n^{\text{ext}}}\hat{a}_{\text{i},n} = \left(\omega_n^{\text{s}} - \omega_n + i\frac{\kappa_n}{2}\right)\hat{a}_n + \sum_{m\neq n}\frac{|g_{nm}|}{2}e^{i\phi_{nm}}\hat{a}_m \tag{4.6}$$

Defining the normalized coupling as $\beta_{nm} = |g_{nm}|e^{i\phi_{nm}}/2\sqrt{\kappa_n\kappa_m}$, and the normalized detuning is defined as

$$\tilde{\Delta}_n = \frac{\omega_n^{\text{s}} - \omega_n}{\kappa_n} + \frac{i}{2} \tag{4.7}$$

The equation of motion becomes

$$i\sqrt{\kappa_n^{\text{ext}}}\hat{a}_{\text{i},n} = \kappa_n\tilde{\Delta}_n\hat{a}_n + \sum_{m\neq n}\sqrt{\kappa_n\kappa_m}\beta_{nm}\hat{a}_m. \tag{4.8}$$

For larger systems, formulating the EOMs describing the system in matrix form becomes useful. First, we define a number of vectors representing the cavity mode operators as $\mathbf{A} = (\hat{a}_1, \ldots, \hat{a}_n)^T$, the input modes $\mathbf{A}_{\text{in}} = (\hat{a}_{\text{i},1}, \ldots, \hat{a}_{\text{i},n})^T$ and output modes $\mathbf{A}_{\text{out}} = (\hat{a}_{\text{o},1}\ldots, \hat{a}_{\text{o},n})^T$. Also, we define the total loss matrix $\mathbf{K} = \text{diag}(\sqrt{\kappa_1}, \ldots, \sqrt{\kappa_n})$ and the external loss $\mathbf{K}^{\text{ext}} = \text{diag}(\sqrt{\kappa_1^{\text{ext}}}, \ldots, \sqrt{\kappa_n^{\text{ext}}})$ and finally the coupling matrix:-

$$\mathbf{M} = \begin{pmatrix} \tilde{\Delta}_1 & \beta_{12} & \cdots \\ \vdots & \ddots & \\ \beta_{m1}^* & & \tilde{\Delta}_m \end{pmatrix}.$$

The final matrix form of the EOMs becomes $\mathbf{KMKA} = i\mathbf{K}^{\text{ext}}\mathbf{A}_{\text{in}}$.

To solve for the scattering matrix, we use the input-output formalism to define the output mode operators as $\mathbf{A}_{\text{out}} = \mathbf{K}^{\text{ext}}\mathbf{A} - \mathbf{A}_{\text{in}}$. Finally, the steady-state scattering matrix is defined as

$$\mathbf{S} = \langle\mathbf{A}_{\text{out}}|\mathbf{A}_{\text{out}}\rangle \,/\, \left\langle\mathbf{A}_{\text{in}}^T\middle|\mathbf{A}_{\text{in}}^T\right\rangle = i\mathbf{H}\mathbf{M}^{-\mathbf{1}}\mathbf{H} - \mathbb{1} \tag{4.9}$$

where we have introduced $\mathbf{H} = \text{diag}(\sqrt{\eta_1}, \ldots, \sqrt{\eta_n})$.

4.3 Creating a 4-site BCL plaquette

We can create a programmable graph of connections between the modes, which then become the sites of our lattice arrayed in synthetic dimensions. As discussed in chapter 3, we induce parametric couplings between modes, including standard "hopping" by selecting a set of

modulation frequencies in resonance with the coupling terms. Because the couplings are created by coherent pump tones, we can control not only the magnitudes of the hopping terms, but also their relative phases. This phase control allows us to implement models with complex hopping terms, describing classical gauge fields and a variety of topological systems.

We program a four-site plaquette by pumping the SQUID with four coherent tones at the appropriate difference frequencies, ω^p_{nm}, as seen in Fig. 4.2. The choice of ω^p_{nm} determines which g_{nm} are nonzero, programming the connection graph of the lattice. The mode and pump frequencies are listed in Table 4.1, where we use the specific mode labels $n \in \{\text{a,b,c,d}\}$. We generate the pump tones using microwave generators phase-locked with 1 GHz references, which provides superior phase coherence.

In setting the coupling strengths for the lattice links, we normalize the coupling to the geometric mean of the mode linewidths κ_m and κ_n, defining $\beta_{nm} = g_{nm}/2\sqrt{\kappa_m \kappa_n}$. Here, we chose the β_{nm} to be roughly equal and in the strong-coupling limit. We use strong coupling here to mean that the eigenmodes of the system are resolved in frequency.

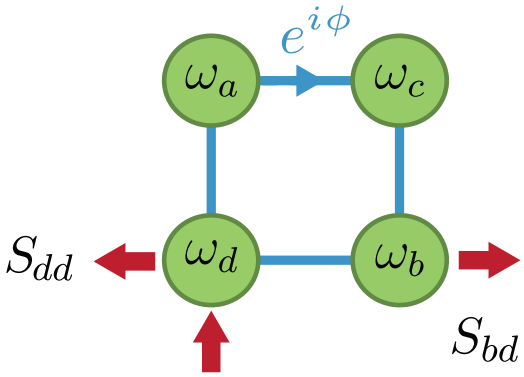

Figure 4.2: Synthetic lattice of a 4-site BCL. We program a four-site lattice in synthetic dimensions using four pump tones, which have a well-controlled phase. We measure the scattering matrix of the system by probing near each node frequency and measuring the output at various nodes, which are separated in frequency space. Reproduced from [27], with permission.

4.3.1 Characterization of the 4-site BCL plaquette

We use a vector network analyzer (VNA) to characterize the lattice to probe the system through its input capacitor as shown in Fig. 4.2. To measure the reflection coefficient, $S_{nn}(\Delta_n)$, of node n, we both probe and detect around that site's frequency, ω_n. When the lattice is activated, the single resonance observed at each uncoupled mode frequency is split into a number of resonances. We can interpret this set of resonances as the spectrum of the eigenmodes that exist on the lattice. Each element is centered on the uncoupled mode frequency and the frequency offset of the coupled eigenmodes can be viewed as the energy of the mode in the common rotating frame of the pumps. We can infer the mode coupling strengths, the g_{nm} of Eqn. 4.3, as a function of pump power from the set of spectra $\{S_{nn}\}$. For the simple case of two coupled modes, the frequency splitting of the eigenmodes directly gives the coupling strength. The situation is more complicated with more than two modes, but the basic intuition is similar.

Since our lattice sites exist along synthetic dimensions in frequency space, measuring the off-diagonal scattering coefficients S_{mn}, which characterize transport between sites, requires a frequency-conversion measurement, where the probe and detection frequencies are offset by ω^p_{nm}. We can distinguish S_{mn} and S_{nm} by swapping the probe and detection frequencies, allowing us to see nonreciprocal features in the transport.

4.4 Simulating the effect of a static gauge field on the BCL plaquatte

We simulate the effect of applying an external magnetic field to the lattice by making the $\{g_{nm}\}$ complex. The phase of the hopping term represents the phase acquired by an excitation moving along the link in the presence of the magnetic field. For our simple 4-site plaquette, only the total phase around the loop matters. As such, we choose, without loss of generality, to sweep the phase, ϕ, of the hopping term between sites a and c. Formally, moving the phases between links can be seen as a gauge transformation.

Figure 4.3 shows the measured 4x4 scattering matrix. Each element S_{nm} is measured as a function of ϕ and Δ_n. We clearly see nontrivial behavior as ϕ is varied, with a series of degeneracies arising and disappearing. The off-diagonal elements $\{S_{mn}\}$ show the magnitude of frequency-converting transport from site n to site m. The frequency differences are set by the pump frequencies, ω^p_{nm} (see Table 4.1). These transport measurements allow us to recover "spatial" information about the support of the eigenmodes over the synthetic lattice.

Being in the strong-coupling limit, we can excite a specific eigenmode at a well-defined detuning, Δ_n. As the eigenmodes are "spatially" distributed along the synthetic dimensions, the excitation hops between the sites and eventually leaks out of the cavity at another site, where it is then detected at the converted frequency.

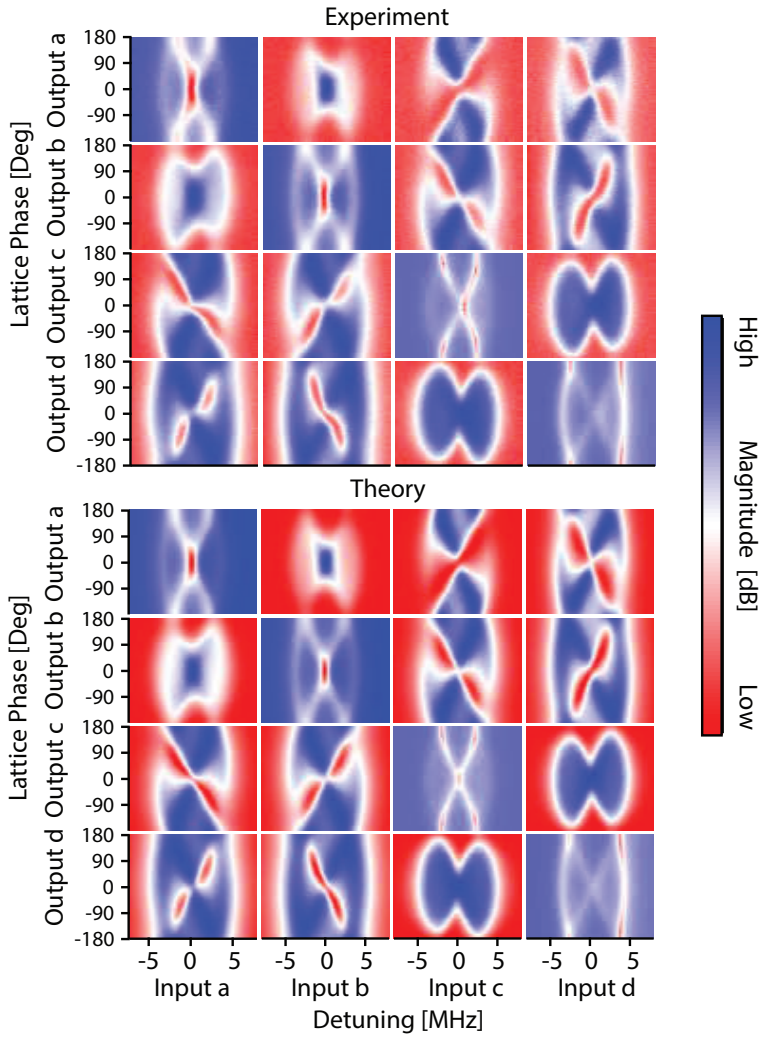

Figure 4.3: The scattering matrix of a 4-site BCL. The magnitude of the experimental (top) and theoretical (bottom) scattering matrices as a function of lattice phase, ϕ, and frequency. The frequency axes give the detunings, Δ_n, from the uncoupled mode frequencies. The diagonal reflection coefficients, $\{S_{nn}\}$, provide the spectrum of the lattice eigenmodes. The off-diagonal elements, $\{S_{mn}\}$, are the magnitude of frequency-converting transport between the nodes. The $\{S_{mn}\}$ allows us to characterize the "spatial" support of each eigenmode over the lattice in the synthetic dimensions (see text). We see clearly that the transport is nonreciprocal with $\{S_{mn}\}$ and $\{S_{nm}\}$ often being complements of each other. Reproduced from [27], with permission.

4.4.1 Measurement Fitting

After taking the scattering matrix measurements, we implement basic data preprocessing steps, described in more detail below. All steps described are applied to the data in linear amplitude units, converted from logarithmic units (dB) according to the relation $S_{nm,\mathrm{Lin}} = 10^{(S_{nm,\mathrm{Log}}/20)}$.

Both the reflection and frequency-converting transmission measurements are subject to frequency dependent gain and loss. Our first step in eliminating these effects is to measure and correct for the background, while all pumps are off. For the reflection measurements, we detune the cavity modes out of the VNA measurement bandwidth and measure the background reflection. We then divide the cavity's reflection data by the recorded background trace. The procedure for the transmission data is similar, except that we note that the background transmission measured is, in fact, the noise floor of the measurement system, as there is negligible frequency conversion of the probe signal if the pumps are not activated.

It is well-known that measurements of resonance curves in cryogenic environments often result in asymmetric line shapes [31]. This distortion of the ideally symmetric lineshapes can be caused by a number of effects, such small impedance mismatches in the measurement line that lead to interference between the desired signal and unintentionally scattered microwaves. A number of approaches to modelling these effects appear in the literature, but a simple and efficient one reduces the stray scattering to a complex loading of the resonator, producing a complex external loss rate, $\bar{\kappa}^{\mathrm{ext}}$ [31, 32]. The real part of $\bar{\kappa}^{\mathrm{ext}}$ is attributed to the ideal loading conditions whereas the imaginary part is responsible for asymmetries in the lineshape. In this sense, only the real part of $\bar{\kappa}^{\mathrm{ext}}$ contributes to the total quality factor. Accordingly, we will define $\kappa_n^{\mathrm{ext}} = \mathrm{Re}[\bar{\kappa}_n^{\mathrm{ext}}]$.

Following the above results, we define a complex external loss rate for each mode, $\bar{\kappa}_n^{\mathrm{ext}}$. In Eqn. 4.9 of the scattering matrix below, we use a complex coupling efficiency $\bar{\eta}_n = \bar{\kappa}_n^{\mathrm{ext}}/\kappa_n$, where the total loss rate is $\kappa_n = \mathrm{Re}[\bar{\kappa}_n^{\mathrm{ext}}] + \kappa_n^{\mathrm{int}}$. The reflection data is fit with this complex parameter $\bar{\eta}_n$ to account for the asymmetries we observe in the data. For the transport, the real part is used as we do not expect the same interference between probe and scattered signal because they are at different frequencies. In fact, using the complex $\bar{\eta}_n$ in the fits of the transport does not produce a noticeable change.

With the fine-scale frequency dependence now removed, we still need to account for the large-scale (between mode) frequency dependence of the loss and gain. We do this by introducing 12 scale parameters, C_{nm}, one for each of the transmission coefficients. (After the background subtraction, the diagonal $C_{nn} = 1$ by definition.)

Next, we incorporate the noise floor of the VNA in the transport measurement fitting by recognizing that the power of transported signal and the noise power add, giving

$$|S_{nm,\mathrm{fit}}| = \sqrt{(C_{nm}|S_{nm,\mathrm{Lin}}|)^2 + 1}, \tag{4.10}$$

recalling that the noise-floor power level has been normalized to one.

The pump tones acquire unknown phase shifts as they travel along the input lines. Since our current system has only one loop, all of these phase shifts add up to produce a constant offset in the loop phase, ϕ. Nevertheless, based on our understanding of the system and the observed periodicity, we can digitally offset the phase of the measured data. This offset phase, ϕ_{off}, becomes a fitting parameter. In the data displayed in Fig. 4.3 , the extracted ϕ_{off} has been subtracted.

The fitting was done on 2D data. The 1$^{\mathrm{st}}$ dimension is the frequency and the 2$^{\mathrm{nd}}$ is the loop phase, ϕ. We use four different values of ϕ: 0, $\pi/4$, $\pi/2$ and π. The phase differences between measurements are known since we control them with the microwave generators that produce the pump tones. Apart from the pump frequencies which are fixed, a total of 33 real parameters are adjusted for fitting: the lattice parameters ω_n, κ_n, $\bar{\eta}_n$, and β_{nm} as well as the ϕ_{off} and the 12 scaling factors C_{nm}. Here we define the normalized coupling strength $\beta_{nm} = g_{nm}/2\sqrt{\kappa_n\kappa_m}$. The full set of extracted parameters is listed in Tables I and II.

we focus on fitting the magnitude of the scattering elements and neglect the phases. We use a frequency-conversion circuit to measure the off-diagonal elements which makes the phases of transport ill-defined without additional calibration of the conversion circuit.

The magnitude of 64 traces that include the 16 scattering matrix elements at four loop phase values are fit simultaneously in one global fitting routine. Note that both the upper and lower part of the scattering matrix must be fit because the transmission is nonreciprocal. The low-level fitting routine is the builtin curve fitting operation of the "Igor Pro" software package.

We use the scattering matrix in Eqn. 4.9 formulated above to create the single output fitting function. The inputs of the fitting function are the probe frequency and the model parameters mentioned above. In addition, it also includes the predefined values of the pump tone frequencies and loop phases. Given those parameters, the function constructs the coupling matrix $\mathbf{M}$ and the coupling efficiency matrix $\mathbf{H}$ and then calculates the scattering matrix of the model for a defined frequency and loop phase. After that, the value of the desired scattering element, whose indices are passed as additional parameters, is extracted and rescaled based on Eqn. 4.10 before it is returned as the function output.

The global fitting procedure cascades the traces of the scattering elements at the designated loop phases to create a single trace to be fit. The global fitting function is then a piece-wise function that includes the local values for loop phase and the scattering element indices as inputs. The rest of the model parameters are global.

To generate initial guesses for the fitting routine, we perform a set of measurements on pairwise coupled modes, that is, with only one coupling pump on at a time. We fit simpler models of pairwise coupled modes to this set of data to extract initial estimates of ω_n, κ_n, η_n and β_{nm}. The initial guess for the phase of $\bar{\eta}_n$ is zero. The extracted parameters of these pairwise fits are shown in Table 4.1.

Mode	a	b	c	d
$\omega_n/2\pi$ [GHz]	4.1578	6.0979	7.4719	9.4802
$\kappa_n/2\pi$ [MHz]	1.0745	1.6298	2.8179	4.1049
η_n	0.46	0.62	0.86	0.74
Coupling	ac	ad	bc	bd
ω^p_{nm} [GHz]	3.3136	5.3223	1.3733	3.382
$g_{nm}/2\pi$ [MHz]	2.9795	3.1395	3.6815	4.6560
β_{nm}	0.8561	0.7474	0.8589	0.9000

Table 4.1: Extracted uncoupled and pairwise coupling parameters, used as initial guesses for the fitting routine for the full lattice. We see that there are small, ~ 1 MHz, frequency shifts between the pair-wise frequencies and the full lattice frequencies in Table 4.2. These are consistent with small, pump-induced shifts of the cavity frequency.

We do the global fitting in two steps. In the first step, we hold the parameters ω_n, κ_n and $\bar{\eta}_n$ constant at their initial values, and fit ϕ_{off} along with the β_n and C_{nm}. We perform the second and final step by freeing the remaining parameters including ω_n, κ_n and $\bar{\eta}_n$. We note that, comparing Table 4.2 and Table 4.1, there are small differences between the full-lattice parameters and the pairwise parameters. These small changes are consistent with what is expected due to the strong parametric pumping.

Mode	a	b	c	d
$\omega_n/2\pi$ [GHz]	4.1589	6.0992	7.4726	9.4806
σ [KHz]	2.4	3	3.7	5.3
$\kappa_n/2\pi$ [MHz]	1.0113	1.6494	2.9334	4.5804
σ [KHz]	5.7	10	7.4	15
$\lvert\bar{\eta}_n\rvert$	0.44	0.56	0.78	0.67
σ	15×10^{-3}	11×10^{-3}	11×10^{-3}	7×10^{-3}
Angle($\bar{\eta}_n$) [deg]	-16	2.1	-12.8	18
σ [deg]	1.02	0.74	0.34	0.33
Coupling	ac	ad	bc	bd
β_{nm}	0.8446	0.8612	0.7950	1.0278
σ	2.78×10^{-3}	2.23×10^{-3}	2.21×10^{-3}	3.2×10^{-3}

Table 4.2: The extracted BCL lattice parameters and their errors, σ.

Mode	a	b	c	d
a	–	19.55 ± 0.36	20.77 ± 0.42	19.83 ± 0.37
b	5.93 ± 0.11	–	9.31 ± 0.12	9.74 ± 0.1
c	8.64 ± 0.18	12.55 ± 0.16	–	13.52 ± 0.16
d	4.28 ± 0.08	6.74 ± 0.06	6.77 ± 0.08	–

Table 4.3: The extracted scaling parameters, C_{nm} and their errors.

The 64 VNA traces used, along with the resulting fits, are shown in the figures below. Each trace contains four resonance peaks, some of them overlapping, resulting in a total of 256 peaks being fit simultaneously using just 33 parameters, or about 1/8 of a parameter per peak. This can be compared to doing detailed fitting of a single resonance where often five or more parameters are used to fit one peak. With that in mind, we would say that the quality of the fit is remarkable given the complexity of the data.

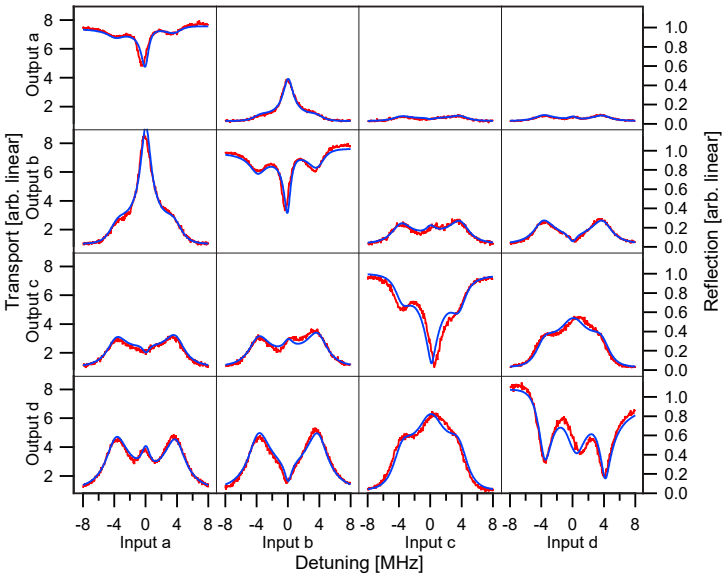

Figure 4.4: Fit results at $\phi = 0$, showing the measured scattering matrix (red lines) and the fits (blue lines). Reproduced from [27], with permission.

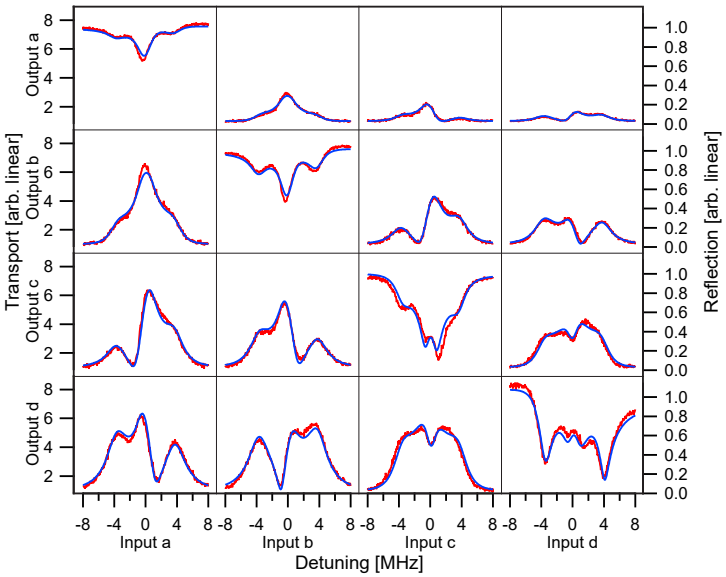

Figure 4.5: Fit results at $\phi = \pi/4$, showing the measured scattering matrix (red lines) and the fits (blue lines). Reproduced from [27], with permission.

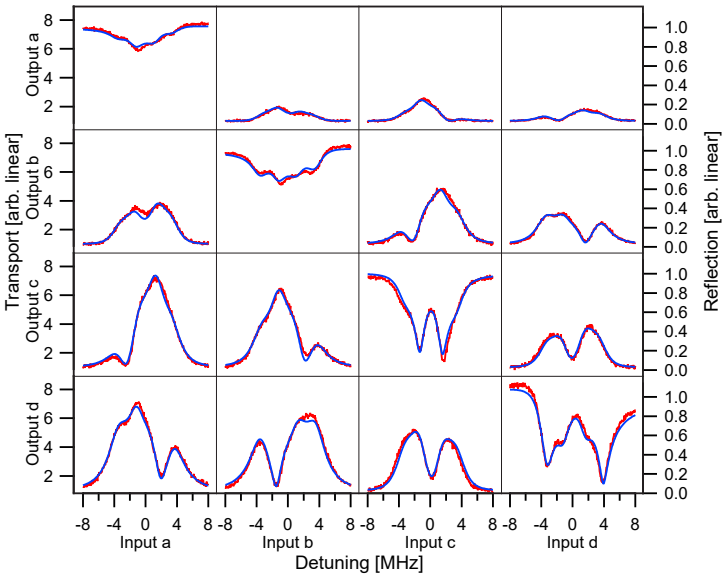

Figure 4.6: Fit results at $\phi = \pi/2$, showing the measured scattering matrix (red lines) and the fits (blue lines). Reproduced from [27], with permission.

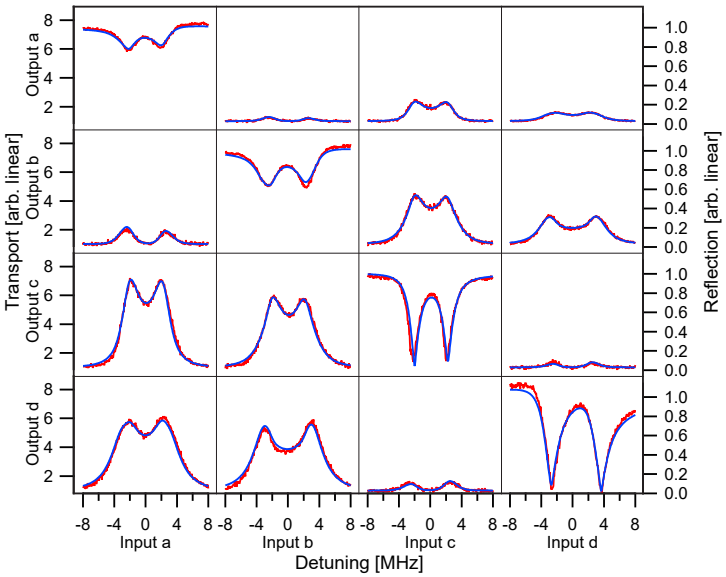

Figure 4.7: Fit results at $\phi = \pi$, showing the measured scattering matrix (red lines) and the fits (blue lines). Reproduced from [27], with permission.

4.5 Observations

We observe a number of interesting features in the scattering matrix. First, we observe clear nonreciprocity in the transport, for instance, noticing that S_{bc} and S_{cb} are effectively complements of each other. The definition of reciprocity is that $S_{ij} = S_{ji}$, which is clearly broken here. We will not emphasize it here, but this can be connected to the fictitious magnetic flux breaking time-reversal symmetry.

We also identify interesting eigenmodes that we associate with emerging topological features of the Creutz ladder. At $\phi = \pi$, Creutz predicted that the bulk states collapse in a pair of flat bands at equal but opposite energies. A flat band implies that the bulk states are localized, as the group velocity goes to zero. Creutz referred to the associated states as "solitons" and identified the localization as arising from interference between alternate paths on the lattice (see Fig. 4.8(d)), a phenomenon often referred to as Aharonov-Bohm caging in recent literature. With open boundary conditions, Creutz also predicted the existence of a pair of zero-energy states localized to the ends of the ladder. The connection between the observed eigenmodes and these topological states is discussed in detail in Fig. 4.8.

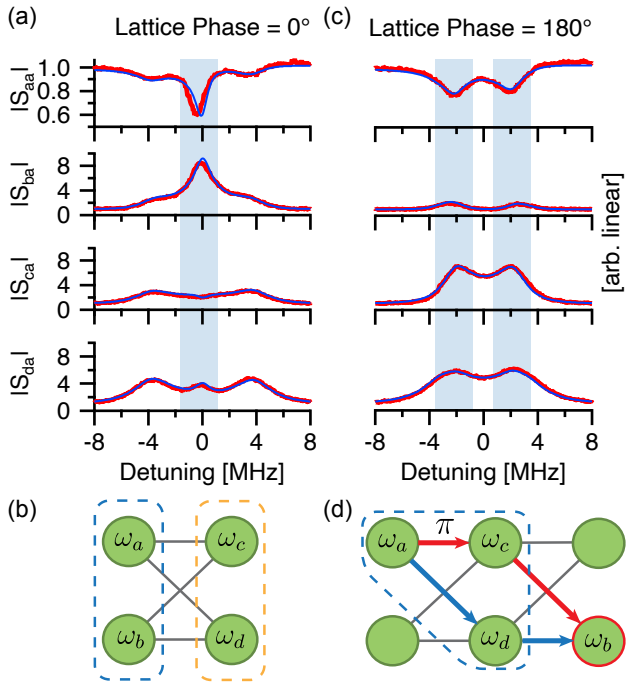

Figure 4.8: Topological precursors. (a) $\phi = 0$ line cuts of the measured (red) and theory (blue) scattering parameters in Fig. 4.3 when probing at node a. The vertical axes are normalized to the background. The measurements indicate the existence of an eigenmode at zero energy with significant support only in nodes a and b, which are not directly connected. We infer this from the relatively high transmission amplitude from a to b. We also observe a 2^{nd} zero mode localized on sites c and d. (b) Twisted plaquette. We expect topological features of the Creutz ladder to appear at $\phi = \pi$ and not $\phi = 0$. However, we note that if we twist the plaquette as indicated, $\phi = 0$ regardless of the external flux. After twisting, the zero modes now appear at the two ends of the plaquette. These states are reminiscent of the predicted zero-mode end states [23]. (c) $\phi = \pi$ line cuts when probing from node a. The scales of the vertical axes are the same as panel (a). The measurements indicate the existence of two pairs of degenerate eigenmodes, one at positive and one at negative detuning, that have support on all but one of the nodes. One of these four eigenmodes exists on each corner. (d) Caging. We can associate the corner eigenmodes with the soliton states in the Creutz ladder by identifying the lattice as the indicated trapezoidal path. Due to Aharonov-Bohm caging, an excitation at, *e.g.*, node a cannot propagate to node b. Reproduced from [27], with permission.

4.6 Discussion

Previously, we have demonstrated the feasibility of our AQS platform based on a multimode superconducting parametric cavity by simulating a plaquette of the bosonic Creutz ladder [27]. The cavity modes share a superconducting quantum interference device (SQUID) which acts as a common boundary condition. Parametric modulation of the boundary condition induces complex "hopping" couplings that allow us to create a programmable graph of connected (coupled) modes, realizing a lattice in synthetic dimensions. We characterize the lattice with scattering measurements, reconstructing the experimental Hamiltonian, and observing important precursors of topological features. By controlling the phases of the complex hopping terms, we implemented static gauge fields and topological effects including nonreciprical transport and Aharonov-Bohm caging. This platform can be easily extended to larger lattices and different models involving other interactions.

Chapter 5

Bosonic Kitaev Chain Experiment

5.1 Introduction

The mode-to-mode coupling demonstrated in the previous chapter can be extended in a number of promising and interesting ways. In the BCL model, we only activated the simplest type of coupling (hopping). Another well-characterized parametric process is two-photon parametric downconversion which leads to a type of pairing interaction, as we defined it in chapter 3. This process is activated by pumping at the sum of two mode frequencies, adding Hamiltonian terms of the form $\hat{a}_i^\dagger \hat{a}_j^\dagger$. First, this term is interesting as it is a source of nonclassical states, including squeezed and entangled states [22]. Next, downconversion unlocks a number of interesting simulation effects. Combining both hopping and pairing terms could help in simulating effects such as superconductivity [33], and also leads directly to chiral and topological features, as in the bosonic Kitaev-Majorona chain [33]. Finally, downconversion provides access to coherent non-Hermitian Hamiltonians, in contrast to the loss-induced non-Hermiticity widely studied in the literature [34, 35].

As a demonstration of the pairing interaction in our platform, we follow the theory of McDonald *et al.* [33] to construct and simulate chiral effects in a 3-site bosonic Kitaev chain. We observe two striking properties of the bosonic Kitaev chain: chiral transport and spectral sensitivity to boundary conditions. To validate our experiment, we use the theory to reconstruct the Hamiltonian by fitting the experimental results to the Kitaev model.

This chapter is largely adapted from our paper [36]. The contributions of the authors are as follows.

- The theory collaborators, comprised of A. McDonald and A.A. Clerk, proposed the

bosonic Kitaev chain model and formulated the framework for using the device to simulate the model.

- I have conducted the experiments and collected data. Jimmy S.C. Hung helped conduct experiments and collect data in the early stages of the work.
- Z. Shi took the lead in fitting the data to the theory and reconstructing the model's Hamiltonian.
- We used two devices in this experiment. C.W. Sandbo Chang designed the first device and, with assistance from I. Nsanzineza, fabricated it. D. Dubyna designed the second device and, with assistance from I. Nsanzineza, fabricated it.
- While Z. Shi and I, along with Jimmy S.C. Hung in the early stages, took the lead in interpreting the results, the theory collaborators also contributed to the interpretation and provided valuable insights.
- Z. Shi and I were jointly responsible for writing the majority of the manuscript. The theory collaborators also participated in reviewing and editing the manuscript.

5.2 Kitaev Chain Theory

5.2.1 The Bosonic Kitaev Chain

The Kitaev-Majorona chain is a famous topological model originally proposed as spinless fermions residing on a 1D tight-binding lattice, with both hopping and pairing terms between nearest-neighbor sites [37]. The model hosts a topologically nontrivial phase with two unpaired Majorana modes at the ends of the chain, which form a single delocalized and topologically protected fermionic mode. It is likewise possible to construct a topologically nontrivial Kitaev chain model of bosons [33, 38], even though it does not host topologically protected edge modes as the fermionic Kitaev chain does.

Consider the bosonic 1D tight-binding Hamiltonian ($\hbar = 1$)

$$\hat{\mathcal{H}}_B = \frac{1}{2}\sum_j \left(it\hat{a}^\dagger_{j+1}\hat{a}_j + i\Delta\hat{a}^\dagger_{j+1}\hat{a}^\dagger_j + \text{h.c.}\right) \tag{5.1}$$

illustrated in Fig. 5.1(a). Here $\hat{a}_j$ is a bosonic annihilation operator on site j, and for simplicity we have assumed that the hopping strength it and the pairing strength $i\Delta$

are purely imaginary with $t > \Delta > 0$ positive real constants. (In a large portion of the parameter space, the system can be reduced to this special case via a Bogoliubov transformation.) Following the fermionic example, McDonald *et al.* split each boson into two normal Hermitian field quadratures, $\hat{x}_j = (\hat{a}_j^\dagger + \hat{a}_j)/\sqrt{2}$ and $\hat{p}_j = i(\hat{a}_j^\dagger - \hat{a}_j)/\sqrt{2}$. Now the Hamiltonian consists entirely of the products of adjacent $\hat{x}$ and $\hat{p}$ quadratures,

$$\hat{\mathcal{H}}_B = \frac{1}{2}\sum_j \left[(t+\Delta)\,\hat{p}_{j+1}\hat{x}_j - (t-\Delta)\,\hat{x}_{j+1}\hat{p}_j\right], \tag{5.2}$$

such that the Heisenberg equations of motion for $\hat{x}$ and $\hat{p}$ quadratures are independent of each other:

$$\begin{aligned}\dot{\hat{x}}_j &= \frac{1}{2}(t+\Delta)\hat{x}_{j-1} - \frac{1}{2}(t-\Delta)\hat{x}_{j+1},\\ \dot{\hat{p}}_j &= \frac{1}{2}(t-\Delta)\hat{p}_{j-1} - \frac{1}{2}(t+\Delta)\hat{p}_{j+1}.\end{aligned} \tag{5.3}$$

When Δ is nonzero, the couplings are asymmetric between left and right, giving rise to phase-dependent chiral propagation. In particular, the propagation becomes fully chiral as Δ approaches t, with the x quadrature propagating to the right and the p quadrature to the left.

While Eq. (5.1) is Hermitian, we can effectively view Eq. (5.3) as two decoupled bosonic Hatano-Nelson chains with asymmetric hopping strengths [39]; this is an example of effective non-Hermitian dynamics occurring in Hermitian systems [40, 38]. The spectra of non-Hermitian systems can depend drastically on their boundary conditions, a phenomenon known as the non-Hermitian skin effect [41]. Indeed, all energy eigenvalues of Eq. (5.1) are real under open boundary conditions as long as $\Delta < t$, but become complex for any nonzero Δ under periodic boundary conditions [33]. In other words, the bosonic Kitaev chain Eq. (5.1) is dynamically stable in the presence of edges for $\Delta < t$, and unstable in the absence of edges for any nonzero Δ.

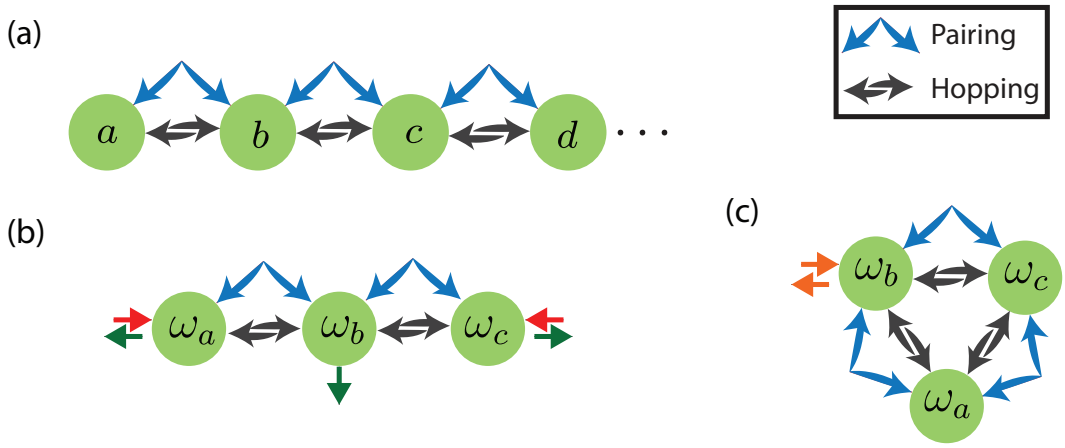

Figure 5.1: (a) Schematic representation of the bosonic Kitaev chain. Black and blue arrows indicate the hopping and pairing couplings, respectively. (b) Device cartoon. We create parametric interactions between cavity modes by pumping the SQUID through a flux line. Blue and black signals represent the two pumps creating hopping and pairing couplings for each link. The system is probed through the input capacitor by a coherent tone. (c)–(d) Synthetic Kitaev lattices. We program 3-site Kitaev chains in synthetic dimensions with (c) open and (d) periodic boundary conditions, using four and six pump tones, respectively. We characterize the open chain (c) by sending a coherent signal with a constant amplitude and a phase varying from $-180°$ to $180°$, while probing at various site frequencies to measure signal transport. In the closed chain (d), we focus on the chain spectrum by measuring the reflection coefficient around the frequency of each site.

5.3 Programming the Hamiltonian in our AQS

5.3.1 Generic Hamiltonian

The general quadratic Hamiltonian that can be programmed in our AQS takes the following form:

$$\hat{\mathcal{H}}_S = \sum_j \delta\omega_j \hat{a}_j^\dagger \hat{a}_j + \frac{1}{2}\sum_{\langle jj'\rangle} \Big(t_{jj'} e^{i\varphi^t_{jj'}} \hat{a}_j^\dagger \hat{a}_{j'} + \Delta_{jj'} e^{i\varphi^\Delta_{jj'}} \hat{a}_j \hat{a}_{j'} + \text{h.c.} \Big), \tag{5.4}$$

where we have already adopted the rotating-wave approximation and work in the frame rotating at the frequency ω_j at mode j (which is defined below in relation to the frequencies of the parametric pumps). Here the detuning $\delta\omega_j = \omega_j - \omega_j^{(0)}$, with $\omega_j^{(0)}$ the uncoupled frequency of mode j. The second sum runs over all pairs of sites j and j' we intend to connect; the hopping $t_{jj'}$ and the pairing $\Delta_{jj'}$ are respectively activated by parametric pumps at the frequencies $|\omega_j - \omega_{j'}|$ and $\omega_j + \omega_{j'}$, and have tunable phases $\varphi^t_{jj'} = -\varphi^t_{j'j}$ and $\varphi^\Delta_{jj'} = \varphi^\Delta_{j'j}$.

5.3.2 Gauge invariance in Kitaev chain with arbitrary phases

Under the local gauge transformation $\hat{a}_j \to \hat{a}_j e^{i\theta_j}$, which transforms the quadratures $\hat{x}$ and $\hat{p}$ into generalized quadratures $\hat{x}_\theta$ and $\hat{p}_\theta$, the coupling phases associated with the link between j and j' transform as $\varphi^t_{jj'} \to \varphi^t_{jj'} + \theta_j - \theta_{j'}$ and $\varphi^\Delta_{jj'} \to \varphi^\Delta_{jj'} - \theta_j - \theta_{j'}$. Defining the link phases $\varphi^\pm_{jj'} \equiv (\varphi^t_{jj'} \pm \varphi^\Delta_{jj'})/2 = -\varphi^\mp_{j'j}$, we find $\varphi^+_{jj'} \to \varphi^+_{jj'} - \theta_{j'}$ and $\varphi^-_{jj'} \to \varphi^-_{jj'} + \theta_j$ are independent of θ_j and $\theta_{j'}$ respectively. For two links $j_1 j_2$ and $j_2 j_3$ sharing the site j_2, the linear combination $\varphi^+_{j_1 j_2} + \varphi^-_{j_2 j_3}$ is fully gauge-invariant.

For a translationally invariant Kitaev chain with arbitrary link phases, Eq. (5.4) becomes

$$\begin{aligned}\hat{\mathcal{H}}_{B,g} &= \sum_j \Big[\delta\omega \hat{a}_j^\dagger \hat{a}_j + \frac{1}{2}\Big(t e^{i\varphi_t} \hat{a}_j^\dagger \hat{a}_{j+1} + \Delta e^{i\varphi_\Delta} \hat{a}_j \hat{a}_{j+1} + \text{h.c.} \Big) \Big] \\ &= \sum_{k>0} \Big(a_k^\dagger, a_{-k} \Big) \left(h_0 \breve{1} + \mathbf{h}\cdot\breve{\sigma} \right) \begin{pmatrix} a_k \\ a_{-k}^\dagger \end{pmatrix}, \end{aligned} \tag{5.5}$$

where, going into momentum space, we have assumed periodic boundary conditions. Operators in the particle-hole space are marked with a breve, and their coefficients are

$$h_0(k) = \delta\omega + t\cos\varphi_t \cos k, \tag{5.6}$$

and

$$\mathbf{h}(k) = \Big(\Delta\cos\varphi_\Delta \cos k, \Delta\sin\varphi_\Delta\cos k, \\ t\sin\varphi_t \sin k\Big). \tag{5.7}$$

For a hypothetical fermionic Hamiltonian of the form Eq. (5.5), the spectrum would be given by $E_{\mathrm{F}} = h_0 \pm |\mathbf{h}|$ with the gap closing at $\mathbf{h} = 0$, and the momentum space winding number would depend on whether the trajectory of $\mathbf{h}$ encloses the origin. However, this is not the case for the bosonic Hamiltonian Eq. (5.5); owing to its effectively non-Hermitian dynamics, its topology is characterized directly by the complex energy spectrum [35], found as the eigenvalues of the dynamical matrix $\left(h_0\breve{1} + \mathbf{h}\cdot\breve{\sigma}\right)\breve{\sigma}_z$, i.e.

$$E_{\mathrm{B}}(k) = t\sin k\sin\varphi_t \\ \pm\sqrt{\left(\delta\omega + t\cos k\cos\varphi_t\right)^2 - \Delta^2\cos^2 k}. \tag{5.8}$$

Note that E_{B} depends on the gauge-invariant phase $\varphi_t = \varphi^+_{j-1,j} + \varphi^-_{j,j+1}$, but not on φ_Δ which can be shifted by a uniform gauge transformation $\hat{a}_j \to \hat{a}_j e^{i\theta}$. In particular, in the special case $\delta\omega = 0$, we find E_{B} becomes complex and the periodic chain becomes dynamically unstable if $|t\cos\varphi_t| < \Delta$, in agreement with [33]. Again, the system is always dynamically unstable under periodic boundary conditions if $\varphi_t = \pi/2$ and $\Delta > 0$. Meanwhile, if $t > \Delta$, it is possible to change the stability of the periodic system by tuning φ_t between 0 and $\pi/2$.

Returning to Eq. (5.4), we probe the system by coupling it to a measurement line, described by the Hamiltonian

$$\hat{\mathcal{H}}_P = i\sum_j \sqrt{\kappa_j^{\mathrm{ext}}}\left(\hat{a}^\dagger_{\mathrm{in},j} - \hat{a}_{\mathrm{in},j}\right)\left(\hat{a}^\dagger_j + \hat{a}_j\right). \tag{5.9}$$

Here κ_j^{ext} is the external coupling rate to the input mode $\hat{a}_{\mathrm{in},j}$. Taking internal dissipation into account, the transport properties of the system then follow from the Heisenberg-

Langevin equations of motion

$$\begin{aligned}
\dot{\hat{a}}_j^{\mathrm{S}} &= i\left(\delta\omega_j^{\mathrm{S}} + i\frac{\kappa_j}{2}\right)\hat{a}_j^{\mathrm{S}} + \frac{i}{2}\sum_{j'}\Big(t_{jj'}e^{i\varphi^t_{jj'}}\hat{a}_{j'}^{\mathrm{S}} \\
&\quad + \Delta_{jj'}e^{-i\varphi^{\Delta}_{jj'}}\hat{a}_{j'}^{\mathrm{I}\dagger}\Big) + \sqrt{\kappa_j^{\mathrm{ext}}}\hat{a}_{\mathrm{in},j}^{\mathrm{S}}, \\
\dot{\hat{a}}_j^{\mathrm{I}\dagger} &= -i\left(\delta\omega_j^{\mathrm{I}} - i\frac{\kappa_j}{2}\right)\hat{a}_j^{\mathrm{I}\dagger} - \frac{i}{2}\sum_{j'}\Big(t_{jj'}e^{-i\varphi^t_{jj'}}\hat{a}_{j'}^{\mathrm{I}\dagger} \\
&\quad + \Delta_{jj'}e^{i\varphi^{\Delta}_{jj'}}\hat{a}_{j'}^{\mathrm{S}}\Big) + \sqrt{\kappa_j^{\mathrm{ext}}}\hat{a}_{\mathrm{in},j}^{\mathrm{I}\dagger},
\end{aligned} \tag{5.10}$$

where the "signal" frequency component $\hat{a}_j^{\mathrm{S}}$ is coupled to the "idler" frequency component $\hat{a}_{j'}^{\mathrm{I}}$ by the pairing pump $\Delta_{jj'}$; the frequencies of both $\hat{a}_j^{\mathrm{S}}$ and $\hat{a}_j^{\mathrm{I}}$ have are close to $\omega_j^{(0)}$, with the probe detuning defined as $\delta\omega_j^{\mathrm{S,I}} = \omega_j^{\mathrm{S,I}} - \omega_j^{(0)}$. κ_j is the total single-photon loss rate including both internal and external contributions. For steady-state solutions, we can let the time derivatives vanish and substitute the solutions into the input-output relation $\hat{a}_{\mathrm{out},j}^{\mathrm{S,I}} = \sqrt{\kappa_j^{\mathrm{ext}}}\hat{a}_j^{\mathrm{S,I}} - \hat{a}_{\mathrm{in},j}^{\mathrm{S,I}}$ to obtain the transport properties.

5.3.3 Transport in an open 3-mode system

For simplicity, we present the analytical results at zero probe detuning $\delta\omega = 0$ from the beginning. we express the output fields in terms of a scattering matrix

$$\begin{pmatrix}
\langle\hat{a}_{o,a}^{S}\rangle \\ \langle\hat{a}_{o,a}^{I\dagger}\rangle \\ \langle\hat{a}_{o,b}^{S}\rangle \\ \langle\hat{a}_{o,b}^{I\dagger}\rangle \\ \langle\hat{a}_{o,c}^{S}\rangle \\ \langle\hat{a}_{o,c}^{I\dagger}\rangle
\end{pmatrix} =
\begin{pmatrix}
S_{aa}^{SS} & S_{aa}^{SI} & S_{ab}^{SS} & S_{ab}^{SI} & S_{ac}^{SS} & S_{ac}^{SI} \\
S_{aa}^{IS} & S_{aa}^{II} & S_{ab}^{IS} & S_{ab}^{II} & S_{ac}^{IS} & S_{ac}^{II} \\
S_{ba}^{SS} & S_{ba}^{SI} & S_{bb}^{SS} & S_{bb}^{SI} & S_{bc}^{SS} & S_{bc}^{SI} \\
S_{ba}^{IS} & S_{ba}^{II} & S_{bb}^{IS} & S_{bb}^{II} & S_{bc}^{IS} & S_{bc}^{II} \\
S_{ca}^{SS} & S_{ca}^{SI} & S_{cb}^{SS} & S_{cb}^{SI} & S_{cc}^{SS} & S_{cc}^{SI} \\
S_{ca}^{IS} & S_{ca}^{II} & S_{cb}^{IS} & S_{cb}^{II} & S_{cc}^{IS} & S_{cc}^{II}
\end{pmatrix}
\begin{pmatrix}
\langle\hat{a}_{i,a}^{S}\rangle \\ \langle\hat{a}_{i,a}^{I\dagger}\rangle \\ \langle\hat{a}_{i,b}^{S}\rangle \\ \langle\hat{a}_{i,b}^{I\dagger}\rangle \\ \langle\hat{a}_{i,c}^{S}\rangle \\ \langle\hat{a}_{i,c}^{I\dagger}\rangle
\end{pmatrix} \tag{5.11}$$

where, defining a common denominator

$$D^o = \left(t_{ab}^2 - \Delta_{ab}^2\right)\kappa_c + \left(t_{bc}^2 - \Delta_{bc}^2\right)\kappa_a + \kappa_a\kappa_b\kappa_c, \tag{5.12}$$

We move on to investigate the different matrix elements.

Transport from the center mode to the ends

We can write the relevant scattering matrix elements from central mode b to end mode a as

$$\begin{aligned} S_{ab}^{SS} &= S_{ab}^{II*} = \frac{2i}{D^o}\sqrt{\kappa_a^{\text{ext}}\kappa_b^{\text{ext}}}\kappa_c\, t_{ab}\, e^{i\left(\varphi_{ab}^{+}+\varphi_{ab}^{-}\right)}, \\ S_{ab}^{SI} &= S_{ab}^{IS*} = \frac{2i}{D^o}\sqrt{\kappa_a^{\text{ext}}\kappa_b^{\text{ext}}}\kappa_c\, \Delta_{ab}\, e^{i\left(-\varphi_{ab}^{+}+\varphi_{ab}^{-}\right)}, \end{aligned} \tag{5.13}$$

where we used link phase definitions $\varphi_{jj'}^{\pm} \equiv (\varphi_{jj'}^{t} \pm \varphi_{jj'}^{\Delta})/2$. The matrix elements for transport in the opposite directions, $\{S_{ba}^{SS}, S_{ba}^{II}, S_{ba}^{SI}, S_{ba}^{IS}\}$, are obtained by interchanging modes $a \leftrightarrow b$ and, by extension, $\varphi_{ab}^{+} \leftrightarrow -\varphi_{ab}^{-}$. (Note that $\varphi_{ab}^{t} = -\varphi_{ba}^{t}$, $\varphi_{ab}^{\Delta} = \varphi_{ba}^{\Delta}$, so when interchanging modes, we have $\varphi_{ba}^{+} = -\varphi_{ab}^{-}$.). Furthermore, we can also obtain similar expressions for transport from central mode b to the other end at mode c, $\{S_{bc}^{SS}, S_{bc}^{II}, S_{bc}^{SI}, S_{bc}^{IS}\}$, by interchanging $a \leftrightarrow c$.

To illustrate the possibility of phase-dependent chiral transport in an interesting case, we consider a coherent tone input $\left\langle \hat{a}_{i,b}^{S/I} \right\rangle = |\langle \hat{a}_{i,b} \rangle|\, e^{i\varphi_{i,b}}$ in the central mode b and probes at a and c. It is straightforward to find the angular dependence of the complex transported amplitudes from b to a and from b to c:

$$\begin{aligned} S_{ab}^{SS}\left\langle \hat{a}_{i,b}^{S} \right\rangle + S_{ab}^{SI}\left\langle \hat{a}_{i,b}^{I\dagger} \right\rangle &\propto ie^{i\varphi_{ab}^{-}}\left[t_{ab}\, e^{i\left(\varphi_{i,b}+\varphi_{ab}^{+}\right)} + \Delta_{ab}\, e^{-i\left(\varphi_{i,b}+\varphi_{ab}^{+}\right)}\right], \\ S_{cb}^{SS}\left\langle \hat{a}_{i,b}^{S} \right\rangle + S_{cb}^{SI}\left\langle \hat{a}_{i,b}^{I\dagger} \right\rangle &\propto ie^{-i\varphi_{ba}^{+}}\left[t_{bc}\, e^{i\left(\varphi_{i,b}-\varphi_{bc}^{-}\right)} + \Delta_{bc}\, e^{-i\left(\varphi_{i,b}-\varphi_{bc}^{-}\right)}\right]. \end{aligned} \tag{5.14}$$

The input phase $\varphi_{i,b} = -\varphi_{ab}^{+}$ is favored in transport from b to a, and by analogy $\varphi_{i,b} = \varphi_{bc}^{-}$ is favored in transport from b to c. This gives us the freedom to choose whether the same or the orthogonal phases are favored in transport to the chain's ends. In the trivial case, we consider the same quadrature being transported to the ends; when $\varphi_{i,b} = -\varphi_{ab}^{+}$ and $\varphi_{i,b} = \varphi_{bc}^{-}$ correspond to the same phase, i.e. when $\varphi_{ab}^{+} + \varphi_{bc}^{-} = 0$. On the other hand, it is now clear that we can achieve a strongly chiral case when $\varphi_{i,b} = -\varphi_{ab}^{+}$ and $\varphi_{i,b} = \varphi_{bc}^{-}$ correspond to orthogonal quadratures being transported to opposite directions, i.e. when $\varphi_{ab}^{+} + \varphi_{bc}^{-} = \pi/2 + n\pi$.

It is useful to define the transmission coefficient $\Gamma_{ab} = S_{ab}^{SS} + S_{ab}^{SI}$. Assuming equal link coupling strengths, the magnitudes of the transmission in the enhanced and suppressed input phases reads,

$$\left|\Gamma_{ab}^{\pm}\right| = \kappa^{\text{ext}}\frac{(t \pm \Delta)}{\left(t^2 - \Delta^2 + \frac{\kappa^2}{2}\right)} \tag{5.15}$$

Then, we can calculate the contrast between the amplitudes of the enhanced and suppressed phases.

$$\text{contrast}_{ab} = \frac{\left|\Gamma_{ab}^{+}\right| - \left|\Gamma_{ab}^{-}\right|}{\left|\Gamma_{ab}^{+}\right| + \left|\Gamma_{ab}^{-}\right|} = \frac{\Delta}{t} \tag{5.16}$$

The contrast then gives a direct measure of the pairing strength with respect to the hopping strength, which we use later in the calibration process.

Investigating the chirality of the chain of transport between the ends

A particularly interesting case is to investigate the transport properties of the signal propagating along the chain. Let us consider a coherent tone input $\left\langle \hat{a}_{i,a}^{S/I} \right\rangle = \left|\langle \hat{a}_{i,a} \rangle\right| e^{i\varphi_{i,a}}$ in mode a and probe mode c. The relevant scattering matrix elements are

$$\begin{aligned} S_{ca}^{SS} = S_{ca}^{II*} &= \frac{2}{D^o}\sqrt{\kappa_a^{\text{ext}}\kappa_c^{\text{ext}}}\left(-t_{ab}\,t_{bc}\,e^{-i\left(\varphi_{ab}^{+}+\varphi_{bc}^{-}\right)} + \Delta_{ab}\,\Delta_{bc}\,e^{i\left(\varphi_{ab}^{+}+\varphi_{bc}^{-}\right)}\right)e^{-i\left(\varphi_{ab}^{-}+\varphi_{bc}^{+}\right)}, \\ S_{ca}^{SI} = S_{ca}^{IS*} &= \frac{2}{D^o}\sqrt{\kappa_a^{\text{ext}}\kappa_c^{\text{ext}}}\left(-\Delta_{ab}\,t_{bc}\,e^{-i\left(\varphi_{ab}^{+}+\varphi_{bc}^{-}\right)} + t_{ab}\,\Delta_{bc}\,e^{i\left(\varphi_{ab}^{+}+\varphi_{bc}^{-}\right)}\right)e^{i\left(\varphi_{ab}^{-}-\varphi_{bc}^{+}\right)}. \end{aligned} \tag{5.17}$$

Extracting the angular dependence of the transport and omitting irrelevant constants:

$$\begin{aligned} &S_{ca}^{SS}\left\langle \hat{a}_{i,a}^{S} \right\rangle + S_{ca}^{SI}\left\langle \hat{a}_{i,a}^{I\dagger} \right\rangle \\ \propto &e^{-i\varphi_{bc}^{+}}\left[\left(-t_{ab}\,t_{bc}\,e^{-i\left(\varphi_{ab}^{+}+\varphi_{bc}^{-}\right)} + \Delta_{ab}\,\Delta_{bc}\,e^{i\left(\varphi_{ab}^{+}+\varphi_{bc}^{-}\right)}\right)e^{i\left(\varphi_{i,a}-\varphi_{ab}^{-}\right)}\right. \\ &\left. + \left(-\Delta_{ab}\,t_{bc}\,e^{-i\left(\varphi_{ab}^{+}+\varphi_{bc}^{-}\right)} + t_{ab}\,\Delta_{bc}\,e^{i\left(\varphi_{ab}^{+}+\varphi_{bc}^{-}\right)}\right)e^{-i\left(\varphi_{i,a}-\varphi_{ab}^{-}\right)}\right]. \end{aligned} \tag{5.18}$$

When the sum phases satisfy $\varphi_{ab}^{+} + \varphi_{bc}^{-} = n\pi$, the input phases $\varphi_{i,a} = \varphi_{ab}^{-}$ and $\varphi_{i,a} = \varphi_{ab}^{-} + \pi/2$ correspond to transported amplitudes proportional to $(t_{ab} \pm \Delta_{ab})\,(t_{bc} \mp \Delta_{bc})$ respectively. Assuming equal link coupling strengths, we reach trivial dynamics as the transport amplitudes become completely phase-independent $(t+\Delta)\,(t-\Delta)$, consistent with the trivial case mentioned in the previous section:

$$\begin{aligned} |\Gamma_{ca}| &= \frac{2\kappa^{\text{ext}}}{2\kappa\left(t^2 - \Delta^2 + \frac{\kappa^2}{2}\right)}\left(t^2 - \Delta^2\right), \\ &= \eta\frac{(t^2 - \Delta^2)}{\left(t^2 - \Delta^2 + \frac{\kappa^2}{2}\right)} \end{aligned} \tag{5.19}$$

The transmission coefficient is independent of the input phase and equivalent to a hopping-only lattice with an effective coupling strength of $g^2 = t^2 - \Delta^2$.

On the other hand, if we align the sum phases such that $\varphi_{ba}^{+} + \varphi_{bc}^{-} = \pi/2 + n\pi$ (i.e. when input in mode a experiences chiral transport), the input phases $\varphi_{i,a} = \varphi_{ab}^{-}$ and $\varphi_{i,a} = \varphi_{ab}^{-} + \pi/2$ correspond to transported amplitudes proportional to $(g_{12}^{t} \pm g_{12}^{\Delta})(g_{13}^{t} \pm g_{13}^{\Delta})$ respectively. Again, we equal link couplings; the transmission coefficients are, respectively,

$$\left|\Gamma_{ca}^{\pm}\right| = \eta \frac{(t \pm \Delta)^2}{\left(t^2 - \Delta^2 + \frac{\kappa^2}{2}\right)} \tag{5.20}$$

Then we can estimate the amount of phase-dependent enhancement and suppression of transport compared to the trivial case:

$$\begin{aligned} \text{enhancement} &= \frac{(t+\Delta)}{(t-\Delta)}, \\ \text{suppression} &= \frac{(t-\Delta)}{(t+\Delta)}. \end{aligned} \tag{5.21}$$

We expect to see a substantial difference between the transported signal in the trivial case and enhanced and suppressed signals in the chiral case. Therefore, with $\varphi_{ab}^{+} + \varphi_{bc}^{-} = n\pi + \pi/2$, the transport depends more strongly on the input phase. The transport between a and c exhibits chirality in the same regime: the input phase $\varphi_{i,a} = \varphi_{ab}^{-}$ corresponding to enhanced transport from a to c yields an output phase $-\varphi_{bc}^{+} - (-1)^n \pi/2$ at c, whose orthogonal quadrature $\varphi_{i,c} = -\varphi_{bc}^{+}$ results in enhanced transport from c to a. We are thus able to identify $\varphi_{ab}^{+} + \varphi_{bc}^{-} = \pi/2 + n\pi$ as the chiral transport regime for the whole open chain.

In the chiral case, the amplitude of the favored phase is enhanced (suppressed) twice through the two links with factor $\frac{(t \pm \Delta)}{\kappa}$ for each link,

$$\left|\Gamma_{ca}^{\pm}\right| = \kappa_{\text{ext}} \frac{\kappa}{\left(t^2 - \Delta^2 + \frac{\kappa^2}{2}\right)} \frac{(t \pm \Delta)}{\kappa} \frac{(t \pm \Delta)}{\kappa} \tag{5.22}$$

On the other hand, in the trivial case, an input phase is enhanced via the first link and then suppressed in the following link, and vice versa for the orthogonal phase,

$$\left|\Gamma_{ca}^{\pm}\right| = \kappa_{\text{ext}} \frac{\kappa}{\left(t^2 - \Delta^2 + \frac{\kappa^2}{2}\right)} \frac{(t + \Delta)}{\kappa} \frac{(t - \Delta)}{\kappa} \tag{5.23}$$

5.3.4 Instability in closed 3-site chain

We can also study how the closed 3-mode system approaches the instability threshold in the linear theory. We simplify the 6 complex couplings with equal coupling strengths

$\Delta_{ab} = \Delta_{bc} = \Delta_{ca} = \Delta$ and $t_{ab} = t_{bc} = t_{ca} = t$. The quantity that signals instability within the linear regime is the coefficient matrix determinant of the coupled Heisenberg-Langevin equations. We again focus on zero detuning $\delta\omega = 0$ first. The determinant has the notable feature that the link phases appear only through the combinations $\theta_a \equiv 2\left(\varphi_{ca}^{+} + \varphi_{ab}^{-}\right)$, $\theta_b \equiv 2\left(\varphi_{ab}^{+} + \varphi_{bc}^{-}\right)$, and $\theta_c \equiv 2\left(\varphi_{bc}^{+} + \varphi_{ca}^{-}\right)$:

$$\begin{aligned} D^c = {} & 4\,t^2\,\Delta^2\left[\left(t^2+\Delta^2\right)\cos\theta_a - t^2\cos\left(\theta_b+\theta_c\right) - \Delta^2\cos\left(\theta_b-\theta_c\right)\right] \\ & + 4\,t^2\,\Delta^2\left[\left(t^2+\Delta^2\right)\cos\theta_b - t^2\cos\left(\theta_a+\theta_c\right) - \Delta^2\cos\left(\theta_a-\theta_c\right)\right] \\ & + 4\,t^2\,\Delta^2\left[\left(t^2+\Delta^2\right)\cos\theta_c - t^2\cos\left(\theta_a+\theta_b\right) - \Delta^2\cos\left(\theta_a-\theta_b\right)\right] \\ & + 2t^2\,\Delta^4\cos\left(\theta_a-\theta_b-\theta_c\right) + 2t^2\,\Delta^4\cos\left(\theta_b-\theta_c-\theta_a\right) \\ & + 2t^2\,\Delta^4\cos\left(\theta_c-\theta_a-\theta_b\right) + 2t^6\cos\left(\theta_a+\theta_b+\theta_c\right) + C^c, \end{aligned} \tag{5.24}$$

Note that the terms in D^c that do depend on the pump phases are independent of loss rates. Where C^c is independent of the pump phases,

$$\begin{aligned} C^c = {} & \left[\kappa^3 + 3\kappa\left(t^2-\Delta^2\right)\right]^2 \\ & + 2\left[t^6 - 2\Delta^6 + 3t^2\Delta^4 - 4t^4\Delta^2\right] \end{aligned} \tag{5.25}$$

When all downconversion pumps are turned off, the only phase-dependent term in D^c is proportional to t^6, and simple algebra shows that D^c is positive definite as a function of pump phases. Once the downconversion pump strength is increased above a threshold value, D^c eventually becomes zero for certain pump phases, and the set of equations becomes singular: this is the point where the closed 3-mode system turns unstable in the linear theory. D^c becomes negative above the threshold.

At this point, we acknowledge that we can also discuss instability in terms of the eigenvalues of the coefficient matrix, following McDonald, Pereg-Barnea, and Clerk. If we multiply Eq. (5.10) by $-i$, then some of the eigenvalues of the coefficient matrix (corresponding to $\delta\omega$ of self-sustained eigenmodes) should have positive imaginary parts when the system becomes unstable, i.e. amplitudes of certain eigenmodes should grow with time. This is equivalent to monitoring the sign of the determinant D^c, although it could be easier to work with D^c directly when we are interested in the transport properties.

Eq. (5.24) allows an analytical minimization with respect to e.g. θ_b by explicitly expanding out the cosine and sine terms. Fortunately, the expression remains free of square roots after this minimization:

$$\begin{aligned} D^c \geq \text{const.} - 8t^2\Delta^2\big[& t^2\cos(\theta_a+\theta_c) + \Delta^2\cos(\theta_a-\theta_c) \\ & - \left(t^2+\Delta^2\right)\cos\theta_a - \left(t^2+\Delta^2\right)\cos\theta_c\big] \end{aligned} \tag{5.26}$$

Since cosines range between -1 and 1, it is clear by now that the minimum with respect to θ_a and θ_c is found at $\cos\theta_a = \cos\theta_c = -1$. Consistent with the 3-fold symmetry, at this point we also have $\cos\theta_b = -1$, i.e. $\varphi^+_{ab} + \varphi^-_{bc} = n\pi + \pi/2$, reminiscent of the chiral transport regime in the open 3-mode system. The minimum of D^c with respect to all link phases reads

$$D^c_{\min} = \left(\kappa^2 - 4g_\Delta^2\right)\left[3g_t^2 + (\kappa + g_\Delta)^2\right]\left[3g_t^2 + (\kappa - g_\Delta)^2\right]. \tag{5.27}$$

The threshold value of the pairing strength g_Δ is, therefore, $\kappa/2$ in the closed system, which is always less than the open system value $(\kappa^2/2 + g_t^2)^{1/2}$, which can be extracted from Eq. (5.12). Right at the threshold, since the minimum of D^c is found at $\cos\theta_a = \cos\theta_b = \cos\theta_c = -1$, it is clear that tuning away any of these three angles θ_a, θ_b, and θ_c should return the system to stability

Deviation from chiral gauge invariant case

It is clear now that to reach the instability; all link connections must be set at the gauge invariant phase to be in the chiral transport. We, therefore, can analyze the instability condition as a function of satisfying the phase condition for equal gauge phase values $\theta_a = \theta_b = \theta_c = \theta$:

$$D^c = 4\left(\left(t\cos\frac{\theta}{2}\right)^2 - \Delta^2 + \left(\frac{\kappa}{2}\right)^2\right), \tag{5.28}$$

The condition to reach instability is

$$\Delta > \sqrt{\left(t\cos\frac{\theta}{2}\right)^2 + \left(\frac{\kappa}{2}\right)^2}. \tag{5.29}$$

It is interesting to see that we retrieve the instability condition for the periodic boundary condition we reached before. It means that we can verify this condition experimentally on our small system.

Instability feature in the spectrum

Following the practice in the experiment, let us fix $\varphi^+_{ab} + \varphi^-_{bc} = n\pi + \pi/2$ (i.e., $\cos\theta_b = -1$), and identify $\varphi^\Delta_{ac} = -\frac{1}{2}(\theta_a + \theta_c) + \varphi^{\Delta,0}_{ac}$ and $\varphi^t_{ac} = \frac{1}{2}(\theta_a - \theta_c) + \varphi^{t,0}_{ac}$, where $\varphi^{\Delta,0}_{ac} = -\varphi^-_{ab} + \varphi^+_{bc}$

and $\varphi_{ac}^{t,0} = \varphi_{ab}^{-} + \varphi_{bc}^{+}$ are independent of the $a-c$ link. We can then single out the φ_{ac}^{t} and φ_{ac}^{Δ} dependence,

$$\begin{aligned} D^c = & \left[\kappa^3 + 3\left(t^2 - \Delta^2\right)\kappa\right]^2 \\ & + 4\left(t+\Delta\right)^3\left(t-\Delta\right)^3 \\ & - 4\left[2\Delta^2 t\cos\left(\varphi_{ac}^{\Delta} - \varphi_{ac}^{\Delta,0}\right) - \left(t^3 + \Delta^2 t\right)\cos\left(\varphi_{ac}^{t} - \varphi_{ac}^{t,0}\right)\right]^2 . \end{aligned} \tag{5.30}$$

Eq. (5.30) indicates that the minimum of D^c is found at:

$$\cos\left(\varphi_{ac}^{\Delta} - \varphi_{ac}^{\Delta,0}\right) = -\cos\left(\varphi_{ac}^{t} - \varphi_{ac}^{t,0}\right) = \pm 1$$

This result, derived from the earlier definitions, implies that either $\theta_a = \theta_c = \pi$ or $\theta_a = -\theta_c = \pi$. These conditions satisfy the non-trivial gauge invariant condition.

The spectrum structure of the 3-site closed chain is identical to the Creutz ladder depending entirely on the loop phases determined by the hopping phases. Let us define the loop phase as $\varphi_{loop} = \varphi_{ab}^{t} + \varphi_{bc}^{t} + \varphi_{ca}^{t}$. Taking into account $\theta_b = \pi$, $\varphi_{loop} = \frac{\pi}{2} - (\varphi_{ac}^{t} - \varphi_{ac}^{t,0})$, which is equivalent to phase in the second cosine. Interestingly, the instability happens at a certain $\varphi_{loop} = \pm\pi/2$, which coincides with one of the near-zero eigenmodes. The additional condition on φ_{ac}^{Δ} determines which one of those near-zero eigenmodes will experience amplification and reaches instability.

5.4 Simulating a 3-Site bosonic Kitaev chain

We program a chain of three sites in the synthetic frequency dimension as seen in Fig. 5.1(b). For the open chain geometry, the sites are connected by two links where each link is created by two coherent pumps: a pump at the modes' frequency difference to activate the hopping and a pump at the modes' sum frequency to activate the pairing potential. We inject four phase-locked coherent tones at the selected frequencies through an on-chip flux line coupled to the SQUID. The amplitudes and phases of these tones determine the same properties of the complex hopping and pairing terms. The coherent pump tones are generated using microwave sources whose references are locked in a daisy-chain fashion at 1 GHz. To impose periodic boundary conditions on the 3-site chain, we apply two additional pump tones which connect the open ends, forming a closed loop, as seen in Fig. 5.1(c).

5.4.1 Characterization and Calibration

We characterize the 3-site open chain by phase-sensitive transport measurements. We send in a probe tone around one site frequency and measure the reflected and transported signals at all other sites. The injected signal propagates through the chain and eventually leaks out, where it is then detected at the site frequencies via three RF digitizers. To observe the dependence of the transport on the input phase, the probe tone is set at a constant magnitude but with a phase that ramps at a constant rate from $-\pi$ to π. The phase-sensitivity of the transport converts the phase sweep of the input signal into magnitude variations in the output signals.

An arbitrary chain is calibrated by activating each link separately while turning off the remaining links. First, upon activating the hopping term of the link $(j, j+1)$, the single mode resonance splits into two resonances whose frequency difference gives twice the coupling strength, $2t_{j,j+1}$. We then set the $t_{j,j+1}$ to be roughly equal along the chain and in the strong-coupling limit. By strong coupling, we mean that the resonance splitting is resolved, i.e., that $t_{j,j+1} > \kappa_j, \kappa_{j+1}$ where κ_j and κ_{j+1} are the photon decay rates.

Then, we activate each link's pairing term. In this case, there is no simple spectral feature that quantifies the pairing strength, $\Delta_{j,j+1}$. We roughly calibrate $\Delta_{j,j+1}$ using transport measurements in the following way. With both hopping and pairing terms applied, we sweep the input phase of the signal described above at site j and measure the contrast of the transport at site $j+1$ as a function of phase, that is, the ratio of the maximum transport magnitude to the minimum. Since the contrast follows $\propto \frac{\Delta}{t}$ approximately, we then vary the pairing pump power, interpreting the power where the observed contrast is maximum as $\Delta_{ij} \approx t_{ij}$. Beyond this point in power, the system becomes dynamically unstable, as predicted. We chose a pairing strength such that it satisfies the topological metastability condition of $\Delta > \frac{\kappa}{2}$.

5.4.2 Twisted-tubes picture of the 3-site chain

The coupling phases control the direction of the transport between the sites' quadratures. We find it convenient to define the sum and difference phases, $\varphi^{\pm}_{j,j+1} = \left(\varphi^{t}_{j,j+1} \pm \varphi^{\Delta}_{j,j+1}\right)/2$, similar to the theory section. When a link is activated, due to the chiral nature of the transport, a certain quadrature will be favored and the respective orthogonal quadrature will be suppressed in the transport from site j to site $j+1$. Importantly, the favored quadrature may have different projections on the IQ plane at both sites, e.g. x_j could be transported to p_{j+1}, $x_j \to p_{j+1}$; it is $\varphi^{-}_{j,j+1}$ and $\varphi^{+}_{j,j+1}$ that determine the projections

of the favored quadrature at site j and site $j+1$ respectively. On the other hand, the orthogonal quadrature will dominate the transported signal in the opposite direction, i.e. $p_j \leftarrow x_{j+1}$ in this example. By programming the coupling phases on a single link, we can tune continuously between different transport scenarios: for instance, starting from $x_j \rightarrow p_{j+1}$ and $p_j \leftarrow x_{j+1}$, we can vary $\varphi^+_{j,j+1}$ to arrive at $x_j \rightarrow x_{j+1}$ and $p_j \leftarrow p_{j+1}$, or vary $\varphi^-_{j,j+1}$ to arrive at $p_j \rightarrow p_{j+1}$ and $x_j \leftarrow x_{j+1}$.

In the presence of more than one link, to intuitively understand the role of coupling phases in chiral transport, we use the twisted-tubes picture shown in Fig. 5.2. Each link is represented as a pair of interleaved directional tubes with elliptic cross-section, where blue tubes transport to the left and red tubes to the right. The elliptic cross section rotates along the direction of transport, and the major axis of the ellipse at either end of the tube indicates the projection of the favored quadrature on the corresponding site's IQ plane. Looking at site a on the left end, for instance, the major axis of the red ellipse shows the phase of the input signal that will be favored in transport to site b, whereas the major axis of the blue ellipse determines the phase of the signal transported to site a. The ends of the tube connecting a and b can be twisted by varying φ^-_{ab} and φ^+_{ab} as illustrated in Fig. 5.2(a). In the theoretical model, Eq. (5.1), it is easy to set the phases such that there is no twisting of the quadratures along the chain. It is not easy to do this in the experimental setting. However, twisting the ends of all tubes at a given site by the same angle amounts to a local gauge transformation, and only the gauge-invariant linear combinations of link phases, e.g. $\varphi^+_{ab} + \varphi^-_{bc}$, which determine the relative orientation of the tubes at the common site, are physically significant. Exploiting this gauge freedom, we can adjust the link phases to find the maximum (minimum) of transport, such that the quadratures are maximally aligned (misaligned) regardless of the local twisting.

5.4.3 Calibration of gauge invariant of the 3-site chain

To calibrate the 3-site chain, we twist the end of the $a-b$ tube at site b by varying φ^+_{ab} while keeping the ends of the $b-c$ tube unchanged, effectively changing the gauge-invariant phase. Figure 5.3 shows the measured phase-dependent transport when the signal is injected at the center site b as a function of φ^+_{ab}. The sinusoidal shape of the transport magnitudes to site a and site c reflects the transport sensitivity to the input phase where maximum (minimum) peaks correspond to the favored (suppressed) phases. While the transport to site c is roughly maintained constant at a certain favored input phase, $\phi_{in} = 0$, the favored phase in transport to site a continuously varies between $-180°$ to $180°$, resulting in two special cases. In the trivial case (red curves) at $\varphi^+_{ab} = -90°$, the same input phase is favored in transport to both chain ends, i.e. the transport magnitudes are in phase, indicating

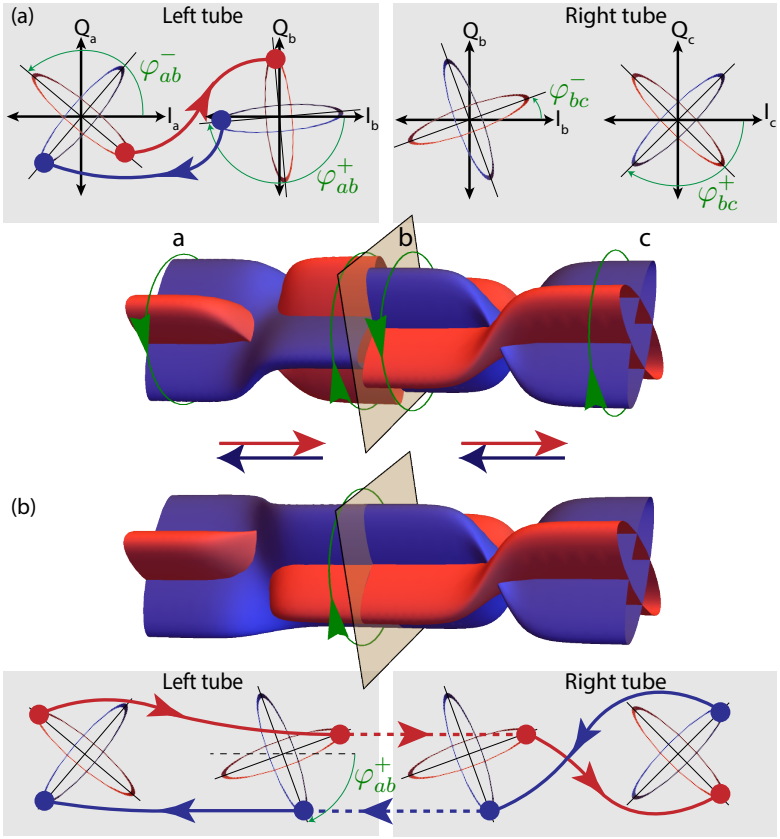

Figure 5.2: Twisted-tubes picture of the bosonic Kitaev chain. (a) Two connected links in a 3-site chain. Each link is represented by a pair of directional interleaved tubes, with blue (red) tubes describing transport to the left (right). The left (right) end of link ab can be twisted by varying the difference phase φ_{ab}^{-} (sum phase φ_{ab}^{+}). For a given transport direction, the major axis of the elliptical cross-section at the input (output) end determines the favored input (output) phase. The curved arrows connecting IQ planes depict how a signal evolves on the IQ plane as it propagates in the corresponding direction. The interface between the tubes at the common site b determines the transport across the 3-site system. In (a), transport is suppressed as the ends of the $a-b$ and $b-c$ tubes are misaligned at the common site b. That is, a signal propagating from left to right arrives at node b in the counterpropagating quadrature and is subsequently attenuated. In (b), by twisting the right end of the $a-b$ link and aligning the tubes, we create two continuous paths along the chain and realize a chiral chain.

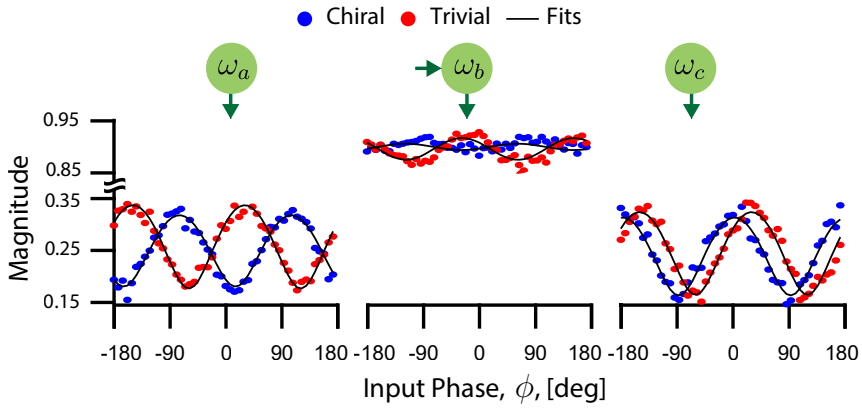

Figure 5.3: Calibration of the gauge-invariant phase of the 3-site open chain. The lattice cartoon depicts a signal injected in the center while reflected and transport signals are being probed. The magnitude and phase of the measured output signals are plotted as a function of the input phase in trivial (red) and chiral (blue) cases, as well as the theory fit (black). Note that all magnitudes of the transport signals are modulated along the input phase axis. However, while the trivial transport magnitudes are in phase, the chiral case magnitudes are out of phase.

that the same input phases get favored or suppressed. In the twisted-tubes picture, this corresponds to complete misalignment between the tube ends where they meet at site b where the projection of the red tube of a link matches with the projection of the blue tube of the other link, impeding chiral transport along the chain.

More interestingly, the chiral case (blue curves) is achieved at $\varphi^{+}_{ab} = 0°$ where the orthogonal input phases transport to the opposite ends as the tubes become perfectly aligned at the connection, and the transport magnitudes to the ends are completely out of phase. When the transport to site a is enhanced for a certain input phase, its transport to the other end at site c is highly suppressed; conversely, the transport of the orthogonal phase is suppressed to site b and enhanced to site c. This is in agreement with the projections of twisted tubes on the IQ plane being aligned at their meeting point at site b as shown in Fig. 5.2(b). This implies that we have established a chiral chain with two directional paths, where orthogonal quadratures transport along the chain in opposite directions.

5.5 Observation of the bosonic Kitaev chain features

5.5.1 Chiral transport properties of BKC

We investigate the chain chirality by performing phase-dependent transport measurements while sweeping the link phase φ_{ab}^{+} . This allows us to examine the transition between chiral and trivial regimes. The measurements, shown in Fig. 5.4, reveal interesting features that we associate with the bosonic Kitaev-chain model. By choosing the proper gauge-invariant phase obtained in the calibration process, the chain exhibits chiral transport properties. While the trivial regime is found to be a special case at $\varphi_{ab}^{+} = 90°$, the chiral regime emerges gradually from a small deviation around 90°, reaching maximum chiral transport at $\varphi_{ab}^{+} = 0°$. These two gauge-invariant phases align with the trivial and chiral cases established in the calibration.

Figure 5.5 illustrates the line cuts of phase-dependent transport between the chain ends in both the chiral and trivial cases. In the trivial case (red curves), the chain shows minimal changes in the transport signals regardless of the input phase. In fact, the transport is expected to be equivalent to a simple tight-binding model with hopping strength of $t - \Delta$. The transport magnitudes from site a to site c and vice versa indicate a constant transport of approximately 0.57, which will serve as a baseline for the chiral transport. Conversely, in the more interesting chiral case (blue curves), the chain transport between the ends exhibits a strong dependence on the input phase. In Fig. 5.5(a), for instance, the transport from site a to site c for an input phase of 0° is enhanced, compared to the baseline, while the transport of the orthogonal input phases at −90° and 90° are highly suppressed at a transport of about 0.31. Theoretically, we expect the ratio of enhanced and suppressed amplitudes, compared to the baselines, to be around $\frac{t+\Delta}{t-\Delta}$ and $\frac{t-\Delta}{t+\Delta}$, respectively.

An additional signature of chirality, illustrated in Fig. 5.5, is the flattening of the transport phase. In the chiral regime, the phase of the transport signal becomes largely independent of the input phase and is determined by the favored local quadrature at the corresponding site. This implies that the phase at the output of the tube is determined by the twisting of the tube itself, rather than the initial excitation phase. For instance, in Fig. 5.5(a), while the transport phase linearly follows the input phase in the trivial chain over a range of 90^0 , the phase in the chiral chain only varies by 35°.

We depict the measurements as injecting coherent excitations at chain ends with two orthogonal phases, as shown in Fig. 5.5(c). In the trivial case (red), the excitation phase plays no role in enhancing or suppressing its propagation. However, in the chiral case, an excitation at $\phi = 0°$ propagates to the right, while the propagation of an excitation with $\phi = 90°$ propagates to the left.

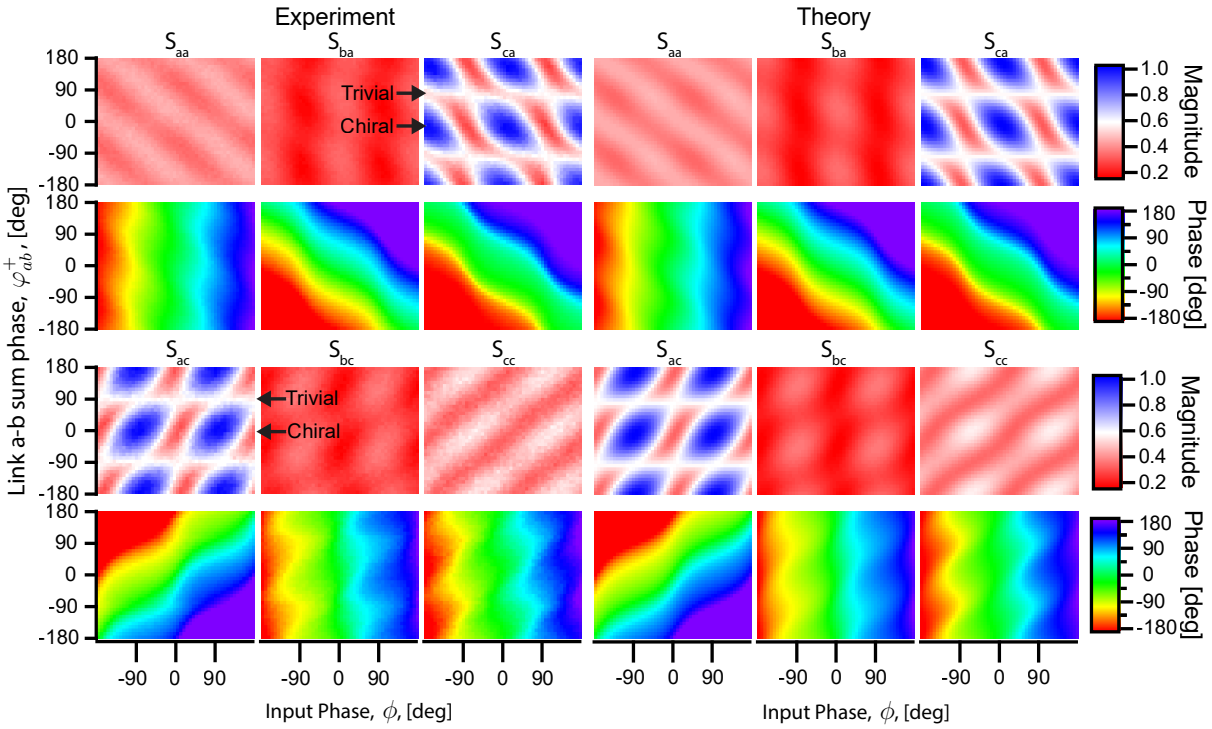

Figure 5.4: Transport of the 3-site open chain. The magnitude and phase of the experimental (left) and theoretical (right) output signals are plotted as functions of $a-b$ link sum phase, φ_{ab}^{+}, and input phase, ϕ. The labels $\{S_{mn}\}$ indicate the output signal at site m when the input signal is injected at site n. For instance, $\{S_{nn}\}$ gives the reflected signal off the input site n, while $\{S_{mn}\}$ corresponds to the transport in the chain from site n to site m. We clearly see that the transport between the chain ends, $\{S_{ac}, S_{ca}\}$, exhibits distinct features between the trivial regimes at $\varphi_{ab}^{+} = \pm 90°$ and the chiral regimes $\varphi_{ab}^{+} = 0°, \pm 180°$. While the trivial transport shows little to no dependence on the input phase, the blue regions highlight the chirality features due to transport magnitude sensitivity to the input phase

.

The observation of topological features under certain gauge invariant coupling phase is consistent with the theoretical prediction that the chain becomes fully chiral if the hopping terms in the Hamiltonian have purely imaginary coupling amplitudes in Eq. (5.1). In this case, the Hamiltonian has a nonzero winding in E-plane, i.e. nontrivial topology, as opposed to the trivial chain that can be reduced to only real hopping terms [33].

5.5.2 Sensitivity to periodic boundary conditions

We examine the sensitivity of the chiral chain to boundary conditions by setting $\varphi_{ab}^{+} = 0°$ and then connecting chain ends at sites a and c as shown in Fig. 5.1(d). We measure the reflection coefficients around the site frequencies using a vector network analyzer (VNA), while varying both hopping and pairing phases of the $a - c$ link, as seen in Fig. 5.6(a)–(c). The observed resonances can be viewed as the spectrum of the chain eigenmodes. The spectrum is centered at the frequency of the uncoupled site, while the frequency offset of an eigenmode is interpreted as the energy of mode in the rotating frame of the pumps.

The dominant pattern is the braiding of the chain spectrum as a function of φ_{ac}^{t}, which is largely determined by the loop phase defined as the sum of the hopping phases around loop [27] as seen in Fig. 5.6(a). For certain phase conditions, however, we observe discontinuities in the central branch of the spectrum, indicating that the chain is approaching dynamical instability.

It is remarkable that the instability is determined solely by the coupling phases (the pump amplitudes are constant), which is a manifestation of the transition from the trivial to the chiral regime. We note that instability happens only when the closed chain spectrum has a zero eigenmode, which occurs for two values of the loop phase. Consequently, the gauge-invariant phase condition for chirality is satisfied by a certain pairing phase. In the twisted-tubes picture, we rotate both ends of the $a - c$ tube until it is aligned with the other tubes where they meet, forming an uninterrupted path around the closed chain, as depicted in Fig. 5.6(e).

In the absence of dissipation, the initial excitation traverses the loop indefinitely, being amplified as it passes through each tube, resulting in dynamical instability for nonzero Δ. In our chain, at the pairing strength shown, the dynamics are dampened by local dissipation, leading only to a finite amplification as seen in Fig. 5.7 It is expected, under uniform coupling strength, that instability can be reached at $\Delta > \frac{\kappa}{2}$. We have confirmed that for higher pairing strength, the system becomes unstable, leading to coupled parametric oscillations of the modes. The instability under periodic boundary conditions has been shown to be a crucial sign of realizing the topologically metastable Bosonic Kitaev chain, which supports Majorona Bosons.

5.5.3 Wavefunctions localization in 3-site open chain

The spectrum of the open chain in both chiral and trivial regimes with N sites is identical. The eigenenergies of both models are equivalent to a tight-binding model with hopping

strength $\tilde{t} = \sqrt{t^2 - \Delta^2}$ and eigenenergies $E_n = \tilde{t}\cos k_n$, where $k_n = \frac{n\pi}{N+1}$ [33]. A chain with odd N sites have a zero-eigenmode for $k = \frac{\pi}{2}$. The eigenmode wavefunction is delocalized with the support at site j proportional to $\frac{2}{N+1}\sin^2(k_n j)$. Hence, the zero-eigenmode wave function does not have any support on even lattice sites. In our 3-site chain, it implies that the zero eigenmode will be only supported on the chain ends and that the reflection measurements will be identical in both trivial and chiral regimes.

Nevertheless, the stark difference lies in the spatial distribution of the x and p wavefunction parts in the chiral chain. In the trivial case, the x and p wavefunctions are simple standing waves $x_k, p_k = \sqrt{\frac{2}{N+1}}\sum_{j=1}^{N}\sin(k_n j)\, x_j, p_k$ with spatial support identical to the mode wavefunction. On the other hand, the x and p wavefunctions in the chiral chain are localized to either end of the chain as $x_k, p_k = \sqrt{\frac{2}{N+1}}\sum_{j=1}^{N}\sin(k_n j)e^{\pm r(j-1)}x_j, p_j$, where r is the squeezing parameter defined as $e^{2r} = \frac{(t+\Delta)}{(t-\Delta)}$. In our 3-site chain, the x wavefunction is localized at site c, while the support at site a is much weaker with a factor of $\frac{(t-\Delta)}{(t+\Delta)}$, whereas the support of p wavefunction is localized at site a with a factor of $\frac{(t+\Delta)}{(t-\Delta)}$ stronger compared to site c support. This is consistent with the transmission factors from site a to site c of x and p excitations in the absence of loss. Hence, we can interpret the support of the wavefunction parts from the transport measurements.

The transport signals from both ends of the chain for a particular input phase are normalized to infer the support of the eigenmodes. Figure 5.8 depicts the support of the x and p wavefunctions in both chiral and trivial cases. Even in a small 3-site chain, we observe strong localization of x and p on the right and left ends, respectively, in contrast to the trivial case where the wavefunctions are delocalized with equal weights on both ends.

5.6 Discussion

The pairing terms break the conservation of particle numbers as they create and destroy pairs of particles. This gives rise to a non-Hermitian dynamical matrix, although here these dynamics are the results of a coherent process in a Hermitian Hamiltonian [40]. Our work, then, can be naturally extended to implement effective non-Hermiticity, which has a wide range of applications in quantum sensing, entanglement dynamics, and topological band theory.

Furthermore, the realized 3-site system can also be used for a number of interesting applications. We can utilize the demonstrated chiral features as a phase-dependent quantum amplifier [33]. Alternatively, vacuum squeezing can be used to realize entangled multimode

states, which is a complex resource that can play a central role in, e.g., Gaussian boson sampling [42]. In addition to AQS, the model exhibits nonlinear dynamics in the above-threshold regime, $\Delta > t + \frac{\kappa}{2}$. For instance, we have observed coupled parametric oscillations in the system. The instability dynamics of the chiral closed chain in the nonlinear regime can be interesting to explore in future work.

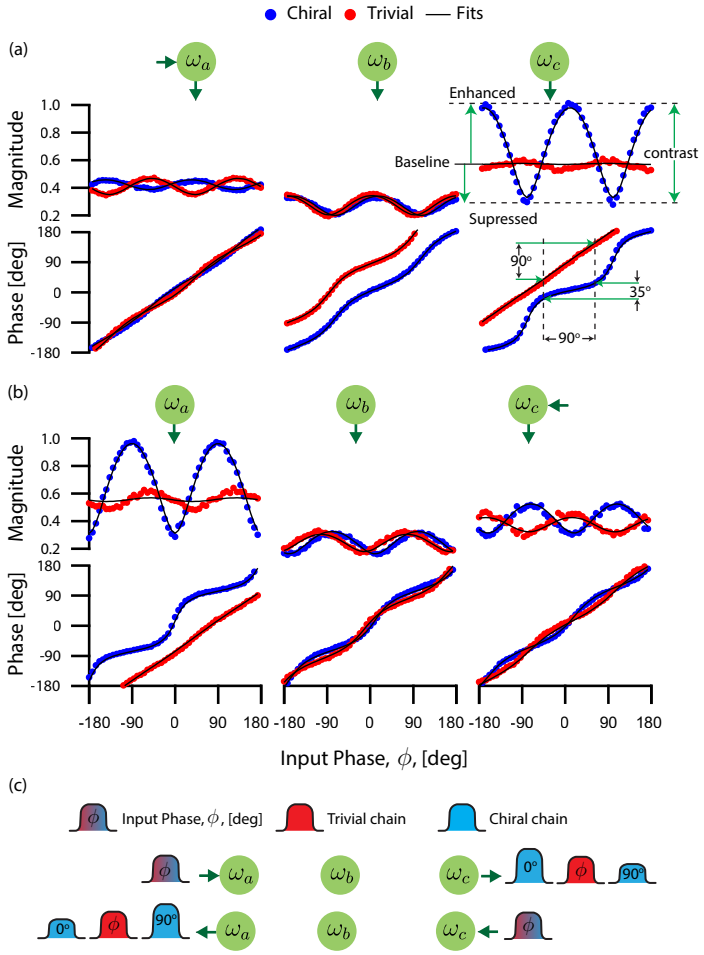

Figure 5.5: Transport of the 3-site open bosonic Kitaev chain at selected pump phases. Line cuts of Fig. 5.4 are shown for the chiral case at $\varphi_{ab}^{+} = 0°$ (blue curves) and the trivial case at $\varphi_{ab}^{+} = 90°$ (red curves) as well as the theory fit (black). (a) Signal injected at the left end. In the trivial case, the link phases are misaligned, and we measure phase-insensitive transport signals for all input phases. In the nontrivial (chiral) case, the transport magnitudes change with the input phase in a sinusoidal fashion. Moreover, the transported phase is flattened despite the fact that ϕ is swept in a continuous linear fashion, a strong indication of how the signal is propagated through a single quadrature. (b) When a signal is injected at the right end, in the chiral case, the enhanced input phase at $\phi = \pm 90°$ is orthogonal to the favored phase in the transport of the opposite direction. (c) a cartoon depicts the propagation of excitations with orthogonal input phases in trivial and chiral chains.

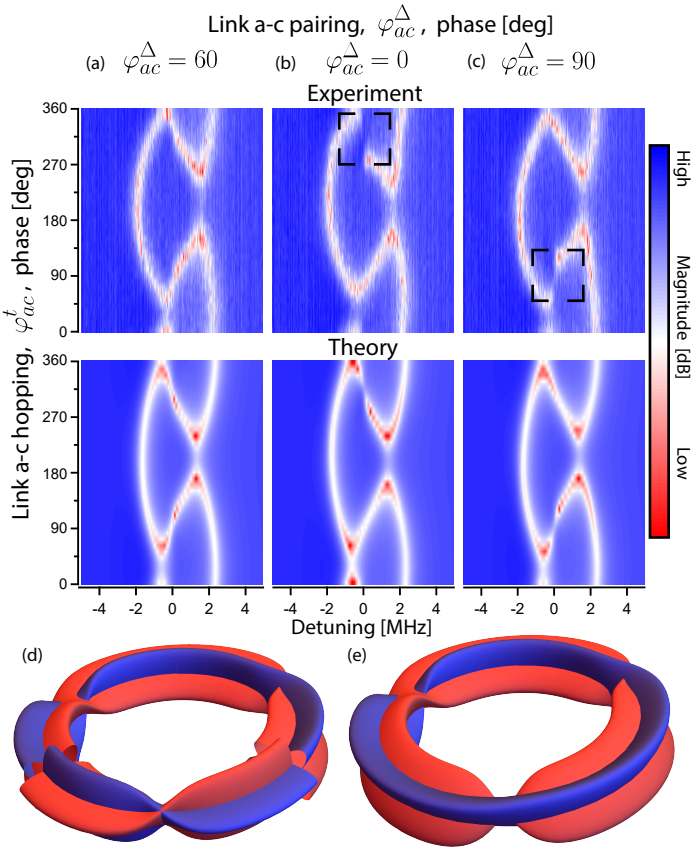

Figure 5.6: 3-site closed Kitaev chain spectrum. (a)–(c) The measured (top) and theory (bottom) reflection magnitudes at site b as functions of the $a-c$ hopping phase, φ_{ac}^{t}, and probe detuning from the uncoupled site frequency. (a) Spectrum at $\varphi_{ac}^{\Delta} = 60°$, the chain tubes are misaligned, reducing the total gain around the loop. In this case, sweeping φ_{ac}^{t} produces a braided spectrum typical of loops with only hopping. At (b) $\varphi_{ac}^{\Delta} = 0°$ and (c) $\varphi_{ac}^{\Delta} = 90°$, the braided spectrum is overall similar, but we observe discontinuities when the gauge-invariant phase satisfies the chirality condition at $\varphi_{ac}^{t} = 310°$ in (b) or $\varphi_{ac}^{t} = 90°$ in (c), indicated by the black squares. Offsetting φ_{ac}^{Δ} by 90° forces the discontinuity to jump from the top to the bottom zero eigenmodes. We note that the magnitudes of all pumps are constant in these plots, so the onset of instability is caused only by satisfying the chirality condition. Twisted-tubes depiction of the closed chain before alignment (d) and after alignment (e). The excitation traverses the red or blue loop indefinitely, depending on its initial phase.

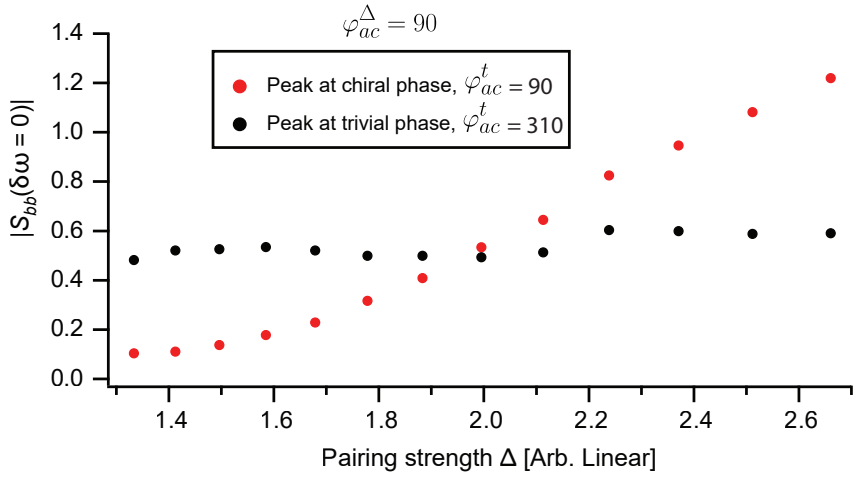

Figure 5.7: zero eigenmodes peak of the reflection at site b as a function of pairing strength in the closed chain. (black) in the trivial regime, increasing the pairing strength does not affect the zero-mode reflection peak. (red) in the chiral regime, the effective loss is reduced until we observe an amplified signal as the reflection coefficient reaches above 1

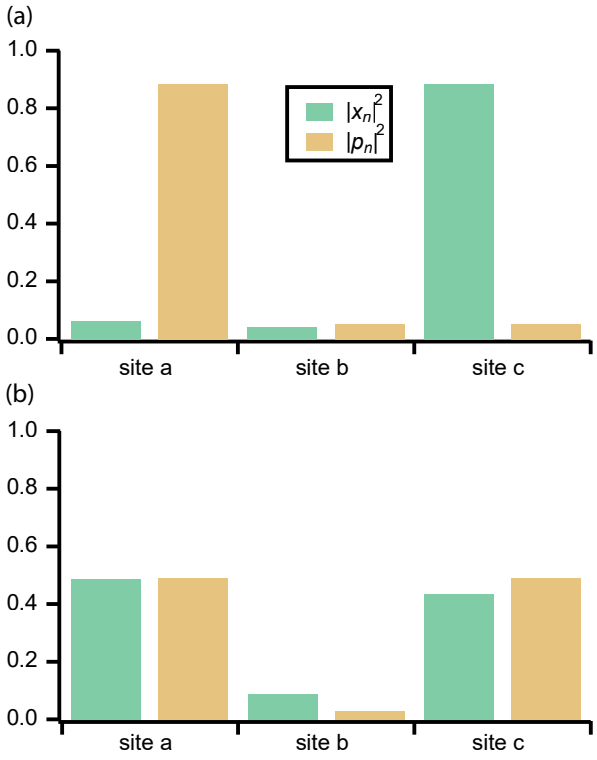

Figure 5.8: The support of x and p wave functions on lattice sites of the 3-site open chain. (a) The distribution of x and p parts of the wave function in the chiral regimes being localized on the chain ends. In the trivial regime, however, we see in (b) that the wave function delocalized with support on end sites only. Furthermore, in both cases, the zero eigenmode wavefunction does not have support in the center site

Chapter 6

Three-Body interaction

The parametric cavity-based ASO platform is capable of simulating static gauge fields indirectly by including their effect, as demonstrated in Chapter 4. However, the simulation of dynamics gauge fields, such as in Lattice Gauge Theories (LGTs) requires the explicit addition of the gauge field degrees of freedom. One approach to fully simulating dynamic fields involves engineering interactions beyond the standard two-body interactions accessible with quadratic Hamiltonians. The lowest order of these would be three-body interactions. In this chapter, we propose and implement a three-qubit device to achieve three-body interaction. We will dive into the design details and simulations of the energy levels and dynamics. Then, we show the experimental results, comparing them with theory.

The contributions to this work are as follows.

- I designed the three-qubit device.
- I fabricated the device with assistance from I. Nsanzineza.
- I conducted the experiments and collected data. Cindy Yang assisted in data collection.
- Z. Shi and I collaborated on fitting the data to the theory and reconstructing the model's Hamiltonian.
- I wrote this chapter independently.

6.1 Lattice gauge theories

A significant part of modern fundamental physics relies on the formalism of gauge theories. In fact, three out of the four forces of nature are considered gauge theories at the fundamental level [43]. These gauge theories are quantum field theories that have a special type of local symmetry known as gauge symmetry.

The first quantum gauge theory to be significantly developed was quantum electrodynamics (QED), which describes the quantum interaction between the electromagnetic field and electrically charged particles. QED is characterized by weak coupling and has been successfully treated using perturbation theory. With the success of QED, the concept of gauge theories was extended to both weak and strong nuclear forces. Also, a weakly-coupled theory, the weak force was successfully described by expanding the gauge symmetry group of QED, ultimately leading to the unified electroweak theory that combines the electromagnetic and weak nuclear forces.

However, as its name suggests, the strong nuclear force is strongly coupled and cannot generally be treated using perturbation theory. The fundamental theory of the strong force is known as quantum chromodynamics (QCD). Looking for ways to tackle QCD in 1972, Wilson proposed lattice gauge theories (LGTs), regularized by discretizing space-time, to deal with strong interaction regimes where perturbative approaches fail [44]. Over the past decades, LGTs have proved to be a powerful framework for overcoming challenging problems in many fields of physics. It has allowed advances in not only elementary particle physics but also in condensed matter physics [45, 46, 47], where it arises as an emergent theory [48, 49], such as in strongly correlated systems. Furthermore, a wide range of many-body systems can be transformed into a gauge theory via slave-particle or parton decomposition [50]. This technique involves fractionalizing the original degree of freedom into 'slave' degrees of freedom that interact with emergent gauge fields [51].

Monte Carlo simulations have established themselves as a key tool in classical simulations of LGTs. These simulations have proven invaluable in various fields of modern physics ranging from low-energy spectra [52, 53, 54], phase diagrams [55, 56, 57], to muon magnetic moment [58] and many others [59, 60]. Despite their proven efficiency, Monte Carlo methods still fail to simulate a wide range of essential problems in LGTs [6, 7]. Such problems include the time evolution of dynamics out of equilibrium [10] and models with finite fermion density [11]. The difficulty with these problems is due to the so-called sign problem, which prevents Monte Carlo simulations from converging or even properly defined [61].

In light of these limitations, quantum simulation has been proposed as a potential approach for investigating LGTs in strongly-interacting regimes [62, 63, 64, 65]. The

Hamiltonian of interest is either simulated digitally or by engineering systems that mimic it. One of the difficulties of using the digital approach is that the interaction terms may need to be broken down into a large set of two-qubit gates. For instance, the simulation of one-dimensional Z2 LGTs and the U(1) spin 1/2 models involves breaking down the interaction term into six two-qubit gates and three layers of single-qubit gates [66]. The situation quickly gets worse for U(1) LGTs when the gauge field is required to take more than two values, even in hardware-efficient simulation schemes. In addition, encoding the large bosonic Hilbert space of gauge fields in a small-scale quantum computer can be extremely challenging. Although promising approaches for the simulation of U(1) LGTs have been realized using trapped ions where the gauge fields are integrated out [67, 68, 69], these approaches are only valid for one-dimensional models and require additional long-range qubit-qubit interactions that are hard to realize, particularly in superconducting circuit platforms.

As a result, analog quantum simulation (AQS) has become an increasingly interesting approach to studying LGTs [70, 10, 71, 72, 73, 74]. This has motivated us to design and implement a building block for LGTs focusing on realizing the matter-gauge interaction term in the form of a three-qubit interaction in superconducting circuits. Gauge fields take different formulations depending on the phenomena studied and are characterized by the underlying (gauge) symmetry group of the system. One of the common gauge groups used to describe gauge fields is the U(1) symmetry group responsible for the emergence of the Gauss's law in QED, which describes a continuous symmetry of rotations on a unit circle. Furthermore, the infinite gauge Hilbert space can be truncated as spin S with discrete degrees of freedom without compromising the continuous symmetry U (1) in what is known as the quantum link model representation [46]. The simplest U(1) LGTs can be called U(1) spin 1/2 models [75], which consider a spin 1/2 gauge that takes only two possible values. In this chapter, we develop a platform for simulating U(1) spin 1/2 models commonly involved in describing coupled-spin systems, such as quantum spin liquids [76]. This simple yet nontrivial U(1) LGT model still allows for studying complex systems with gauge symmetries and investigating conservation laws, such as Gauss's law. It also shows exciting physics, such as confinement phase transition and spontaneous symmetry breaking [77, 66]. This mainly serves as a demonstration of our platform's capability of realizing the dynamical gauge-matter interaction. By generalizing the approach here, this platform should be able to extend the model to more sophisticated problems with larger gauge Hilbert spaces.

6.2 Theory of U(1) Lattice gauge theories

In general, in LGTs, spacetime is discretized into a lattice where the matter fields (massive particles) live on the lattice sites and the gauge fields live on the links connecting the sites. For simplicity, we consider the theory of one-dimensional U(1) - LGT with configuration depicted in Fig. 6.1(a).

Following [78] the Kogut-Susskind formulation of LGTs in a 1-dimensional staggered lattice, the Hamiltonian can be written as a sum of three terms: $\hat{\mathcal{H}}_m$, $\hat{\mathcal{H}}_g$, and $\hat{\mathcal{H}}_{mg}$. The first term, $\hat{\mathcal{H}}_m$, represents the energy of the matter fields and is given by:

$$\hat{\mathcal{H}}_m = \mu \sum_n (-1)^n \hat{\psi}_n^\dagger \hat{\psi}_n, \tag{6.1}$$

where $\hat{\psi}_n$ is the fermionic annihilation operator of the matter field on site n with rest mass μ.

The second term, $\hat{\mathcal{H}}_g$, represents the energy of the gauge fields

$$\hat{\mathcal{H}}_g = g_e \sum_n (\hat{E}_{n,n+1})^2, \tag{6.2}$$

where $\hat{E}_{n,n+1}$ is the electric field operator on the link connecting sites n and $n+1$, and g_e measures its energy.

The third term, $\hat{\mathcal{H}}_{mg}$, is the matter-gauge interaction. It is given by

$$\hat{\mathcal{H}}_{mg} = -J \sum_n \hat{\psi}_n^\dagger \hat{U}_{n,n+1} \hat{\psi}_{n+1}, \tag{6.3}$$

where J is the kinetic energy term, and the unitary gauge operator $\hat{U}_{n,n+1} = e^{i\hat{\theta}_{n,n+1}}$ with $\hat{\theta}_{n,n+1}$ corresponding to the vector potential. Here, the gauge field is represented by the canonical operators $\hat{E}_{n,n+1}$ and $\hat{\theta}_{n,n+1}$ which satisfy the commutation relation $[\hat{\theta}_{n,n+1}, \hat{E}_{m,m+1}] = i\hat{\delta}_{n,m}$. We see that the hopping of matter excitations is connected to the gauge fields. This term is invariant under local gauge transformations of matter $\hat{V}^\dagger \hat{\psi}_n \hat{V} = e^{i\alpha_n} \hat{\psi}_n$ and gauges $\hat{V}^\dagger \hat{U}_{n,n+1} \hat{V} = e^{i\alpha_n} \hat{U}_{n,n+1} e^{-i\alpha_{n+1}}$, where $\hat{V} = \prod_n e^{i\alpha_n \hat{G}_n}$. The U(1) local symmetry generator at site n is $\hat{G}_n = \hat{\psi}_n^\dagger \hat{\psi}_n - (\hat{E}_{n,n+1} - \hat{E}_{n-1,n}) + \frac{1}{2}[(-1)^n - 1]$. It is worth noting that, through Noether's theorem, gauge symmetries imply the conservation of a quantity in the system. For example, a system with translational symmetry implies the conservation of momentum in that system. In this view, the symmetry leads to a conservation law understood as a lattice version of Gauss's law in 1D quantum electrodynamics.

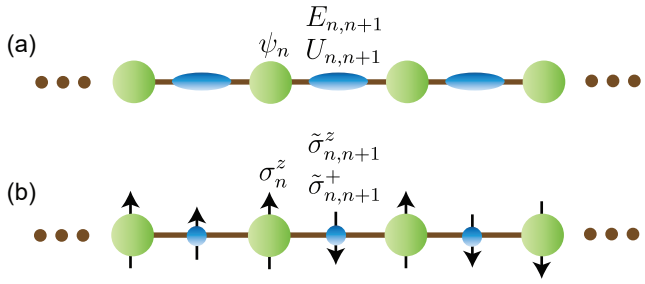

Figure 6.1: One-dimensional LGTs and quantum link representation. (a) depiction of 1D LGTs considers matter fields $\hat{\psi}_n$ living in lattice sites (green), coupled to U(1) gauge fields living on the links (blue) connecting the sites, defined by ($\hat{E}_{n,n+1}$, $\hat{U}_{n,n+1}$). (b) The LGTs picture using quantum link models, the gauge fields' Hilbert space is truncated to spin $\hat{S}$ operators, where it approaches the Wilson formulation in the limit of $S \to \infty$. In this work, we are concerned U(1) LGTs with link spin $\frac{1}{2}$, ($\hat{\tilde{\sigma}}^z_{n,n+1}$, $\hat{\tilde{\sigma}}^+_{n,n+1}$).

A convenient framework for dealing with LGTs in the context of quantum simulation is given by quantum link models (QLMs) [79]. The infinite Hilbert space of the gauge field is truncated by replacing it with spin S degrees of freedom with a $2S+1$-dimensional Hilbert space. In fact, QLMs can be considered a generalization of LGTs, as they include models relevant to condensed matter physics and quantum information theory [46]. In this work, we consider S = $\frac{1}{2}$ links and denote the link Pauli operators $\hat{\sigma}_{n,n+1}$, such that the unitary gauge operator $\hat{U}_{n,n+1}$ ($\hat{U}^\dagger_{n,n+1}$) maps to $\hat{\sigma}^-_{n,n+1}$ ($\hat{\sigma}^+_{n,n+1}$), and the electric field operator $\hat{E}_{n,n+1}$ maps to $\hat{\sigma}^z_{n,n+1}$. The relevant Hamiltonian terms are rewritten as $(\hat{\sigma}^z_{n,n+1})^2 = 1$ for the gauge energy term and $\hat{\psi}^\dagger_n \hat{\sigma}^-_{n,n+1} \hat{\psi}_{n+1}$ for the interaction term.

While superconducting circuits, and many other platforms, lack inherently fermionic building blocks, one can still map one-component fermions to spin $\frac{1}{2}$ in a one-dimensional lattice using the Jordan-Wigner transformation [79]:

$$\begin{aligned} \hat{\psi}_n &= (-1)^{\sum_{i<n}(\hat{\sigma}^z_i+1)/2}\hat{\sigma}^-_n, \\ \hat{\psi}^\dagger_n &= (-1)^{\sum_{i<n}(\hat{\sigma}^z_i+1)/2}\hat{\sigma}^+_n, \\ \hat{\psi}^\dagger_n \hat{\psi}_n &= (\hat{\sigma}^z_n + 1)/2. \end{aligned} \tag{6.4}$$

And the final (1+1)D U(1) - LGT Hamiltonian , depicted in Fig. 6.1(b), can be written as

$$\hat{\mathcal{H}}_m = \mu \sum_n (-1)^n (\hat{\sigma}^z_n + 1)/2 - J \sum_n \hat{\sigma}^+_n \hat{\sigma}^-_{n,n+1} \hat{\sigma}^-_{n+1} \tag{6.5}$$

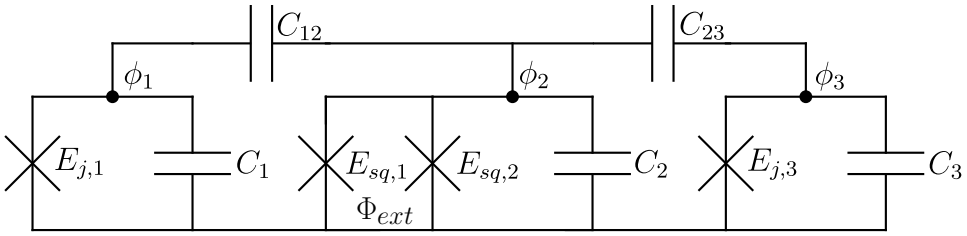

Figure 6.2: The circuit schematic of the three-qubit Device. Qubits 1 and 3 are fixed frequency transmon qubits, i.e. a Josephson junction shunted with a capacitor, representing the matter sites. Qubit 2 is a tunable transmon qubit, i.e., a SQUID shunted with a capacitor. The qubits are coupled with capacitors C_{12} and C_{23}. The external flux, Φ_{ext}, is applied to activate the three-body interaction parametrically.

The three-body interaction term in the Hamiltonian ensures that the gauge fields and matter particles evolve in a way that respects the gauge symmetries of the system. Importantly, the local symmetry in U(1) LGTs is still respected in QLM with spin $\frac{1}{2}$ links, which maintain Gauss's law defined by the modified symmetry generator

$$\hat{G_n} = (\hat{\sigma}^z_n + 1)/2 - (\hat{\sigma}^z_{n,n+1} - \hat{\sigma}^z_{n-1,n}) + \frac{1}{2}[(-1)^n - 1]. \tag{6.6}$$

where the charge in site n is represented by $(\hat{\sigma}^z_n + 1)/2$, while the electric field divergence is calculated as the difference of the electric field spin states between the links connected to that site.

6.3 c-QED implementation of three-body interaction

We design a superconducting circuit to realize the interaction building block for U(1) LGTs. The building block resembles a two-site lattice and a mediating gauge field in a link. A transmon qubit is convenient for representing lattice sites and links as spin-1/2 systems. The circuit design is shown in Fig. 6.2 where we have three transmon qubits capacitively coupled in a chain fashion. The middle qubit is designed with an asymmetric SQUID, which will allow us to control and activate the interactions parametrically.

6.3.1 Hamiltonian Formulation

The Hamiltonian of the system is derived below. We define a flux vector, $\Phi = (\phi_1, \phi_2, \phi_3)$, where ϕ_n represents the flux variable at qubit n. The capacitance matrix of the circuit can be written as

$$\mathcal{C} = \begin{bmatrix} C_1 + C_{12} & -C_{12} & 0 \\ -C_{12} & C_2 + C_{12} + C_{23} & -C_{23} \\ 0 & -C_{23} & C_3 + C_{23} \end{bmatrix}, \tag{6.7}$$

where C_n is the capacitor at qubit n, and $C_{n,m}$ is the coupling capacitance between qubits n and m. In the standard way, the kinetic energy of the system is considered to be the charging energy of the circuit capacitances and reads,

$$\mathcal{T} = \frac{1}{2}\dot{\Phi}^{\intercal}\mathcal{C}\dot{\Phi}. \tag{6.8}$$

The diagonal elements represent the qubit charging energies, and the nonzero off-diagonal elements are the capacitive coupling terms $\propto \dot{\phi_n}\dot{\phi_m}$.

On the other hand, the potential energy of the circuit is taken to be the inductive energy, in this case, stored in the junctions and SQUID:

$$\mathcal{U} = \sum_n U_{J,n} + U_{SQ},$$

where $U_{J,n}$ are the junction energies of qubit 1 and 3 defined in Eq. 2.5, and U_{SQ} is the SQUID energy, Eq. 2.16, all of which are functions of the flux at the junctions.

6.3.2 SQUID energy approximation with an external flux

To realize the parametric interaction, we operate the SQUID such that a maximum coupling strength is achieved for the desired interaction. External flux consists of a DC flux ϕ_b, for biasing the SQUID energy, and an AC flux signal $\phi_p(t)$, for the parametric drive. AC flux is assumed to be small, $\phi_p(t) << \frac{\Phi_0}{2\pi}$, for minimum perturbation to the system energy, while the DC flux bias is set at zero, $\phi_b = 0$, such that the odd terms in the Taylor expansion of the SQUID energy are at a maximum. In this regime, the external flux cosine and sine terms are approximated as $\cos\left(\pi\frac{\phi_p(t)}{\Phi_0}\right) \approx 1$, and $\sin\left(\pi\frac{\phi_p(t)}{\Phi_0}\right) \approx \pi\frac{\phi_p(t)}{\Phi_0}$. The SQUID energy can then be separated into static and time-dependent components as

$$U_{SQ} = U_{SQ,0} + U_{SQ,t}\,, \tag{6.9}$$

$$U_{SQ,0} = -E_\Sigma \cos\left(2\pi \frac{\phi_2}{\Phi_0}\right), \tag{6.10}$$

$$U_{SQ,t} = E_\Delta \pi \frac{\phi_p(t)}{\Phi_0} \sin\left(2\pi \frac{\phi_2}{\Phi_0}\right). \tag{6.11}$$

The first term, $U_{SQ,0}$ is the static SQUID energy, and the second term, $U_{SQ,t}$, is the time-dependent part, as it includes the parametric drive, which will be treated later when we discuss the parametric interaction.

6.3.3 Junction and SQUID as nonlinear inductors

Similarly to 2, the qubits are treated as nonlinear resonators by Taylor expanding the junction energies and the static SQUID energy to the fourth order in the flux variable. In this approximation, the junctions and SQUID can be considered nonlinear inductors, such as

$$U = -E\cos\left(2\pi\frac{\phi}{\Phi_0}\right) \approx E(\frac{2\pi}{\Phi_0})^2\frac{\phi^2}{2} - E(\frac{2\pi}{\Phi_0})^4\frac{\phi^4}{24}. \tag{6.12}$$

The quadratic term is treated as the energy of an effective inductance $L = \frac{1}{E}(\frac{\Phi_0}{2\pi})^2$, defined from now on as $U_L = \frac{\phi^2}{2L}$. On the other hand, the quartic term, which we define as U_p onward, represents the nonlinearity of the system. All the junctions and SQUID terms are summed up to reach the final expression of the system's potential energy,

$$\mathcal{U} \approx \sum_n (U_{L,n} - U_{p,n}) + U_{SQ,t}.$$

6.4 The system Hamiltonian as coupled oscillators

To solve for the dynamics of the system, we first proceed to solve the linear part of the system by dropping the nonlinear parts $U_{p,n}$, and the time-dependent part $U_{SQ,t}$, of the potential energy, which will be treated perturbatively later. The potential energy of the linear system of coupled oscillators, $\mathcal{U}_0$, can be written in the matrix form as

$$\mathcal{U}_0 = \frac{1}{2}\Phi^\intercal L^{-1}\Phi, \tag{6.13}$$

where L^{-1} is the inverse of the inductance matrix defined

$$L^{-1} = \begin{bmatrix} \frac{1}{L_1} & 0 & 0 \\ 0 & \frac{1}{L_2} & 0 \\ 0 & 0 & \frac{1}{L_3} \end{bmatrix}. \tag{6.14}$$

We next write down the Lagrangian $\mathcal{L} = \mathcal{T} - \mathcal{U}_0$ as

$$\mathcal{L} = \frac{1}{2}\dot{\Phi}^\intercal C\dot{\Phi} - \frac{1}{2}\Phi^\intercal L^{-1}\Phi. \tag{6.15}$$

Since L^{-1} and C do not necessarily commute, we cannot find a unitary transformation that diagonalizes both Lagrangian terms. However, diagonalization can still be done assuming that either L or C is a positive definite matrix, which is reasonable given the physical constraint that inductances and capacitances are positive. Here, the inductance matrix is clearly positive definite, represented by a simple diagonal matrix with positive definite entries. Nevertheless, to present a generic approach that includes both L and C couplings, we diagonalize the Lagrangian starting with the diagonalization of the capacitance matrix.

The positive capacitance matrix can be written as $C = V_c\Omega_c V_c^\intercal$ using eigenvalue decomposition, where V_c is the eigenvector matrix and Ω_c is the eigenvalue matrix. Recalling that $V_c V_c^\intercal = I$, it is straightforward then to define the new coordinate as $\tilde{\Phi} = \sqrt{\Omega_c}V_c^\intercal\Phi$, and rewrite the Lagrangian in terms of it as

$$\mathcal{L} = \frac{1}{2}\dot{\tilde{\Phi}}^\intercal\dot{\tilde{\Phi}} - \frac{1}{2}\tilde{\Phi}^\intercal\Omega\tilde{\Phi}, \tag{6.16}$$

where $\Omega = (\sqrt{\Omega_c})^{-1}V_c^\intercal L^{-1}V_c(\sqrt{\Omega_c})^{-1} = (\sqrt{\Omega_c}V_c^\intercal LV_c\sqrt{\Omega_c})^{-1}$. Now the eigenmodes of the system can be found by applying an eigenvalue decomposition to Ω such that $\Omega = V\Lambda V^\intercal$, where V is the eigenvector matrix, and Λ is the eigenvalue matrix. The coordinates of the eigenmodes are defined as $\Psi = V^\intercal\tilde{\Phi}$, and the diagonalized Lagrangian reads,

$$\mathcal{L} = \frac{1}{2}\dot{\tilde{\Phi}}^\intercal VV^\intercal\dot{\tilde{\Phi}} - \frac{1}{2}\tilde{\Phi}^\intercal V\Lambda V^\intercal\tilde{\Phi} = \frac{1}{2}\dot{\Psi}^\intercal\dot{\Psi} - \frac{1}{2}\Psi^\intercal\Lambda\Psi. \tag{6.17}$$

From this point, the derivation of the Hamiltonian of a harmonic oscillator is quite standard, so we largely just write the results. We find that the Hamiltonian of the system is

$$\mathcal{H}_0 = \frac{1}{2}Q^\intercal Q + \frac{1}{2}\Psi^\intercal\Lambda\Psi, \tag{6.18}$$

where Q is the vector conjugate momentum of Ψ defined

$$Q = \frac{\partial\mathcal{L}}{\partial\dot{\Psi}} = \dot{\Psi}. \tag{6.19}$$

The diagonalized Hamiltonian can be thought of as a set of decoupled oscillators with mass $= 1$. The frequency of the oscillator n is then the square root of the n-th element of the diagonal matrix Λ, i.e., $\omega_n = \sqrt{\lambda_n}$. We can then rewrite the Hamiltonian as

$$\mathcal{H} = \sum_n \left(\frac{q_n^2}{2} + \frac{1}{2}\omega_n^2\psi_n^2\right). \tag{6.20}$$

Following the standard program of canonical quantization, we can then promote the q_n and ψ_n to operators and impose canonical commutation relations with $\hbar = 1$. Once the system is quantized, the Hamiltonian can also be written in the bosonic operator representation as

$$\hat{\mathcal{H}}_0 = \sum_n \omega_n (\hat{a}_n^\dagger \hat{a}_n + \frac{1}{2}), \tag{6.21}$$

where ω_n is the eigenfrequency, and $\hat{a}_n$ is the lowering operator of the eigenmode n. The constant term $\frac{\omega_n}{2}$ represents the vacuum energy in mode n. Here, the eigenmode operator $\hat{\psi}_n$ is defined in terms of the lowering and raising operators as

$$\hat{\psi}_n = \frac{1}{\sqrt{2\omega_n}} (\hat{a}_n + \hat{a}_n^\dagger). \tag{6.22}$$

It is also useful to relate the set of eigenmode coordinates to the original uncoupled coordinates using the transformation matrix $B = L^{\frac{1}{2}} V$. For given coordinate m, the relation is

$$\hat{\phi}_n = \sum_m \beta_{n,m} \hat{\psi}_m, \tag{6.23}$$

where $\beta_{n,m}$ is the matrix element of B at row n and column m.

6.4.1 Treatment of the perturbative part

Now, the perturbative term U_p is redefined in terms of the eigenmodes, using Eq. 6.23, to find correction and coupling terms.

$$\hat{U}_p = -\sum_n (\frac{2\pi}{\Phi_0})^2 \frac{\hat{\phi}_n^4}{24 L_n} = -\sum_n (\frac{2\pi}{\Phi_0})^2 \frac{(\sum_m \beta_{n,m} \hat{\psi}_m)^4}{24 L_n} = -\sum_n (\frac{\pi}{\Phi_0})^2 \frac{(\sum_m \frac{\beta_{n,m}}{\sqrt{\omega_m}} (\hat{a}_m + \hat{a}_m^\dagger))^4}{24 L_n} \tag{6.24}$$

When the quartic term is expanded, we end up with terms mixing the lowering and raising operators of the different eigenmodes. However, most of those terms are fast-rotating terms except for those in the form of $\hat{a}_n^\dagger \hat{a}_n \hat{a}_m^\dagger \hat{a}_m$. Using the RWA, we keep only the static terms for the first-order perturbation theory results. This gives

$$\hat{U}_p = -\sum_{n,m} \chi_{n,m} \hat{a}_n^\dagger \hat{a}_n \hat{a}_m^\dagger \hat{a}_m. \tag{6.25}$$

When $n = m$, $\chi_{n,m} = (\frac{\pi}{\Phi_0})^2 \frac{1}{4\omega_n^2} \sum_k \frac{\beta_{k,m}^4}{L_k}$ defines the mode nonlinearity, which creates the anharmonicity of the qubit. Coming from quantum optics, this form of nonlinearity is

often called Kerr nonlinearity. When $n \neq m$, $\chi_{n,m} = (\frac{\pi}{\Phi_0})^2 \frac{1}{2\omega_n\omega_m} \sum_k \frac{\beta_{k,n}^2 \beta_{k,m}^2}{L_k}$ defines the cross-Kerr coupling between the qubit modes.

For the transmons in our circuit, the nonlinearity is designed to be large enough so that the system can be treated as an effective two-level system (qubit). We can therefore rewrite the Hamiltonian making the two-level approximation for each qubit:

$$\hat{\mathcal{H}} = \sum_n \frac{\omega_n}{2} \hat{\sigma}_n^z - \sum_{n<m} \chi_{n,m}\, \hat{\sigma}_n^z \hat{\sigma}_m^z \tag{6.26}$$

where $\hat{\sigma}_z = |0\rangle\langle 0| - |1\rangle\langle 1|$. In addition, the flux operators as defined earlier in Eq. 6.22 can be rewritten by reducing the lowering and raising operator to Pauli operators:

$$\hat{\psi}_n = \frac{1}{\sqrt{2}}(\hat{\sigma}_n^- + \hat{\sigma}_n^+) \tag{6.27}$$

where $\hat{\sigma}^- = |0\rangle\langle 1|$ and $\hat{\sigma}^+ = |1\rangle\langle 0|$. The system in its static state represents three qubits at different frequencies with only ZZ couplings. Although this type of coupling is not present in LGTs theory discussed earlier, $\mathbf{U}(1)$ is still preserved in the presence of those terms as they commute with the symmetry generator in Eq. 6.6.

6.4.2 Realizing the parametric interaction

Finally, we proceed to treat the time-dependent term, $\hat{U}_{SQ,t}$, in order to realize the proper parametric interaction that simulates the three-body term in LGTs, $\hat{\sigma}_n^+ \hat{\sigma}_{n,n+1}^+ \hat{\sigma}_{n+1}^-$. The first step is to write $\hat{U}_{SQ,t}$ in terms of the eigenmodes as follows:

$$\hat{U}_{SQ,t} = \frac{\pi E_\Delta}{\Phi_0} \phi_p(t) \sin\left(2\pi \frac{\sum_m \beta_{2,m}\, \hat{\psi}_m}{\Phi_0}\right) \tag{6.28}$$

Since the three-body interaction requires third-order mixing of the qubits, we only need to keep the third-order term of the sine expansion. We substitute $\hat{\psi}_m$ by the Pauli operator representation in Eq. 6.27 as

$$\hat{U}_{SQ,t} = \frac{2\sqrt{2}}{3} (\frac{\pi}{\Phi_0})^4 E_\Delta \phi_p(t) (\sum_m \frac{\beta_{2,m}}{\sqrt{\omega_m}} (\hat{\sigma}_m^- + \hat{\sigma}_m^+))^3. \tag{6.29}$$

Now, we can include the energy terms and write the Hamiltonian of the system, neglecting the ZZ couplings:

$$\hat{\mathcal{H}} = \sum_m \frac{\omega_m}{2} \hat{\sigma}_m^z + E_\Delta \phi_p(t) (\sum_m g_m\, (\hat{\sigma}_m^- + \hat{\sigma}_m^+))^3, \tag{6.30}$$

where we defined $g_m = \frac{1}{\sqrt[3]{3}}(\frac{\pi}{\Phi_0})^{\frac{4}{3}}\sqrt{\frac{2}{\omega_m}}\beta_{2,m}$. The system dynamics are captured by moving to the interaction picture via the unitary transformation $\hat{U} = e^{\frac{i}{\hbar}\hat{\mathcal{H}}_0 t}$, where $\hat{\mathcal{H}}_0 = \sum_m \frac{\omega_m}{2}\hat{\sigma}_m^z$,

$$\begin{aligned}\hat{\mathcal{H}}_{int} &= i\hbar\dot{\hat{U}}\hat{U}^\dagger + \hat{U}\hat{\mathcal{H}}\hat{U}^\dagger = E_\Delta\phi_p(t)(\sum_m g_m(\hat{\sigma}_m^- e^{-i\omega_m t} + \hat{\sigma}_m^+ e^{i\omega_m t}))^3 \\ &= E_\Delta\phi_p(t)\sum_{n,m,k} g_n g_m g_k \sum_{S_n,S_m,S_k\in\{+,-\}} \hat{\sigma}_n^{S_n}\hat{\sigma}_m^{S_m}\hat{\sigma}_k^{S_k} e^{i(S_n\omega_n + S_m\omega_m + S_k\omega_k)t},\end{aligned} \tag{6.31}$$

where we expanded the cubic bracket in the first line. The Hamiltonian essentially contains a sum of three-body terms in the form of $\hat{\sigma}_n^{S_n}\hat{\sigma}_m^{S_m}\hat{\sigma}_k^{S_k}$ of all possible permutations of the system's qubits n, m, k , and the possible variation of $S_n \in \{+, -\}$, which denotes whether the operator $\hat{\sigma}$ is a raising operator $\hat{\sigma}^+$ or a lowering operator $\hat{\sigma}^-$. In the RWA, all of these terms rotate at a non-zero frequency equal to $S_n\omega_n + S_m\omega_m + S_k\omega_k$, effectively causing little to no effect on the system dynamics unless a counter-rotating factor is introduced to cancel out the rotating frequency. The proper term in our Hamiltonian that corresponds to the three-body term in LGTs, $\hat{\sigma}_n^+\hat{\sigma}_{n,n+1}^+\hat{\sigma}_{n+1}^-$, clearly is $\hat{\sigma}_n^+\hat{\sigma}_m^+\hat{\sigma}_k^-$, which rotates at a frequency equals to $\omega_n + \omega_m - \omega_k$. To cancel out the term's rotation, we can apply a pump signal in the form: $\phi_p = \alpha_p \cos[\omega_p t]$, where $\omega_p = \omega_1 + \omega_2 - \omega_3$, resulting in a non-rotating term $\hat{\sigma}_1^+\hat{\sigma}_2^+\hat{\sigma}_3^- + \hat{\sigma}_1^-\hat{\sigma}_2^-\hat{\sigma}_3^+$ as follows:

$$\begin{aligned}\hat{\mathcal{H}}_{int} &= E_\Delta\alpha_p\cos[\omega_p t]\sum_{n,m,k} g_n g_m g_k \sum_{S_n,S_m,S_k\in\{+,-\}} \hat{\sigma}_n^{S_n}\hat{\sigma}_m^{S_m}\hat{\sigma}_k^{S_k} e^{i(S_n\omega_n + S_m\omega_m + S_k\omega_k)t} \\ &= E_\Delta\frac{\alpha_p}{2}\sum_{n,m,k} g_n g_m g_k \sum_{S_n,S_m,S_k\in\{+,-\}} \hat{\sigma}_n^{S_n}\hat{\sigma}_m^{S_m}\hat{\sigma}_k^{S_k} e^{i[(S_n\omega_n + S_m\omega_m + S_k\omega_k)\pm(\omega_1+\omega_2-\omega_3)]t} \\ &= E_\Delta\frac{\alpha_p}{2} g_1 g_2 g_3[\hat{\sigma}_1^+\hat{\sigma}_2^+\hat{\sigma}_3^- + \hat{\sigma}_1^-\hat{\sigma}_2^-\hat{\sigma}_3^+],\end{aligned} \tag{6.32}$$

where RWA is applied by dropping fast-rotating terms. The frequency cancellation occurs only when $n = 1$, $m = 2$, $k = 3$, in two cases $S_1 = +, S_2 = +, S_3 = -$ and $S_1 = -, S_2 = -, S_3 = +$. Finally, we change the qubit subscripts to follow the LGTs notations ($\hat{\sigma}_1 \to \hat{\sigma}_1$, $\hat{\sigma}_2 \to \hat{\sigma}_{1,2}$, $\hat{\sigma}_3 \to \hat{\sigma}_2$) to obtain the interaction Hamiltonian,

$$\mathcal{H}_{int} = g\alpha_p(\hat{\sigma}_1^+\hat{\sigma}_{1,2}^+\hat{\sigma}_2^- + h.c.). \tag{6.33}$$

6.4.3 Interpretation/simulation of Gauss's law

We provide an example of how the system can be viewed as the simplest 2-site U(1) LGT while maintaining Gauss's law, depicted in Fig. 6.3. The matter sites are represented by

qubit 1 (site 1) and qubit 3 (site 2), where the states 0 and 1 encode the absence and presence of an electron at the site, respectively. In addition, qubit 2 encodes the electric field where states 0 and 1 represent the electric field pointing to the left or right, respectively. The system was initialized at $|001\rangle$ encoding an electron at site 2 with the electric field pointing to the left, satisfying Gauss's law. Once the three-body interaction is activated, the system starts evolving toward state $|110\rangle$, simulating an electron hopping from site 2 to site 1 while simultaneously flipping the direction of the electric field to the right. This illustrates that the fundamental process of conserving Gauss's law via the three-body interaction is successfully captured in our system.

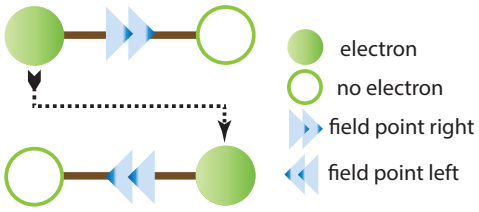

Figure 6.3: Simulation of 2-site U(1) LGTs. The simulation mimics the behavior of the electric field as the electron jumps from left to right. The lattice state satisfies Gauss's law at any moment in time, in the sense that the electric field points out of the charge. This is hard to achieve using sequential approaches as those will result in breaking Gauss's Law at intermediate times as the field state flips before the electron hops or vice versa.

6.4.4 Design and Simulation

CAD drawings of the device design are shown in Fig. 6.4. The design of a parametric system often requires that qubits be detuned in the initial state so that they do not interact unless the parametric process is involved. To ensure proper detunings and placement of resonators and qubit frequencies within the bandwidth of our measurement setup ($4-8$GHz), we placed the qubits in the lower range between $4.5-5.5$ with about 500MHz spacing to avoid crossing and difficult identification of higher-energy transitions. The readout resonators were placed around $7-8$GHz to allow for decent qubit-resonator detuning large than 2 GHz.

The anharmonicity of the qubits was chosen to be 250 MHz, which from Eq. 2.43 sets the total capacitance of each qubit island to be around 80 fF. Taking this into account, the qubit frequency determined the effective junction inductances as $15.5, 12.5, 10.5$ nH. The qubit-qubit coupling was also set at 160 MHz with the determined qubit capacitance; the

coupling capacitance can be estimated at 5fF using $g = \frac{Cg}{2\sqrt{C_{\Sigma,n}C_{\Sigma,m}}}\sqrt{\omega_{q,n}\omega_{q,m}}$. The readout resonators are designed as lumped LC circuits with a capacitance of $Cr = 300$ fF. With the 2 GHz qubit-resonator detuning, we predict a readout dispersive shift of 1.75 MHz with qubit resonator coupling $g = 170$ MHz as in Eq. 2.53, and a corresponding coupling capacitance of 10 fF.

We calculated the spectrum of the system and the strength of the parametric interaction using the scQubits and Qutips packages in Python. The calculated spectrum is shown in Fig. 6.5. The SQUID in our design not only allows the parametric process but can also be tuned to change the system's spectrum, particularly qubit 2. The simulation plots show the energy transitions moving as the flux bias, ϕ_b, changes. Qubit 2 shows a large tuning range, being the qubit with the SQUID. Some higher energy transitions also reflect the tunability of qubit 2. For example, the three-body transition $|001\rangle \rightarrow |110\rangle$ is evidently sensitive to flux bias, understandable, taking into account that its estimated transition frequency $\omega_{3q} = \omega_{01}^{q1} + \omega_{01}^{q2} - \omega_{01}^{q3}$, ignoring the cross-Kerr effect. Patterns of other three-body transitions can be understood in a similar way. The tuning of the spectrum can also affect the strength of the qubit-qubit coupling, as indicated by the cross-Kerr factors, χ_{ij}, which show changes as a function of flux bias. Specifically, χ_{12} decreases while χ_{23} increases as qubit 2 is tuned away from qubit 1 and closer to qubit 3, which can affect the strength of the three-body interaction.

The three-body strength is affected by flux bias in two ways. First, the three-body interaction is realized through the sine term of the SQUID energy, which has a prefactor $\cos(\phi_b)$. Second, the change in qubit-qubit couplings inferred from the cross-Kerr terms, as seen in Fig. 6.5(b), will also have an effect on the three-body strength since the parametric terms in Eq. 6.32 involves an average of qubit couplings to the SQUID mode.

Finally, we analyze the strength of three-body interaction for the different possible permutations in Fig. 6.6 In panel (b), we clearly see the resonance frequencies shift as the parametric pump strength increases, which tunes in a consistent direction with the qubit 2 frequency in the spectrum plot, depending on whether the contribution of qubit 2 to ω_{3q} is positive or negative. This indicates that the parametric modulation also affects the SQUID's cosine term, resulting in effective flux biasing. On the basis of the calculation results, we believe the interaction is achievable with a reasonable pump strength.

HFSS simulation

We simulate the whole chip using the finite-element-model software known as HFSS. The aluminum film is modeled as a perfect conductor, and the qubit junctions are modeled as

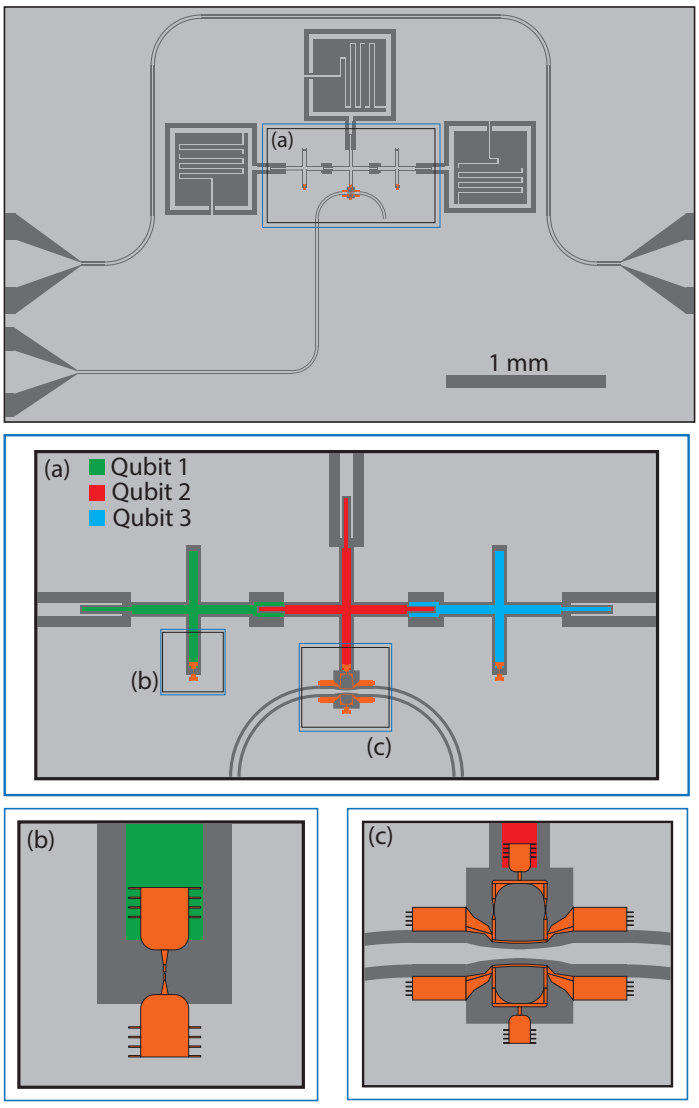

Figure 6.4: CAD drawing of three-qubit device. (a) Three transmon qubits in Xmon shape are capacitively coupled. (b) The qubit junction (orange) shunts the bottom finger to the ground. (c) The SQUID of the middle qubit is inductively coupled to the pump line.

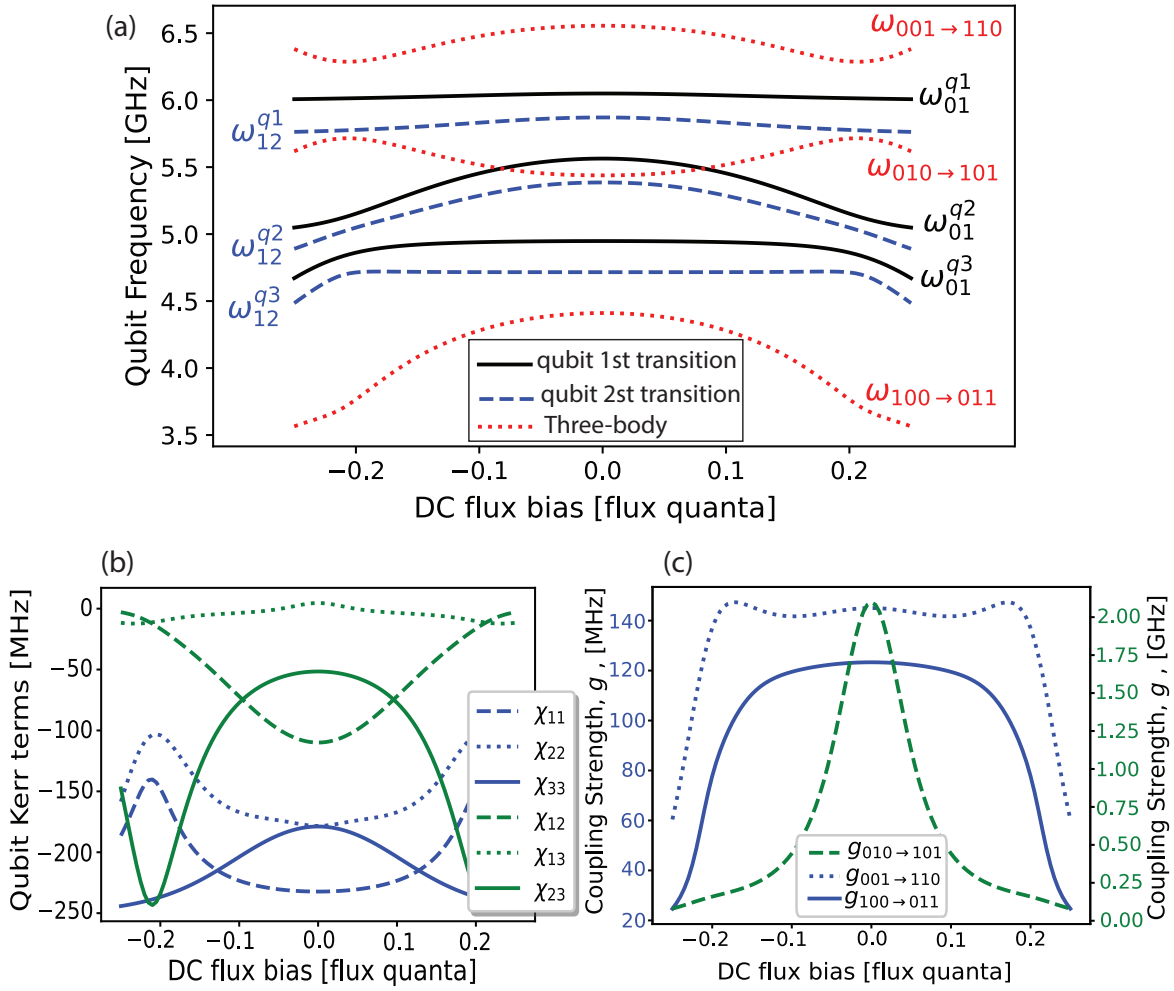

Figure 6.5: The simulation of capacitively coupled three-qubit design. (a) Shows the first two transitions of each qubit as a function of flux bias, with qubit 2 being strongly tunable due to the presence of the SQUID. The resonance frequencies of the three-body transitions are also plotted in red. (b) and (c) demonstrate the effect of flux bias on the important system properties. In (b) shows the qubit self-Kerr, χ_{ii}, (anharmonicities), as a function of flux bias. (c) shows the pre-factor of the three-body terms without considering the pump signal strength.

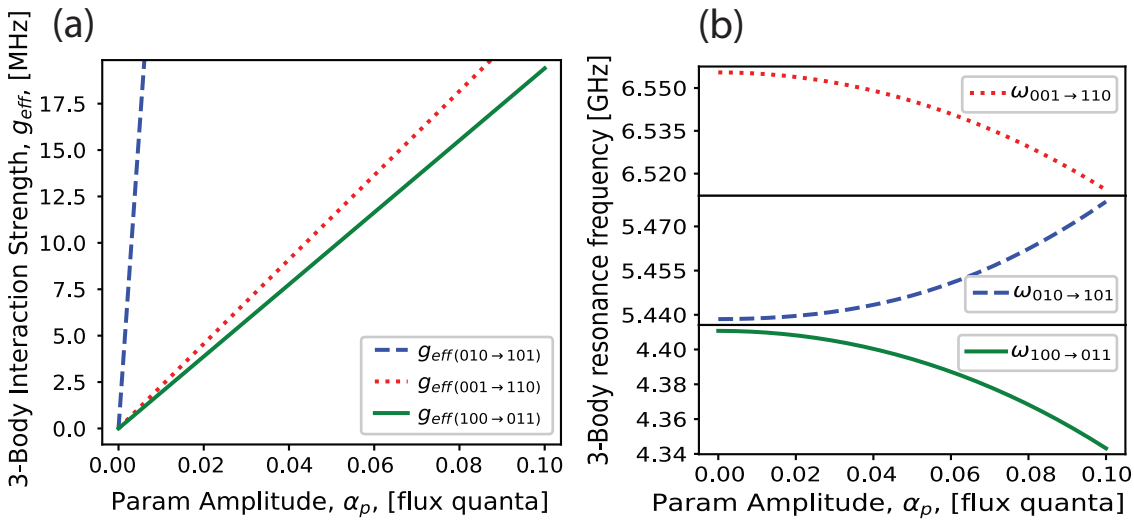

Figure 6.6: Three-qubit interaction strength and resonance. Calculations to first-order in perturbation theory at zero flux bias are shown in (a) and (b), which describe the strength and three-body resonance, ω_{3q}, of the interaction as a function of pump signal amplitude, respectively.

lumped-element linear conductors. Each qubit is assigned a lumped port in parallel to the qubit node. The zeros of the input impedance seen by the port represent the resonances of the chip. This allows us to estimate the capacitances of the physical layout of the qubit and resonator design, as well as to estimate the coupling strengths. We sweep the middle qubit frequency across the other two qubits to estimate the coupling strength as half of the splitting due to the avoided crossings as shown in Fig. 6.7

6.5 Experiment

6.5.1 Experimental Setup

Fridge Setup

The device is cooled using a cryogenic-free dilution refrigerator that can reach a temperature of approximately 7 mK. The interior structure of the fridge consists of five different stages, starting from the 50K stage all the way down to the 10 mK stage, the mixing chamber (MC), where the device is mounted.

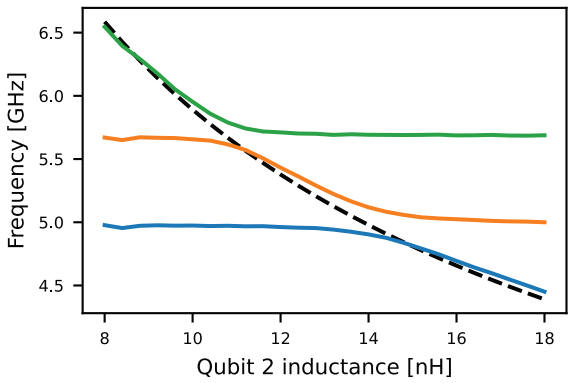

Figure 6.7: HFSS simulation of three-qubit device. The black line represents the bare frequency of qubit 2. We observe two avoided crossings as the qubit passes qubit 1 and qubit 3. The avoided crossing gap is equivalent to twice the coupling strength, g.

In addition to cooling the device down, we need a proper wiring setup between the device ports and the room temperature instrument to control the qubits and readout the quantum state of the device, as shown in Fig. 6.8 . The wiring setup includes three microwave lines with 50-ohm SMA cables for input, control, and output signals, as well as a DC line terminated by a coil for external flux bias.

Although the input signal at the device port needs to be at the few-photon level, the high thermal noise at room temperature impedes us from achieving a good SNR. Instead, the input signal at the fridge input is often set roughly from -20 to -40 dBm. Then, the fridge input line is heavily attenuated along the different stages for proper cooling of the input signal to maintain good SNR. In addition to a cryogenic low-pass filter, we will use an in-house carbon nanotube-based lossy transmission line filter (CNT) designed to block thermal radiation higher than 50 GHz.

However, the weak signal of the device output needs to be amplified before it is washed away by thermal noise. We use a low-noise amplifier at the 3K stage, namely a high electron mobility transistor (HEMT) amplifier, to enhance the signal before it reaches the fridge output for further amplification. Also, the device output port is isolated from thermal noise using circulators at the MC stage, where any noise coming from the output line/ HEMT is shunted to a 50 OHM terminated port, thermally anchored to the MC plate.

We use an external coil mounted on the sample box to apply a DC flux bias on the device via fridge DC lines. In addition, the device has an on-chip fast-flux line used for parametric control, which we connect to through the pump line. The pump is treated as

the input line we discussed, heavily attenuated with a low-pass filter.

Control and measurement Setup

We use digital-to-analog converters (DAC)s to generate the qubit control pulses. The pulse wave is synthesized digitally at an IF frequency $f_{IF} = 150$ MHz via a sampling rate of 1.2 Gsps. We use an upconversion circuit to upconvert the pulse to the RF range with a local oscillator at around $f_{LO} = 5$ GHz. Since the upconversion process typically results in two sidebands in the RF range at $f_{LO} \pm f_{IF}$, we use an IQ mixer to implement single-side-band mixing. Channel 2 of the DAC is used to generate an out-of-phase pulse to be fed to the Quadrature port of the IQ mixer, which will destructively interfere with the in-phase pulse on one sideband, $f_{LO} - f_{IF}$, but constructively interfere on the other, $f_{LO} + f_{IF}$. Keep in mind that the perfect phase calibration does not necessarily happen at 90° as the length of the paths for both signals is not perfect and not equal. Additionally, LO leakage to the IQ mixer output is a common issue that can be suppressed by tuning the dc offsets of mixer inputs.

We inject three readout pulses to detect the resonator responses simultaneously. The circuit involves three continuous-wave (CW) sources combined and connected to the input port of a microwave switch. While the normally-closed (NC) output port is terminated by a 50 ohm, the normally-opened (NO) output port is connected to the fridge input. The readout pulses are generated at the NO port by feeding a square pulse to the switch trigger port using an arbitrary function generator (AFG). In other words, the square pulse will act as an envelope to the CW signals.

The parametric pulse we apply through the pump line is generated using an Aeroflex 3025C RF digital arbitrary wave generator (AWG) with integrated dual-channel; the single-side-band mixing is calibrated onboard from the manufacturer. Since the AWG has an output range of only up to 6 GHz, we employ an upconversion circuit to reach a higher frequency with filtering at the output to eliminate sidebands and LO leakages.

Finally, the fridge output is filtered within the range of readout frequencies and down-converted to a range of 2 GHz before it is split into three Aeroflex 3025C heterodyne analog-to-digital converters (ADC)s called RF digitizers (ADC)s. In the digitization process, the incoming signal is downconverted to an IF before it is sampled at 250MHz. This process preserves the information from both quadratures, which are then produced digitally by the FPGA.

Those instruments and pulses have to be synchronized together using a proper triggering scheme. All of the Aeroflex instruments are modules mounted on a NI PXI-1045 chassis

with trigger routing modules on the chassis backplane. This allows us to route the AWG trigger signal to all ADC modules. Mounted on the same chassis, we used a NI PXI-6651 Timing module to synchronize standalone instruments with AWG trigger. It allows us to generate additional synchronized trigger signals at two output ports, which are connected through external cables to the AFG and DAC trigger inputs.

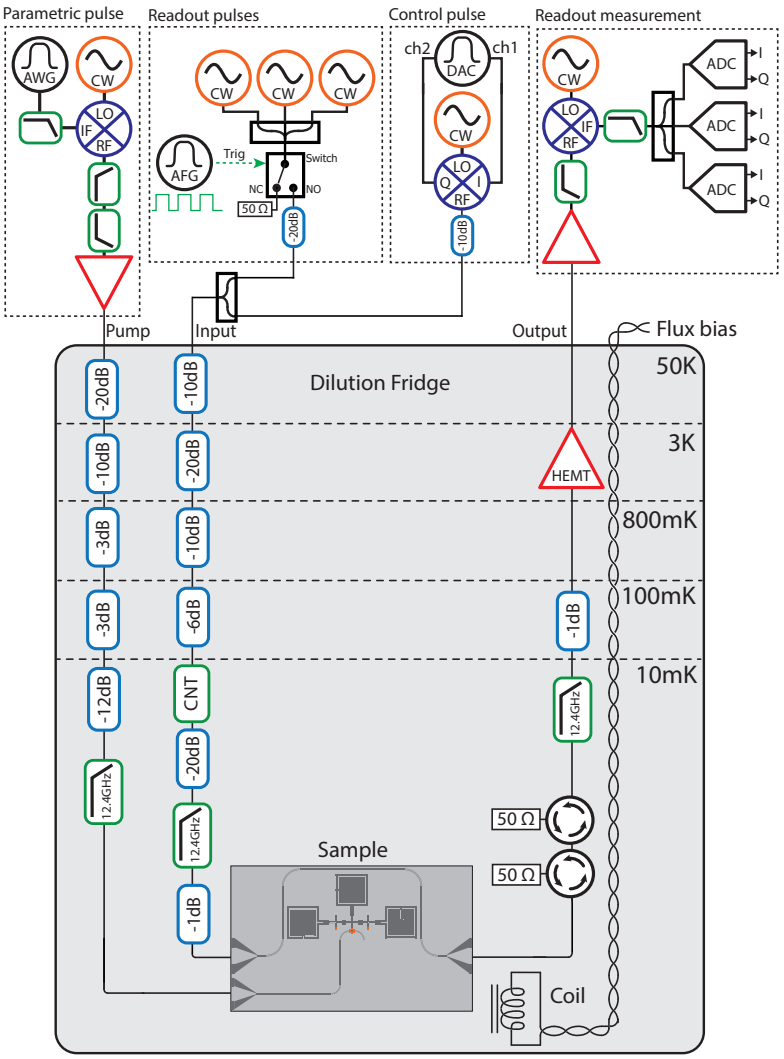

Figure 6.8: three-qubit Experiment Setup.

Readout resonator	**1**	2	3
Resonance frequency [GHz]	7.698	7.518	7.035
Internal decay rate, κ_{int}, [MHz]	0.439	0.489	5.1
External decay rate, κ_{ext}, [MHz]	0.211	0.154	1.27
Coupling efficiency, η.	0.325	0.240	0.199

Table 6.1: The table shows all the resonator parameters extracted from VNA measurements, including resonance frequencies, internal and external decay rates

6.5.2 Device Characterization

Spectroscopy Measurements

We first identify the resonators in our device using VNA measurements of the resonators. The resonators are capacitively coupled to a two-port (through) transmission line. Using a VNA, we measure S_{21} at low power across a wide range of frequency. The typical resonator response in magnitude and phase helps identify any resonances in the system. Usually, the system will have several stray resonances, which we rule out by performing a Punchout experiment. In the Punchout experiment, we detect the resonators' nonlinearity due to coupling to qubits. This manifests as a sudden shift in the resonator frequency as the VNA probe power is increased. The measured parameters of the readout resonators are listed in table 6.1. We note that resonator 3 was far off from design with a very large internal decay rate,κ_{int}, which will pose challenges on the qubit state readout.

Then, we use spectroscopy to find the qubits. We continuously measure the resonators S_{21} using the VNA while applying an additional strong microwave signal which is stepped over a wide frequency range to search for qubit frequencies. When the search signal hits a qubit frequency, it excites the qubit into a mixed state, causing a change in the resonators' response due to the qubit-resonator dispersive coupling.

Resolving some of the higher-order transitions in our complex system is essential to realize the three-body interaction and characterize the qubit anharmonicities. Here, we use two-tone spectroscopy. In addition to the resonator probe and first spectroscopy tone fixed at the resonant frequency of one of the qubits, we apply a second spectroscopy tone which is again stepped over a wide range in frequency. In other words, the system is prepared in mixture that contains one of the single qubit states $|10\rangle$ previously identified, while the search tone scans for the next transition to either the qubit second state $|20\rangle$ or the qubit-qubit excited state $|11\rangle$. The transition to the qubit second state gives us the self-Kerr strength proportional to its anharmonicity, while the qubit-qubit transition yields

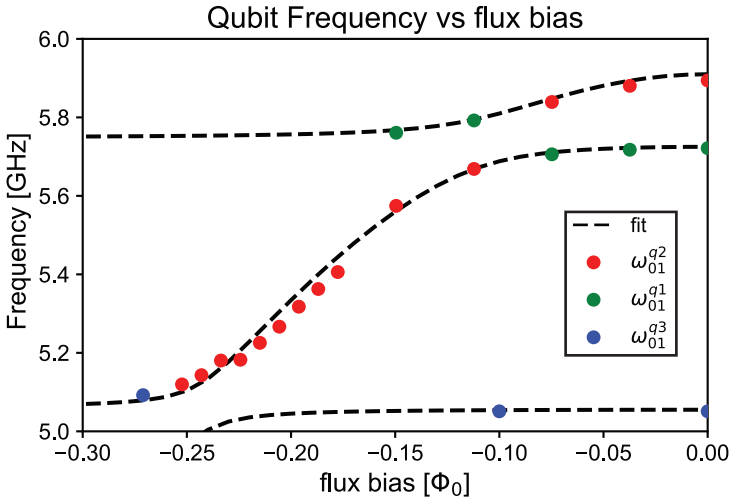

Figure 6.9: The measured three-qubit spectrum and fit. The dots represent the measured qubit frequencies as a function of flux bias and theory fit (dotted).

the cross-Kerr couplings.

Spectrum as a function of the flux bias

Here we measure the qubit frequencies as a function of the flux bias, ϕ_b. The tunability of the qubit was found to be very large, spanning a range of more than 800 MHz. Following the tuning curve, the qubit 2 frequency shifts down as a function of flux bias, crosses the first qubit, and gets very close to the lowest qubit frequency, allowing us to observe avoided crossings. We show in Fig. 6.9 the measured spectrum along with the fit using our design model, which gives us information about the qubit-qubit couplings and qubit frequencies as functions of external flux.

Qubit	1	2	3
ω_{01}^{q} [GHz]	5.731	5.888	5.0935
Qubit capacitance, C_n [fF]	82	116	116
Qubits n and m	12	13	23
Coupling capacitance, C_{nm} [fF]	2.464	5.274	1.605

Table 6.2: The extracted 3Qubit parameters by fitting the spectrum vs flux bias

Qubit calibration and characterization

We now move on to the characterization and calibration of qubits and their control pulses. To do that, we need to perform pulsed measurements. The measurements start with initializing the system in an initial state, then either allowing the system to evolve or applying a number of control pulses on qubits. Finally, the system state is measured by applying readout pulses on the readout resonators.

First, the qubit frequency and π-pulse calibration are performed via the Rabi experiment repeated for a varying pulse frequency. We apply a Gaussian control pulse on the qubit to excite it to an arbitrary superposition state of $|0\rangle$ and $|1\rangle$. The control pulse width is gradually increased to change the superposition amplitudes of the qubit state, analogous to rotating the qubit on the Bloch sphere. Therefore, we observe the decaying Rabi oscillations of the qubit coherent population which vanishes as the qubit state becomes a statistically mixed state. We repeat this measurement by varying the control pulse frequency around the qubit frequency identified earlier in spectroscopy. Based on standard theoretical expectations, we identify the qubit frequency as the one with the slowest Rabi oscillation. With the Rabi data, we can also calibrate the standard π-pulse and $\pi/2$-pulse widths required to excite the qubit to state $|1\rangle$.

A more accurate calibration of qubit frequency is then done using a Ramsey experiment. First, a $\pi/2$-pulse is applied to initialize the qubit in an equal superposition state $|0\rangle + |1\rangle$, setting the qubit at the equator of the Bloch sphere. Then, the qubit state is allowed to evolve freely for a time t before a second $\pi/2$-pulse is applied to rotate the state back to the $\{|0\rangle, |1\rangle\}$ basis. Finally, we readout the qubit state, projecting onto the $\{|0\rangle, |1\rangle\}$ basis. In general, plotting, e.g. the excited state population versus t shows decaying oscillations. The oscillation frequency indicates the detuning from the actual qubit frequency. We repeat this measurement with the updated qubit frequency until the oscillation vanishes, resulting in a simple exponential decay curve. The time constant of this decay is known as T_{Ramsey} (or T_2^* in standard NMR notation).

With the qubit frequency calibrated, we can complete the characterization by measuring T_1 and T_{Echo}. The energy relaxation time, T_1, is measured by initializing the qubit in the ground state, applying a π pulse, then measuring the probability of finding the qubit in the excited state over time. T_1 characterizes the loss of energy by the qubit to the environment. T_{Ramsey} and T_{Echo}, on the other hand, describe the decay of coherence in the qubit. T_{Ramsey} includes contributions from both energy relaxation and pure dephasing, $1/T_{Ramsey} = 1/2T_1 + 1/T_\phi$ [80]. The measurement of T_{Echo}, on the other hand, involves the application of a refocusing "echo" π-pulse at the midpoint of the waiting time. The effect of the refocusing pulse is to cancel the effects of low-frequency dephasing. In the best case,

	Qubit 1	Qubit 2	Qubit 3
Qubit frequency [GHz]	5.725	5.910	5.055
Qubit Anharmonicity [MHz]	-184	-105	-156
Lifetime, T_1, [ns]	1302	4216	7313
Ramsey decay time,T_{Ramsey}, [ns]	971	2470	2907
Echo decay time, T_{Echo}, [ns]	965	-	4527
Dispersive shift on R1, $2\chi^{r1}_{100}$, [MHz]	-7.3	-0.4	0
Dispersive shift on R2, $2\chi^{r2}_{010}$ [MHz]	-2.2	-2.4	0
Dispersive shift on R3, $2\chi^{r3}_{001}$ [MHz]	-2	-3	-0.5

Table 6.3: The table shows all the parameters extracted during the three-qubit characterization, including qubit frequencies, anharmonicities, lifetimes, and dispersive shifts of resonator frequencies.

T_{Echo} can approach the homogeneous limit of $T_{Echo} = 2T_1$.

6.6 Validation of the $|110\rangle$ state

The simulation of LGTs requires finding the qubits' lowest states as well as an additional higher state, namely $|110\rangle$, in the model we aim to simulate. Due to the strong cross-Kerr couplings and proximity of qubits 1 and 2, estimating $|110\rangle$ as $\omega_{01}^{q_1} + \omega_{01}^{q_2}$ is insufficient. We show in Figure 6.10 that this is true; not only the transition frequency is shifted due to cross-Kerr coupling, but also two other two-photon transitions exist very close to the target state, namely $|200\rangle$ and $|020\rangle$.

To distinguish the state $|110\rangle$ transition from other states, we climb the energy ladder to the $|110\rangle$ via two consecutive single-photon transitions. First, we calibrate the amplitude of a control pulse to ensure it is weak enough not to excite higher transitions during a Rabi experiment. Starting in the ground state, we sweep the pulse frequency in the expected range where the target transition occurs to ensure that no undesired transitions exist in that range. Then, we search for the target state by preparing the system in the $|010\rangle$ or $|100\rangle$ states, then perform a second 2D Rabi-style experiment in the same frequency range. When the pulse frequency is in resonance with a single-photon transition, we observe the Rabi oscillations between the one-excitation state and the two-excitation state. The experiment is done twice by climbing the ladder via the two possible paths through $|100\rangle$ or $|010\rangle$. Since the transitions $|100\rangle \rightarrow |020\rangle$ and $|010\rangle \rightarrow |200\rangle$ are higher-order processes involving the annihilation of a photon in one qubit and the creation of two photons in

another, they are strongly suppressed under typical driving conditions. In addition, each path connects to two states via a single-photon transition. i.e, $|100\rangle \rightarrow |200\rangle, |110\rangle$ and $|010\rangle \rightarrow |020\rangle, |110\rangle$. Hence, this allows us to determine the target state $|110\rangle$ since it is the only state accessible via single-photon transitions through both paths. Finally, we probe the two-excitation states identified earlier via two-photon transitions by driving at half the transition frequencies starting from the ground state, i.e., $|000\rangle \rightarrow |200\rangle, |020\rangle, |110\rangle$.

We further provide additional confirmation of the identified states $|200\rangle, |110\rangle, |020\rangle$ by means of setting bounds based on the values of the lower energy levels. According to the transmon qubit design, the higher energy levels are expected to be shifted down since it is characterized by a negative self-Kerr. In other words, the transition frequency to the second energy level of a transmon, $E_{|200\rangle}$, is smaller than twice the transition frequency to the first energy level, $E_{|100\rangle}$; i.e., $E_{|200\rangle} < 2E_{|100\rangle}$. Also, the static qubit-qubit coupling results in negative cross-Kerr, i.e., $E_{|110\rangle} < E_{|100\rangle} + E_{|010\rangle}$. This allows us to define a range where we expect to find the energy level $E_{|110\rangle}$, highlighted in green in Fig. 6.10. Since we only observed the $|110\rangle$ state, identified in the previous process, within those bounds, this gives us high confidence it is the target state.

6.6.1 Characterizing the dispersive shifts of quantum states

In our complex system, it is crucial to characterize the resonator's dispersive shifts to identify the system state as it evolves. Not only do we need to characterize the shift of the intended resonator-qubit pairs but also the unwanted coupling of all possible pairs. We find that the unwanted shifts are too strong to mitigate in single-frequency readouts when we expect the system to be in an arbitrary state. For this reason, we plot the state-dependent dispersive shifts in a 2D plane where each axis represent a shift on resonator 1 and 2 to allow us to distinguish the first two-qubit states as shown in Fig. 6.11. Since resonator 3 has a large decay rate, couples to all qubits, and exhibits only small dispersive shifts, we leave it to the last step to infer only qubit-3.

6.6.2 Three-Body interaction

Now that we characterized the system, we proceed to the primary goal of this work: realizing the three-body interaction. First, we initialize the system in the state $|001\rangle$ by applying a π pulse on qubit 3. Second, we activate the interaction for time t by applying the parametric pulse with appropriate width on the SQUID loop at, ω_{3q}, corresponding to the energy difference between the initial state and the target state $|110\rangle$. Finally, we apply three

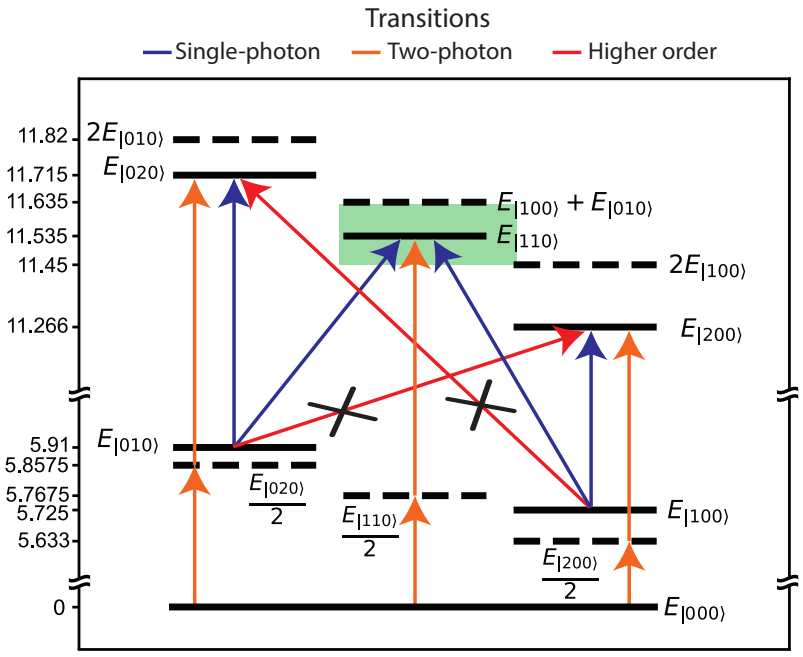

Figure 6.10: Validation of $|110\rangle$ state. Depiction of the measured energy levels and the process used to determine the $|110\rangle$ state. The plot shows two possible paths to $|110\rangle$ by preparing the system at $|010\rangle$ or $|100\rangle$ state. (We use low-amplitude control pulses to suppress multiphoton transitions.) Although the two-excitation states $|020\rangle$ or $|200\rangle$ can be accessed via single-photon transitions via one of the paths, the only state accessible via single-photon transition in both paths is the state $|110\rangle$. The dashed lines depict the two-excitation energy levels in the absence of cross-Kerr couplings. With negative cross-Kerr, those energy levels shift down, i.e., $E_{|020\rangle} < 2E_{|010\rangle}$, $E_{|200\rangle} < 2E_{|100\rangle}$ and $E_{|110\rangle} < E_{|100\rangle} + E_{|010\rangle}$ which sets bounds defined by the lowest energy levels. We define a region of interest (green), bounded at the bottom by $2E_{|100\rangle}$ and the top by $E_{|100\rangle} + E_{|010\rangle}$, where we can only expect state $|110\rangle$ to be observed. After states identification, we use a stronger drive at half the transition frequency to drive the two-excitation states via a two-photon process (orange)

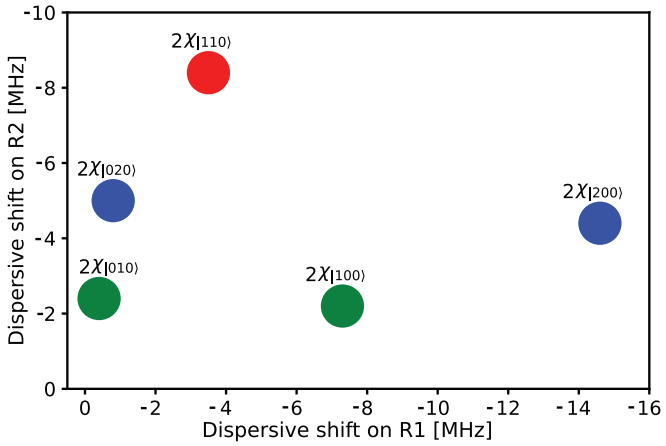

Figure 6.11: The state-dependent resonator shifts in the 2D dispersive plane. We character the dispersive shifts of the one and two-excitation states. Depicts of the characterized state-dependent where horizontal and vertical axes represent resonator 1 and resonator 2 shifts, respectively.

simultaneous readout pulses to measure the system state. In Fig. 6.12, we produce the 2D Rabi-like chevrons by repeating the experiment while varying the parametric pulse time and frequency.

We control how strong the interaction is by increasing the parametric pulse amplitude. We show in Fig. 6.12 that we can achieve up to 7 MHz strength. In other words, we can drive the system to reach the final state in as short a time as 70 ns. The difficulty in our system remains that ω_{3q} starts shifting down as we increase the pulse amplitude. This happens because the strong modulation of the SQUID energy results, on average, in an effective dc flux bias, which causes the system spectrum to shift, especially for qubit 2. As a result, the energy difference between the target state and the initial state decreases. We observe this experimentally and can fit the results using the three-qubit model with parameters from the spectrum fit, as shown in Fig. 6.12

Although within the same order of magnitude, the model predicts a linear increase in strength, whereas the experimental data shows a nonlinear trend at slightly higher strength. One possible explanation is that with a strong pulse, we can be activating other high-order transitions close in frequency to the current parametric frequency. Especially when the frequency is changed as we increase the pulse amplitude, the strength and the stray transitions activated are varied, resulting in a nontrivial trend. Although this does

not undermine the significance of the three-body interaction we achieved, it highlights the need for a better understanding of the model or an alternative three-qubit design that is less disturbed by the strength of the pulse amplitude.

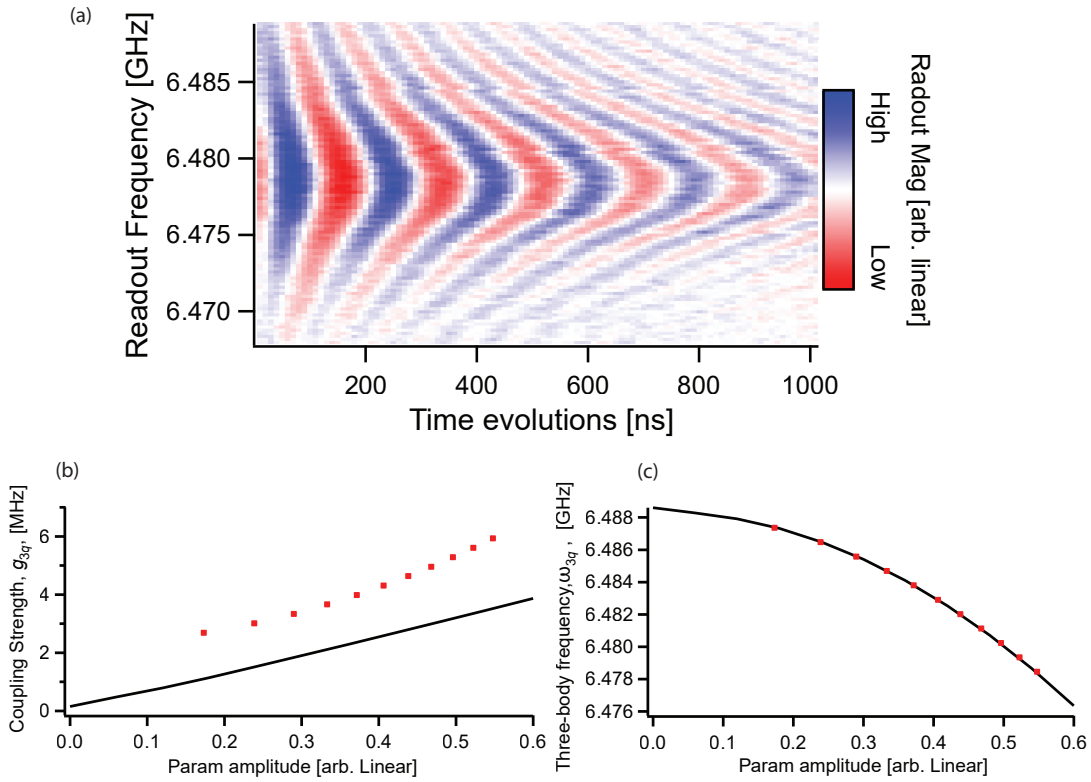

Figure 6.12: Achieving the three-body interaction. (a) 2D Rabi chevron of three-body interaction as we measure the $|110\rangle$ state by readout at resonator 2. The extracted strength (b) and resonance frequency, ω_{3q}, (c) as a function of parametric pulse amplitude are plotted in red markers (red markers) and the first-order perturbation is calculated using model parameters from spectrum fit (black)

Inferring the system state

After realizing the target interaction, we further confirm it by inspecting the characterized state-depedent dispersive shifts. However, the complicated family of dispersive shifts in our system prevents us from making a direct inference. In the following, we describe the inference process starting with a theoretical background.

Dispersive coupling allows us to detect the state of the qubits by measuring the response of the resonator to a readout pulse. The resonator field can reach steady state, that is, $\dot{a} = 0$, with a sufficiently long readout pulse. i.e., $t > \kappa$, where κ is the total decay rate of the resonator. Furthermore, the output mode quadratures are related to the resonator quadratures by the input-output theorem. Thus, we can infer the qubit states by measuring the averaged state-dependent resonator quadratures [81]. The averaged state-dependent field amplitude, α_σ, can be written as

$$\alpha_\sigma(\omega_d) = -\frac{(\kappa/2)}{\sqrt{(\kappa/2)^2 + (\omega_r - \omega_d + 2\chi_\sigma)^2}} \tag{6.34}$$

where ω_d is readout frequency, σ is an eigenstate of the system, and $2\chi_\sigma$ is the resonator's state-dependent dispersive shift. Furthermore, the measurement operator can be constructed as [81]

$$\hat{M}(\omega_d) = \sum_\sigma \alpha_\sigma(\omega_d) \left|\sigma\right\rangle \left\langle\sigma\right| . \tag{6.35}$$

The expectation value of the measured field amplitude is then $\alpha(\omega_d, t) = Tr[\hat{\rho}(t)\hat{M}(\omega_d)]$. The density operator $\hat{\rho}(t)$ in time is $\hat{\rho}(t) = \sum_{\sigma\sigma'} P_{\sigma\sigma'}(t) \left|\sigma\right\rangle \left\langle\sigma'\right|$ where $\sigma = \{000, 001, 010, 100, 011, 101, 110\}$. Since $\hat{M}$ is diagonal in the eigenstates basis, we arrive at the simple final expression of interest:

$$\alpha(\omega_d, t) = \sum_\sigma P_{\sigma\sigma'}(t)\alpha_\sigma(\omega_d). \tag{6.36}$$

The field amplitudes travel through the measurement lines to be amplified. Therefore, the measured signals, $\tilde{\alpha}(\omega_d, t)$, at the digitizers represent the field amplitudes with an arbitrary scale, G, and the addition of noise, μ, i.e., $\tilde{\alpha}(\omega_d, t) = G\alpha(\omega_d, t) + \mu$. We extract the normalization parameters by measuring the field amplitude in a known state, the ground state, $P_{000}(t) = 1$, such that what we measure reduces to

$$\tilde{\alpha}(\omega_d, t) = -G\frac{(\kappa/2)}{\sqrt{(\kappa/2)^2 + (\omega_r - \omega_d)^2}} + \mu. \tag{6.37}$$

Moving forward, all measured amplitudes are normalized so that we are directly observing Eq. 6.36.

We use the 2D dispersive plane to extract the system states as it evolves over time. In Fig. 6.13, the system is initialized at the state $|001\rangle$, which corresponds to qubits 1 and 2 being in the ground state and qubit 3 being excited. The system then evolves to the state $|110\rangle$ and continues oscillating back and forth between these states. The difference between dispersive shifts is larger than the resonator linewidths, $|\chi_{11} - \chi_\sigma| > \kappa/2$, which

simplifies the state-distinction process. That means we can choose $\tilde{\omega}_d = \omega_r + 2\chi_{110}$ such that all $\alpha_\sigma(\tilde{\omega}_d) \approx 0$, and only $\alpha_{110}(\tilde{\omega}_d) \approx -1$, which reduces the expectation values of the measured field amplitude 6.36 to

$$|\alpha(\omega_d, t)| = P_{|110\rangle}(t), \tag{6.38}$$

Which directly measures the population of the state $|110\rangle$ as shown in Fig. 6.13(d). We fit the data to a decaying-oscillating probability $P_\sigma(t) = a_\sigma(1 - \cos(\omega_g t + \phi_\sigma))e^{-t/T_d}$, where a_σ oscillation amplitude, ϕ_σ determines the initial state population, T_d is decay time, and ω_g is the oscillation frequency.

It is important to point out that the low population of $|110\rangle$ can be partially attributed to our simplified assumptions. In our analysis, we assume that the average of the readout pulse amplitude over the pulse time corresponds to the magnitude of the resonator field in the steady state, and that the qubits have an infinite lifetime. However, our readout pulse time is comparable to qubits' lifetimes. For such a case, we would need to fit the whole dynamics of the dispersive resonators to reach a more accurate estimate of the state population [82]. Further, due to the strong ZZ interaction, and in the presence of thermal noise, we suffered from low fidelity single qubit gates which resulted in the initial low population of qubit 3, $P_{|001\rangle}(0) \approx 0.6$

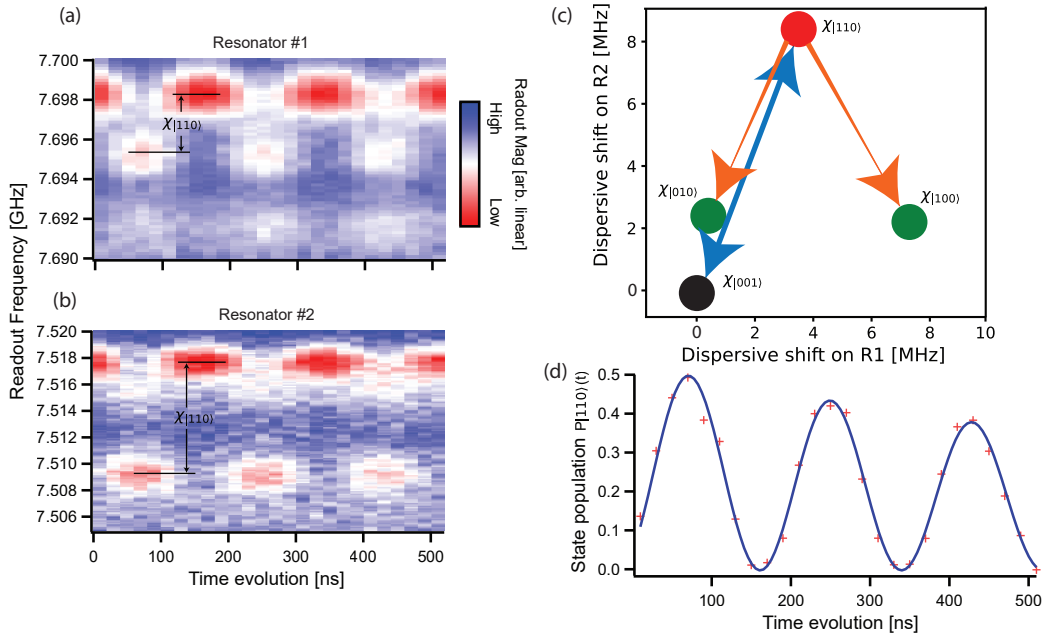

Figure 6.13: Analyzing the System State using the 2D Dispersive Plane. On the left, the averaged measured field amplitudes of resonators 1 (a) and resonator 2 (b) as a function of readout frequency, ω_d. The observed "blobs" indicate minimum peaks of the field amplitudes, corresponding to the states with respective χ_σ evolving in time. The 2D coordinate of these "blops" is determined by the shifts on both resonators. In (c), we can identify the main interaction as the oscillation between the state $|110\rangle$ (in red) and$|001\rangle$ (in black), in addition to the decay to lower qubit states $|100\rangle$ and $|010\rangle$. In (d), we can extract the population of state $|110\rangle$ by taking the line cut of resonator 2 amplitude at $\tilde{\omega}_d = \omega_r + 2\chi_{110}$.

Fitting resonator 3 to extract qubit 3 state

Although resonator 3 was designed to be mainly coupled to qubit 3, the fabricated device shows considerable issues with this readout resonator. First, it couples poorly to qubit 3. Next, it couples much more strongly than expected to qubits 1 and 2. This may be due to the small resonator-qubit detuning with those qubits compared to qubit 3 (about 800 MHz smaller). In addition, the resonator linewidth, $\kappa^{r3} = 6.37$MHz, is larger than all single-photon dispersive shifts, $\kappa^{r3} > \chi^{r3}_{001}, \chi^{r3}_{100}, \chi^{r3}_{010}$, leading to substantial overlaps between all states.

Nevertheless, since we now know $P_{110}(t)$, including some of the interaction parameters,

such as ω_g and T_d, we are still able to extract the qubit 3 state by fitting the resonator 3 measurements. The goal is to fit the resonator 3 field amplitudes to Eq 6.36. Therefore, we measure and normalize the state-dependent field amplitudes of resonator 3, $\alpha_\sigma^{r3}(\omega_d)$, for the expected states to be involved in the dynamics, $\sigma = \{000, 001, 010, 100, 110\}$ shown in Fig. 6.13(c). While we assume a decaying sinusoidal $P_{001}(t) = a_{001}(1-\cos(\omega_g t + \phi_{001}))e^{-t/T_d}$, the decay probabilities to lower energy levels, P_{010} and P_{100}, are assumed to have constant probabilities in the timescale, we are fitting. Finally, using Eq. 6.36, we fit the 2D measurement of averaged field amplitude $\alpha^{r3}(\omega_d, t)$ as seen in Fig in 6.14. Based on the fits in Fig. 6.14 and Fig. 6.13, we can infer with high confidence that we have implemented the desired three-body interaction which drives the oscillations between the states $|001\rangle$ and $|110\rangle$.

Other permutations of the three-body interaction are also possible, as mentioned in the design section, such as $|010\rangle \rightarrow |101\rangle$ and $|100\rangle \rightarrow |011\rangle$. We have experimentally tried the permutation $|010\rangle \rightarrow |101\rangle$; however, we have not conducted additional experiments, such as those in the validation of $|110\rangle$ section, to confirm it.

Alternative design

Based on the detailed measurements and issues presented, we have also investigated an alternative design in an attempt to overcome a few challenges. The tunability of qubit 2 results in a significant change in the coupling strength between the qubits when the parametric drive amplitude is increased. Additionally, the three-body frequency, ω_{3q}, drifts as observed in Fig. 6.6(b). In light of these issues, we have considered an alternative approach to mitigate these challenges.

The proposed design involves three qubits that share a SQUID, which acts as additional inductance to the qubits and also weakly couples their current to enable parametrically activated interactions. We use qubit parameters similar to those of the previous design, with qubit frequencies of $4.5 - 6$ GHz, initial anharmonicities around 250MHz, and a shunting capacitance of 70fF.

The simulation starts with a very small inductance and then gradually increases, as shown in Fig. 6.16. In panel (b), we observe a downward shift in qubit frequencies as their total inductance increases. However, panel (a) reveals that the three-body coupling strength is also increasing - while the SQUID inductance results in reduced qubit anharmonicity, it increases coupling to other qubits. After careful consideration, we chose a SQUID inductance of 0.5 nH, which provides a reasonable coupling strength without compromising qubit anharmonicities or increasing cross-Kerr terms.

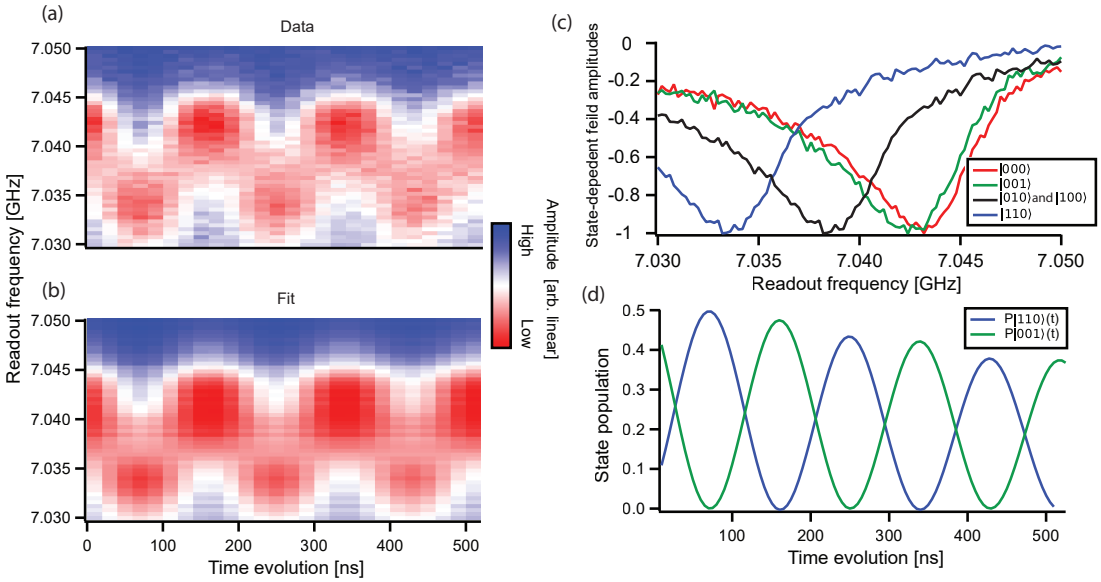

Figure 6.14: Extracting qubit 3 state. (a) measured (b) and fit (bottom) of reading out the interaction at resonator 3 while sweeping the readout frequency. (c) The state-dependent field amplitude of resonator 3 for different states. Taking the extracted information about the state $|11\rangle$ population, $P_{110}(t)$, we fit the 2D data in (a). The fit further confirms that the system is oscillating between the initial state and the target state as expected by the three-body interaction

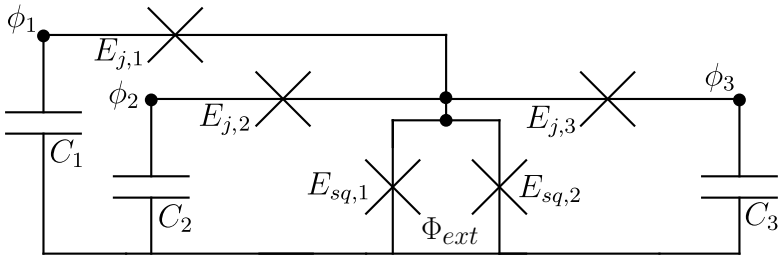

Figure 6.15: The circuit of an alternative design of three-qubit device. The SQUID inductance is shared among all three qubits.

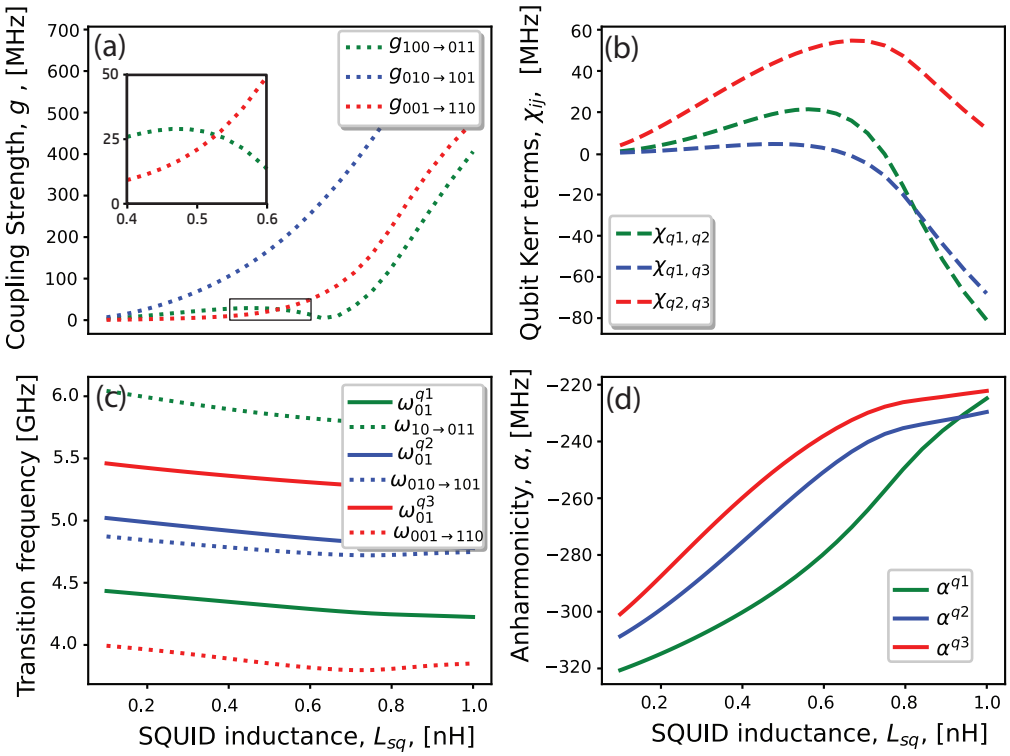

Figure 6.16: The simulation of an alternative design of the three-qubit device as a function of shared SQUID inductance

We examine the effect of DC biasing the SQUID in Fig. 6.17 on qubit frequencies and other parameters. Basing the SQUID results in larger inductance, leading to stronger coupling between the qubits, as is evident in panels (a) and (b). In (c), we observe the qubit frequencies shifts in the same direction with a tuning range of about 250 MHz, implying that the couplings are less sensitive to the flux bias. Therefore, we will operate the SQUID at zero DC flux bias since the design inductance is achieved in the fabrication process. However, if the coupling strengths are found to be weak, we can easily tune them to higher values.

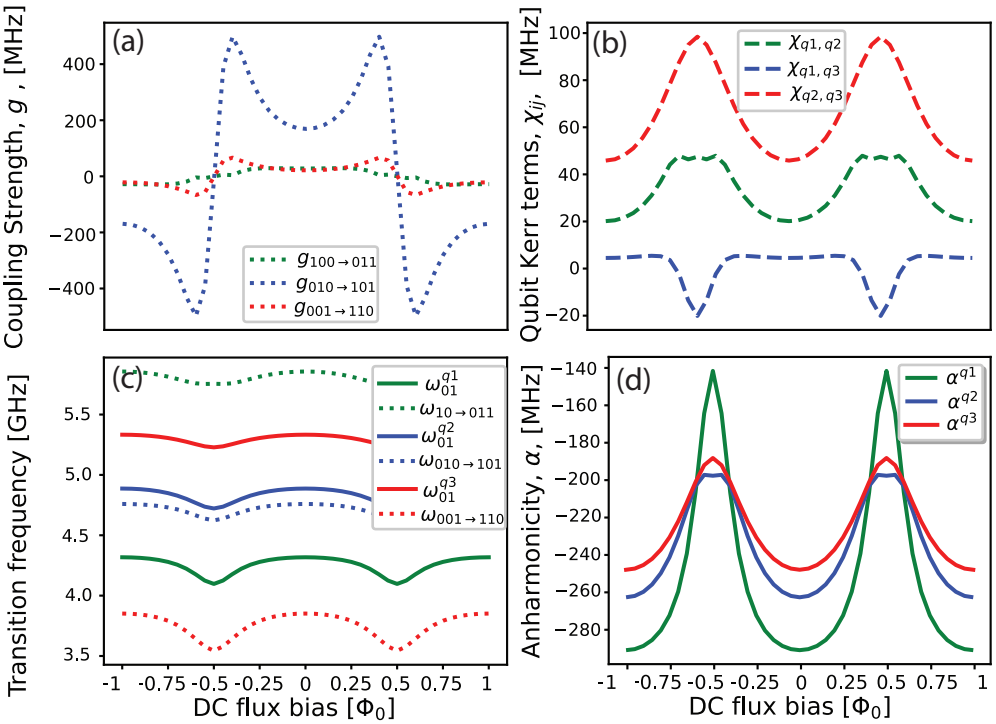

Figure 6.17: The alternative design of three-qubit devices as a function of DC flux bias. (a) shows the pre-factor of the three-body terms without considering the pump signal strength. In (b), the qubit-qubit Kerr, $\chi_{qi,qj}$, as a function of flux bias. (c) Qubit frequencies as functions of flux bias due to the presence of the SQUID (solid). The resonance frequencies of the three-body transitions are also plotted in (dotted). Also, qubit anharmonicities are plotted as the SQUID is biased in (d).

Finally, we evaluated the effect of the parametric drive on the coupling strength and three-body resonance frequencies in Fig. 6.18. The strongest coupling we achieved was for the interaction ($|010\rangle \to |101\rangle$) with a strength of 25 MHz at a parametric amplitude

of $0.1\Phi_0$, as seen in panel (a). The shifts in resonance frequencies were on the scale of a couple of MHz, whereas in the previous design, the shifts were one order of magnitude larger. While this design mitigates the previous issues, one challenge that remains here is to increase the coupling of other interaction permutations to be at a comparable strength. This can be achieved with a simple optimization algorithm to tune the qubit charging and junction energies.

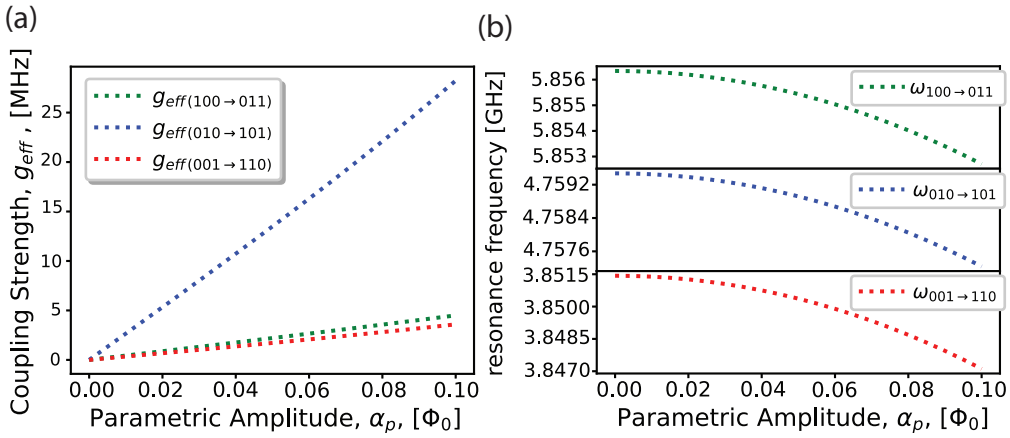

Figure 6.18: Alternative three-qubit design interaction strength and resonance. Calculations to first-order in perturbation theory at zero flux bias are shown in (a) and (b), which describe the strength and three-body resonance, ω_{3q}, of the interaction as a function of pump signal amplitude, respectively.

Chapter 7

Conclusion

We have introduced a platform for programmable analog quantum simulation of topological lattice models. The platform is hardware efficient, creating the lattice in synthetic dimensions within a single parametric cavity terminated at the short circuit end with a SQUID. We have demonstrated the potential of the platform and *in situ* tunable complex couplings that are parametrically created and controlled with pump magnitude and phase. We performed small-scale simulations of paradigmatic topological models of the bosonic Creutz ladder and bosonic Kitaev chain, showing that we can reconstruct the realized Hamiltonians and their topological features.

We have demonstrated that nontrivial non-Hermitian topological systems can be realized using parametric downconversion on our AQS platform. Unlike dissipation-induced non-Hermiticity, this approach allows us to preserve some of the Hamiltonian symmetries, such as time-reversal symmetry. Therefore, this platform can be used to explore the rich topological phases and symmetries of non-Hermitian systems. Furthermore, since the dynamics are the results of a coherent process in a Hermitian Hamiltonian [40], our AQS platform can implement genuine quantum dynamics with effective non-Hermiticity.

Comparing to competing platforms, such as shaking the optical lattice of a cold-atom system [83] or modulating a harmonic optical cavity [84], we can make the general statement that experimental demonstrations of simulations with complex hopping parameters have generally employed some type of global modulation. While this global approach offers efficiency, it also imposes limitations on uniformity and simulation size, as individual couplings cannot be tuned and, *e.g.*, the global control field will vary across the lattice. Further, the global approach will generally limit the type and complexity of phase patterns, *i.e.* simulated field configurations, that can be imprinted on the lattice. Lastly, the accessible

connectivity graphs of these approaches is generally both limited and not programmable. Our local approach, with individual amplitude and phase control on every link, circumvents these problems. The obvious trade-off is the relatively large number of control fields required.

In the last chapter, we proposed and implemented a three-qubit circuit to simulate U(1) LGTs. We built a building block consisting of two matter sites connected by gauge field link where all are encoded as qubits. In the experiment, we observed the system evolution maintains the U(1) symmetry, and the gauge field satisfies Gauss's law. While alternative approaches rely on the breakdown of three-body interaction terms in U(1) LGTs into smaller two-qubit gates or impose additional penalty terms in the Hamiltonian to keep the system state in Hilbert subspace that respects Gauss's law, we here implemented the three-body interaction explicitly saving computational costs and avoiding ad-hoc approaches. That way our three-qubit building block can be easily employed to create large-scale LGTs models, including in higher dimensions.

7.1 Future work

In our experimental work on lattice models using a cavity-based AQS platform, we mainly used a coherent classical state. The next natural step is to study quantum correlations and/or introduce nonclassical states. In fact, in the bosonic kitaev chain, the pairing term corresponds to a two-mode downconversion that generates entangled photons in pairs of modes. This immediately implies that we can study quantum correlations in our 3-site chain as well as other non-Hermitian models that can be realized with squeezing terms. Alternatively, using single-mode downconversion on one mode, we create squeezed state reservoirs, which then can be weakly coupled to a lattice as a source of nonclassical states. More generally, one can couple a qubit to the parametric cavity as a source of programmable quantum states, or for tomography purposes.

Furthermore, while we considered the linear limit of our cavity-based AQS platform in the models we simulated, we can extend it to investigate models with nonlinearities. The cavity modes inherit some of the SQUID nonlinearities which leads to addition terms like self-Kerr and cross-Kerr terms. One can consider these terms to study the nonlinear Kitaev chain. In fact, during the kitaev chain experiment, we noticed that the model exhibits nonlinear dynamics above a specific threshold of coupling strength. For instance, we have observed coupled parametric oscillations in the system, which can be interesting to explore in future work. This would serve as a first example of non-Hermitian non-linear quantum dynamics.

We consider the scalability of our cavity-based AQS platform. We can increase the number of nodes in a single cavity in a straightforward manner by increasing the physical length of the cavity, increasing the density of the cavity modes in frequency [85]. Achieving a frequency spacing of 100 MHz is straightforward. This would allow approximately 10 modes per 1 GHz within our 8 GHz of measurement bandwidth. This mode spacing would still easily allow for $g_{nm} \approx$ 10-20 MHz without worrying about mode crowding. However, we do imagine that eventually there will be a limit to the number of pump tones we can apply to a single cavity. In that sense, we view this device design as a hardware-efficient building block in a larger system consisting of many of these cavities parametrically coupled to each other [86]. Each individual cavity would then be a sublattice stitched together into a larger lattice made of several cavities. Devices made from hundreds of coupled cavities on a single chip have been demonstrated [87].

While we have emphasized, as a demonstration, the simulation of a quasi-1D lattice, the platform is easily extensible to two dimensions (or higher). Essentially, the connection graph of the simulated lattice is arbitrary and the dimensionality of the simulation is set by the number of nearest-neighbor connections of each node. As an example of possible physics to explore, Ref. [88] proposed a pattern of hopping phases that produces an effective (magnetic) gauge field for photons in a 2D photonic lattice like ours.

Now, we consider future work of a three-qubit circuit for U(1) LGTs. There are three parallel lines of works. First, the next step would be to build a simple model with at least 3 matter sites to observe nontrivial phenomena associated with LGTs such as string breaking or confinement. In addition, in LGTs, the gauge fields are bosonic degrees of freedom with infinite Hilbert space; therefore, we will replace the link qubit with a resonator that naturally represents gauge fields. Finally, although the ZZ terms that we observed in our design do not break the U(1) symmetry, it does not show up in theoretical models. Hence, one could find alternative coupling approaches or qubit designs that suppress the residual ZZ couplings.

Letter of Copyright Permission

Use of material from Ref. [27] is covered by American Physical Societys (APS) standing rules on their Physical Review journals of which, for the purpose of use of an article in a thesis where the thesis author is also the author of said article, Yes, the author has the right to use the article or a portion of the article in a thesis or dissertation without requesting permission from APS, provided the bibliographic citation and the APS copyright credit line are given on the appropriate pages.

References

[1] Milad Marvian, Daniel A Lidar, and Itay Hen. On the computational complexity of curing non-stoquastic hamiltonians. *Nature communications*, 10(1):1571, 2019.

[2] Dominik Hangleiter, Ingo Roth, Daniel Nagaj, and Jens Eisert. Easing the monte carlo sign problem. *Science advances*, 6(33):eabb8341, 2020.

[3] Gaopei Pan and Zi Yang Meng. Sign problem in quantum monte carlo simulation. *arXiv preprint arXiv:2204.08777*, 2022.

[4] Mauro Iazzi, Alexey A Soluyanov, and Matthias Troyer. Topological origin of the fermion sign problem. *Physical Review B*, 93(11):115102, 2016.

[5] Matthew B Hastings. How quantum are non-negative wavefunctions? *Journal of Mathematical Physics*, 57(1), 2016.

[6] Christof Gattringer and Christian Lang. *Quantum chromodynamics on the lattice: an introductory presentation*, volume 788. Springer Science & Business Media, 2009.

[7] Esteban A Calzetta and Bei-Lok B Hu. *Nonequilibrium quantum field theory*. Cambridge University Press, 2009.

[8] Adam Smith, Omri Golan, and Zohar Ringel. Intrinsic sign problems in topological quantum field theories. *Physical review research*, 2(3):033515, 2020.

[9] Omri Golan, Adam Smith, and Zohar Ringel. Intrinsic sign problem in fermionic and bosonic chiral topological matter. *Physical Review Research*, 2(4):043032, 2020.

[10] Raka Dasgupta and Indrakshi Raychowdhury. Cold-atom quantum simulator for string and hadron dynamics in non-abelian lattice gauge theory. *Physical Review A*, 105(2):023322, 2022.

[11] Matthias Troyer and Uwe-Jens Wiese. Computational complexity and fundamental limitations to fermionic quantum monte carlo simulations. *Physical Review Letters*, 94(17):170201, 2005.

[12] Michael Tinkham. *Introduction to superconductivity*. Courier Corporation, 2004.

[13] Vinay Ambegaokar and Alexis Baratoff. Tunneling between superconductors. *Physical Review Letters*, 10(11):486, 1963.

[14] Chung Wai Sandbo Chang. *Two-photon and Three-photon Parametric Interactions in Superconducting Microwave Circuits*. PhD thesis, University of Waterloo, 2019.

[15] Steven M Girvin. Circuit qed: superconducting qubits coupled to microwave photons. *Quantum machines: measurement and control of engineered quantum systems*, pages 113–256, 2014.

[16] Jens Koch, M Yu Terri, Jay Gambetta, Andrew A Houck, David I Schuster, Johannes Majer, Alexandre Blais, Michel H Devoret, Steven M Girvin, and Robert J Schoelkopf. Charge-insensitive qubit design derived from the cooper pair box. *Physical Review A*, 76(4):042319, 2007.

[17] David M Pozar. *Microwave engineering*. John wiley & sons, 2011.

[18] Eva Zakka-Bajjani, François Nguyen, Minhyea Lee, Leila R Vale, Raymond W Simmonds, and José Aumentado. Quantum superposition of a single microwave photon in two different'colour'states. *Nature Physics*, 7(8):599–603, 2011.

[19] Martin Sandberg, CM Wilson, Fredrik Persson, Thilo Bauch, Göran Johansson, Vitaly Shumeiko, Tim Duty, and Per Delsing. Tuning the field in a microwave resonator faster than the photon lifetime. *Applied Physics Letters*, 92(20):203501, 2008.

[20] Roy J Glauber. Coherent and incoherent states of the radiation field. *Physical Review*, 131(6):2766, 1963.

[21] Emmanuel Flurin, Nicolas Roch, François Mallet, Michel H Devoret, and Benjamin Huard. Generating entangled microwave radiation over two transmission lines. *Physical Review Letters*, 109(18):183901, 2012.

[22] CW Sandbo Chang, M Simoen, José Aumentado, Carlos Sabín, P Forn-Díaz, AM Vadiraj, Fernando Quijandría, G Johansson, I Fuentes, and CM Wilson. Generating multimode entangled microwaves with a superconducting parametric cavity. *Physical Review Applied*, 10(4):044019, 2018.

[23] Michael Creutz. End States, Ladder Compounds, and Domain-Wall Fermions. *Physical Review Letters*, 83(13):2636, 1999.

[24] Hadiseh Alaeian, Chung Wai Sandbo Chang, Mehran Vahdani Moghaddam, Christopher M Wilson, Enrique Solano, and Enrique Rico. Creating lattice gauge potentials in circuit QED: The bosonic Creutz ladder. *Physical Review A*, 99(5):053834, 2019.

[25] Juan Zurita, Charles E Creffield, and Gloria Platero. Topology and Interactions in the Photonic Creutz and Creutz-Hubbard Ladders. *Advanced Quantum Technologies*, 3(2):1900105, 2020.

[26] Michael Creutz. Chiral Symmetry and Lattice Fermions. *arXiv preprint arXiv:1309.6288*, 2013.

[27] Jimmy SC Hung, JH Busnaina, CW Sandbo Chang, AM Vadiraj, I Nsanzineza, E Solano, H Alaeian, E Rico, and CM Wilson. Quantum simulation of the bosonic creutz ladder with a parametric cavity. *Physical Review Letters*, 127(10):100503, 2021.

[28] Goran Lindblad. On the generators of quantum dynamical semigroups. *Communications in Mathematical Physics*, 48:119–130, 1976.

[29] Crispin Gardiner and Peter Zoller. *Quantum Noise: A Handbook of Markovian and Non-Markovian Quantum Stochastic Methods with Applications to Quantum Optics*. Springer Science & Business Media, 2004.

[30] F Lecocq, L Ranzani, GA Peterson, K Cicak, RW Simmonds, JD Teufel, and J Aumentado. Nonreciprocal Microwave Signal Processing with a Field-Programmable Josephson Amplifier. *Physical Review Applied*, 7(2):024028, 2017.

[31] Corey Rae Harrington McRae, Haozhi Wang, Jiansong Gao, Michael R Vissers, Teresa Brecht, Andrew Dunsworth, David P Pappas, and Josh Mutus. Materials loss measurements using superconducting microwave resonators, 2020.

[32] M Stoutimore Khalil, MJA Stoutimore, FC Wellstood, and KD Osborn. An analysis method for asymmetric resonator transmission applied to superconducting devices. *Journal of Applied Physics*, 111(5), 2012.

[33] Alexander McDonald, T Pereg-Barnea, and AA Clerk. Phase-dependent chiral transport and effective non-hermitian dynamics in a bosonic kitaev-majorana chain. *Physical Review X*, 8(4):041031, 2018.

[34] Tomoki Ozawa, Hannah M Price, Alberto Amo, Nathan Goldman, Mohammad Hafezi, Ling Lu, Mikael C Rechtsman, David Schuster, Jonathan Simon, Oded Zilberberg, et al. Topological photonics. *Reviews of Modern Physics*, 91(1):015006, 2019.

[35] Zongping Gong, Yuto Ashida, Kohei Kawabata, Kazuaki Takasan, Sho Higashikawa, and Masahito Ueda. Topological phases of non-hermitian systems. *Physical Review X*, 8(3):031079, 2018.

[36] J. H. Busnaina, Z. Shi, A. McDonald, D. Dubyna, I. Nsanzineza, Jimmy S. C. Hung, C. W. Sandbo Chang, A. A. Clerk, and C. M. Wilson. Quantum simulation of the bosonic kitaev chain, 2023.

[37] A Yu Kitaev. Unpaired majorana fermions in quantum wires. *Physics-uspekhi*, 44(10S):131, 2001.

[38] Vincent P Flynn, Emilio Cobanera, and Lorenza Viola. Deconstructing effective non-hermitian dynamics in quadratic bosonic hamiltonians. *New Journal of Physics*, 22(8):083004, 2020.

[39] Naomichi Hatano and David R Nelson. Localization transitions in non-hermitian quantum mechanics. *Physical Review Letters*, 77(3):570, 1996.

[40] Yu-Xin Wang and AA Clerk. Non-hermitian dynamics without dissipation in quantum systems. *Physical Review A*, 99(6):063834, 2019.

[41] Shunyu Yao and Zhong Wang. Edge states and topological invariants of non-hermitian systems. *Physical Review Letters*, 121(8):086803, 2018.

[42] Joonsuk Huh, Gian Giacomo Guerreschi, Borja Peropadre, Jarrod R McClean, and Alán Aspuru-Guzik. Boson sampling for molecular vibronic spectra. *Nature Photonics*, 9(9):615–620, 2015.

[43] Ta-Pei Cheng and Ling-Fong Li. *Gauge theory of elementary particle physics*. Oxford university press, 1994.

[44] Kenneth G Wilson. Confinement of quarks. *Physical review D*, 10(8):2445, 1974.

[45] John B Kogut. An introduction to lattice gauge theory and spin systems. *Reviews of Modern Physics*, 51(4):659, 1979.

[46] U-J Wiese. Ultracold quantum gases and lattice systems: quantum simulation of lattice gauge theories. *Annalen der Physik*, 525(10-11):777–796, 2013.

[47] Eduardo Fradkin. *Field theories of condensed matter physics*. Cambridge University Press, 2013.

[48] Leon Balents. Spin liquids in frustrated magnets. *Nature*, 464(7286):199–208, 2010.

[49] Lucile Savary and Leon Balents. Quantum spin liquids: a review. *Reports on Progress in Physics*, 80(1):016502, 2016.

[50] Xiao-Gang Wen. *Quantum field theory of many-body systems: from the origin of sound to an origin of light and electrons*. OUP Oxford, 2004.

[51] Christian Prosko, Shu-Ping Lee, and Joseph Maciejko. Simple z 2 lattice gauge theories at finite fermion density. *Physical Review B*, 96(20):205104, 2017.

[52] Federica Maria Surace, Pierre Fromholz, Nelson Darkwah Oppong, Marcello Dalmonte, and Monika Aidelsburger. *ab initio* derivation of lattice gauge theory dynamics for cold gases in optical lattices. *arXiv preprint arXiv:2301.03474*, 2023.

[53] Zoltan Fodor and Christian Hoelbling. Light hadron masses from lattice qcd. *Reviews of Modern Physics*, 84(2):449, 2012.

[54] USQCD collaboration, William Detmold, Robert G Edwards, Jozef J Dudek, Michael Engelhardt, Huey-Wen Lin, Stefan Meinel, Kostas Orginos, and Phiala Shanahan. Hadrons and nuclei. *The European Physical Journal A*, 55:1–27, 2019.

[55] CE DeTar and UM Heller. Qcd thermodynamics from the lattice. *The European Physical Journal A*, 41:405–437, 2009.

[56] Kenji Fukushima and Tetsuo Hatsuda. The phase diagram of dense qcd. *Reports on Progress in Physics*, 74(1):014001, 2010.

[57] Owe Philipsen. Constraining the qcd phase diagram at finite temperature and density. *arXiv preprint arXiv:1912.04827*, 2019.

[58] Sz Borsanyi, Z Fodor, JN Guenther, C Hoelbling, SD Katz, L Lellouch, T Lippert, K Miura, L Parato, KK Szabo, et al. Leading hadronic contribution to the muon magnetic moment from lattice qcd. *Nature*, 593(7857):51–55, 2021.

[59] Michael Creutz, Laurence Jacobs, and Claudio Rebbi. Monte carlo computations in lattice gauge theories. *Physics Reports*, 95(4):201–282, 1983.

[60] Bálint Joó, Chulwoo Jung, Norman H Christ, William Detmold, Robert G Edwards, Martin Savage, and Phiala Shanahan. Status and future perspectives for lattice gauge theory calculations to the exascale and beyond. *The European Physical Journal A*, 55:1–26, 2019.

[61] Philippe De Forcrand. Simulating qcd at finite density. *arXiv preprint arXiv:1005.0539*, 2010.

[62] Mari Carmen Banuls, Rainer Blatt, Jacopo Catani, Alessio Celi, Juan Ignacio Cirac, Marcello Dalmonte, Leonardo Fallani, Karl Jansen, Maciej Lewenstein, Simone Montangero, et al. Simulating lattice gauge theories within quantum technologies. *The European physical journal D*, 74:1–42, 2020.

[63] Zohreh Davoudi, Mohammad Hafezi, Christopher Monroe, Guido Pagano, Alireza Seif, and Andrew Shaw. Towards analog quantum simulations of lattice gauge theories with trapped ions. *Physical Review Research*, 2(2):023015, 2020.

[64] Natalie Klco, Martin J Savage, and Jesse R Stryker. Su (2) non-abelian gauge field theory in one dimension on digital quantum computers. *Physical Review D*, 101(7):074512, 2020.

[65] Zohreh Davoudi, Norbert M Linke, and Guido Pagano. Toward simulating quantum field theories with controlled phonon-ion dynamics: A hybrid analog-digital approach. *Physical Review Research*, 3(4):043072, 2021.

[66] Julius Mildenberger, Wojciech Mruczkiewicz, Jad C Halimeh, Zhang Jiang, and Philipp Hauke. Probing confinement in a $\mathbb{Z}_2$ lattice gauge theory on a quantum computer. *arXiv preprint arXiv:2203.08905*, 2022.

[67] Esteban A Martinez, Christine A Muschik, Philipp Schindler, Daniel Nigg, Alexander Erhard, Markus Heyl, Philipp Hauke, Marcello Dalmonte, Thomas Monz, Peter Zoller, et al. Real-time dynamics of lattice gauge theories with a few-qubit quantum computer. *Nature*, 534(7608):516–519, 2016.

[68] Christian Kokail, Christine Maier, Rick van Bijnen, Tiff Brydges, Manoj K Joshi, Petar Jurcevic, Christine A Muschik, Pietro Silvi, Rainer Blatt, Christian F Roos, et al. Self-verifying variational quantum simulation of lattice models. *Nature*, 569(7756):355–360, 2019.

[69] Nhung H Nguyen, Minh C Tran, Yingyue Zhu, Alaina M Green, C Huerta Alderete, Zohreh Davoudi, and Norbert M Linke. Digital quantum simulation of the schwinger model and symmetry protection with trapped ions. *PRX Quantum*, 3(2):020324, 2022.

[70] Christian W Bauer, Zohreh Davoudi, Natalie Klco, and Martin J Savage. Quantum simulation of fundamental particles and forces. *Nature Reviews Physics*, pages 1–13, 2023.

[71] Anthony N Ciavarella, Stephan Caspar, Hersh Singh, and Martin J Savage. Preparation for quantum simulation of the $(1 + 1)$-dimensional o(3) nonlinear σ model using cold atoms. *Physical Review A*, 107(4):042404, 2023.

[72] Samuel A Wilkinson and Michael J Hartmann. Superconducting quantum many-body circuits for quantum simulation and computing. *Applied Physics Letters*, 116(23):230501, 2020.

[73] Rasmus Berg Jensen, Simon Panyella Pedersen, and Nikolaj Thomas Zinner. Dynamical quantum phase transitions in a noisy lattice gauge theory. *Physical Review B*, 105(22):224309, 2022.

[74] Lukas Homeier, Annabelle Bohrdt, Simon Linsel, Eugene Demler, Jad C Halimeh, and Fabian Grusdt. Realistic scheme for quantum simulation of z 2 lattice gauge theories with dynamical matter in (2+ 1) d. *Communications Physics*, 6(1):127, 2023.

[75] Alessio Celi, Benoît Vermersch, Oscar Viyuela, Hannes Pichler, Mikhail D Lukin, and Peter Zoller. Emerging two-dimensional gauge theories in rydberg configurable arrays. *Physical Review X*, 10(2):021057, 2020.

[76] Michael Hermele, Matthew PA Fisher, and Leon Balents. Pyrochlore photons: The $u(1)$ spin liquid in a $s = \frac{1}{2}$ three-dimensional frustrated magnet. *Physical Review B*, 69(6):064404, 2004.

[77] Adam Smith, Johannes Knolle, Roderich Moessner, and Dmitry L Kovrizhin. Dynamical localization in z 2 lattice gauge theories. *Physical Review B*, 97(24):245137, 2018.

[78] Debasish Banerjee, M Dalmonte, M Müller, E Rico, P Stebler, U-J Wiese, and P Zoller. Atomic quantum simulation of dynamical gauge fields coupled to fermionic matter: From string breaking to evolution after a quench. *Physical Review Letters*, 109(17):175302, 2012.

[79] Dayou Yang, Gouri Shankar Giri, Michael Johanning, Christof Wunderlich, Peter Zoller, and Philipp Hauke. Analog quantum simulation of (1+ 1)-dimensional lattice qed with trapped ions. *Physical Review A*, 94(5):052321, 2016.

[80] Jonas Bylander, Simon Gustavsson, Fei Yan, Fumiki Yoshihara, Khalil Harrabi, George Fitch, David G Cory, Yasunobu Nakamura, Jaw-Shen Tsai, and William D Oliver. Noise spectroscopy through dynamical decoupling with a superconducting flux qubit. *Nature Physics*, 7(7):565–570, 2011.

[81] Stefan Filipp, Patrick Maurer, Peter J Leek, M Baur, R Bianchetti, JM Fink, M Göppl, L Steffen, Jay M Gambetta, Alexandre Blais, et al. Two-qubit state tomography using a joint dispersive readout. *Physical Review Letters*, 102(20):200402, 2009.

[82] R Bianchetti, Stefan Filipp, M Baur, JM Fink, M Göppl, Peter J Leek, L Steffen, Alexandre Blais, and Andreas Wallraff. Dynamics of dispersive single-qubit readout in circuit quantum electrodynamics. *Physical Review A*, 80(4):043840, 2009.

[83] Jin Hyoun Kang, Jeong Ho Han, and YI Shin. Creutz ladder in a resonantly shaken 1D optical lattice. *New Journal of Physics*, 22(1):013023, 2020.

[84] Avik Dutt, Qian Lin, Luqi Yuan, Momchil Minkov, Meng Xiao, and Shanhui Fan. A single photonic cavity with two independent physical synthetic dimensions. *Science*, 367(6473):59–64, 2020.

[85] Nathan RA Lee, Marek Pechal, E Alex Wollack, Patricio Arrangoiz-Arriola, Zhaoyou Wang, and Amir H Safavi-Naeni. Propagation of microwave photons along a synthetic dimension. *Physical Review A*, 101(5):053807, 2020.

[86] Borja Peropadre, David Zueco, Friedrich Wulschner, Frank Deppe, Achim Marx, Rudolf Gross, and Juan José García-Ripoll. Tunable coupling engineering between superconducting resonators: From sidebands to effective gauge fields. *Physical Review B*, 87(13):134504, 2013.

[87] Andrew A Houck, Hakan E Türeci, and Jens Koch. On-chip quantum simulation with superconducting circuits. *Nature Physics*, 8(4):292–299, 2012.

[88] Kejie Fang, Zongfu Yu, and Shanhui Fan. Realizing effective magnetic field for photons by controlling the phase of dynamic modulation. *Nature photonics*, 6(11):782–787, 2012.

[89] Jad C Halimeh and Philipp Hauke. Reliability of lattice gauge theories. *Physical Review Letters*, 125(3):030503, 2020.

[90] Hannes Bernien, Sylvain Schwartz, Alexander Keesling, Harry Levine, Ahmed Omran, Hannes Pichler, Soonwon Choi, Alexander S Zibrov, Manuel Endres, Markus Greiner, et al. Probing many-body dynamics on a 51-atom quantum simulator. *Nature*, 551(7682):579–584, 2017.

[91] Jad C Halimeh, Lukas Homeier, Hongzheng Zhao, Annabelle Bohrdt, Fabian Grusdt, Philipp Hauke, and Johannes Knolle. Enhancing disorder-free localization through dynamically emergent local symmetries. *PRX Quantum*, 3(2):020345, 2022.

[92] Adith Sai Aramthottil, Utso Bhattacharya, Daniel González-Cuadra, Maciej Lewenstein, Luca Barbiero, and Jakub Zakrzewski. Scar states in deconfined z 2 lattice gauge theories. *Physical Review B*, 106(4):L041101, 2022.

[93] Jad C Halimeh and Philipp Hauke. Origin of staircase prethermalization in lattice gauge theories. *arXiv preprint arXiv:2004.07254*, 2020.

[94] Martin Suchara, John Kubiatowicz, Arvin Faruque, Frederic T Chong, Ching-Yi Lai, and Gerardo Paz. Qure: The quantum resource estimator toolbox. In *2013 IEEE 31st International Conference on Computer Design (ICCD)*, pages 419–426. IEEE, 2013.

[95] Reinis Irmejs, Mari Carmen Banuls, and Juan Ignacio Cirac. Quantum simulation of z2 lattice gauge theory with minimal requirements. *arXiv preprint arXiv:2206.08909*, 2022.

[96] Maarten Van Damme, Haifeng Lang, Philipp Hauke, and Jad C Halimeh. Reliability of lattice gauge theories in the thermodynamic limit. *Physical Review B*, 107(3):035153, 2023.

[97] Philipp Hauke, David Marcos, Marcello Dalmonte, and Peter Zoller. Quantum simulation of a lattice schwinger model in a chain of trapped ions. *Physical Review X*, 3(4):041018, 2013.

[98] Valentin Kasper, Florian Hebenstreit, Fred Jendrzejewski, Markus K Oberthaler, and Jürgen Berges. Implementing quantum electrodynamics with ultracold atomic systems. *New journal of physics*, 19(2):023030, 2017.

[99] Akihiro Tanaka and Shintaro Takayoshi. A short guide to topological terms in the effective theories of condensed matter. *Science and Technology of Advanced Materials*, 16(1):014404, 2015.